

INVESTIGATING THE MECHANISM OF BACTERIAL CELL DIVISION WITH
SUPERRESOLUTION MICROSCOPY

by

Carla Coltharp

A dissertation submitted to Johns Hopkins University in conformity with the
requirements for the degree of Doctor of Philosophy

Baltimore, Maryland

April, 2015

Abstract

The molecular mechanisms that drive bacterial cytokinesis are attractive antibiotic targets that remain poorly understood. The machinery that performs cytokinesis in bacteria has been termed the 'divisome' (see Chapter 1 for description). The most widely-conserved divisome protein, FtsZ, is an essential tubulin homolog that polymerizes into protofilaments in a nucleotide-dependent manner. These protofilaments assemble at midcell to form the 'Z-ring', which has been the prevailing candidate for constrictive force generation during cell division. However, it has been difficult to experimentally test proposed Z-ring force generation models *in vivo* due to the small size of bacteria (< 1 μm diameter for *E. coli*) compared to the diffraction-limited resolution of light ($\sim 0.3 \mu\text{m}$).

In this work, quantitative superresolution and time-lapse microscopy were applied to examine whether Z-ring structure and function indeed play limiting roles in driving *E. coli* cell constriction (Chapter 2). Surprisingly, these studies revealed that the rate of septum closure during constriction is robust to substantial changes in many Z-ring properties, including the GTPase activity of FtsZ, molecular density of the Z-ring, the timing of Z-ring disassembly, and the absence of Z-ring assembly regulators. Further investigation revealed that septum closure rate is instead highly coupled to the rate of cell wall growth and elongation, and can be modulated by coordination with chromosome segregation. Taken together, these results challenge the Z-ring centric view of constriction force generation, and suggest that cell wall synthesis and chromosome segregation likely drive the rate and progress of cell constriction in bacteria.

These investigations were made possible by advancements in quantitative superresolution microscopy techniques (see Chapter 3 for overview). One major obstacle encountered during

the course of this work, and shared by those utilizing localization-based superresolution microscopy techniques, was the overestimation of molecule numbers caused by fluorophore photoblinking. Thus, Chapter 4 describes a systematic characterization of the effects of photoblinking on the accurate construction and analysis of superresolution images. These characterizations enabled the development of a simple method to identify the optimal clustering thresholds and an empirical criterion to evaluate whether an imaging condition is appropriate for accurate superresolution image reconstruction. Both the threshold selection method and imaging condition criterion are easy to implement within existing PALM clustering algorithms and experimental conditions.

Primary Reader: Jie Xiao

Secondary Reader: Christian Kaiser

Acknowledgements

As will become clear in Chapter 2, this project took a few unexpected turns along the way. Through that process, my advisor, Jie Xiao, was a unwavering source of enthusiasm, motivation, and confidence as we unraveled the puzzles that came our way. I also received timely advice from all the members of the Xiao lab, our collaborators in the Goley lab, and my thesis advisory committee (Erin Goley, Jin Zhang, and Christian Kaiser) that were invaluable to this project. I'm especially indebted to Jackson Buss for allowing me to write 'as described previously' so many times in my papers and Xinxing Yang for thoughtful, and always joyful, criticism. These lively and constructive discussions about science and life provided a fantastic work environment where I was inspired by the fortitude of Zach Hensel, meticulousness of Tao Huang, generosity of Rene Kessler, persistence of Xiaoli Weng, earnestness of Kelsey Bettridge, tirelessness of Gina Wang, daydreaming of Chris Bohrer, and enthusiasm of Ryan McQuillen. The work itself would not have been possible without our generous collaborators at the HHMI Janelia Farm Campus, Harald Hess and Gleb Shtengel, funding from the NIH, and the tireless work of our program's support staff. I thank all of these wonderful colleagues for their support during this project.

I especially want to thank my family and friends for their continued love and support. Everything I've accomplished and will accomplish stems from the encouragement and example of my mom, Kyong Coltharp, who is a model of self-reliance and composure. Matt Preimesberger has been my support on a daily basis, inspiring me with his undying fascination with science, sharing my love of cooking and gardening, and always asking me 'why?' and 'how?'. Finally, Emily Adney has been my wonderful friend and confidant, who always knows how to put everything in perspective. Many thanks to all these loved ones.

Contents

Abstract.....	ii
Acknowledgements.....	iv
Contents.....	v
List of Figures	xi
Part I: The Processes that Drive Cytokinesis in Bacteria	1
Chapter 1 : Introduction to Bacterial Cytokinesis	2
The Bacterial Divisome	3
The cytoplasmic scaffold.....	4
The periplasmic cell wall modifiers.....	6
The chromosomal linkage.....	8
Proposed Force Generation Mechanisms.....	8
Chapter 2 : Contributions of the Z-ring, cell wall synthesis, and chromosome segregation in driving <i>E. coli</i> cytokinesis	13
Introduction	14
Results.....	14
3D structure of the <i>E. coli</i> Z-ring	14
Z-ring width and thickness remain constant during contraction.....	23
The Z-ring contracts in two apparent phases	24
The Z-ring condenses as it contracts.....	27

Measuring septum closure rate.....	30
90% reduction in FtsZ GTPase activity alters Z-ring density and dynamics, but not septum closure rate	32
<i>minC</i> and <i>matP</i> deletions alter Z-ring density and dynamics similarly, but septum closure rate oppositely	35
Septum closure rate is coupled to cell elongation rate	37
Absence of MatP modulates the coupling between cell wall elongation and septum closure rate.....	43
Discussion	44
Z-ring Organization	44
Constriction Initiation	46
Z-ring function during constriction	47
The role of FtsZ's GTPase activity.....	48
Factors driving cell constriction	49
Summary	51
Materials and Methods.....	52
Bacterial strains and plasmid construction.....	52
Growth conditions and sample preparation.....	54
Fluorescence imaging	57
FtsZ cluster simulation	58

Additional image processing, data analysis, and simulation	60
Statistics	63
Part II: Quantitative Superresolution Fluorescence Microscopy	64
Chapter 3 : Overview of Superresolution Fluorescence Microscopy.....	65
Introduction	66
Single Molecule Localization Methods	67
Structured Illumination Microscopy (SIM).....	69
Stimulated Emission Depletion Microscopy (STED).....	69
Practical Considerations for Microbiology.....	70
Time Resolution	70
Imaging Duration	71
Probe Selection	72
Functionality of Labeled Protein.....	74
Expression Level.....	74
Fixation.....	75
Sample Immobilization	75
Hardware and Software Complexity	76
Quantitative Analyses	77
Image-based Analyses.....	77
Counting Molecule Numbers	80

Identifying Spatial Distribution Patterns.....	82
Colocalization.....	86
Outlook	89
Chapter 4 : Accurate Construction of Photo-activated Localization Microscopy (PALM) Images	
for Quantitative Measurements	91
Introduction	92
Results.....	97
Dimension measurements are not affected by fluorophore blinking, but can be affected by applying a clustering algorithm.....	97
Effects of fluorophore blinking and clustering thresholds on density measurements.....	100
Multiple threshold pairs can result in accurate measurements of both dimension and density measurements	104
The Jaccard Index identifies images that are accurate on both the ensemble and single- molecule level	105
Structural geometry does not affect the positions of the optimum threshold pair and Jaccard index peak	107
Low measurement error is not sufficient to guarantee high Jaccard index	108
Fluorophore blinking kinetics and activation rate determine achievable accuracy in superresolution image reconstruction	109
Identifying the optimal threshold pair from an experimental dataset.....	111
Application of the optimal threshold pair to experimental data.....	115

Discussion	117
Selection of localization-based superresolution imaging method	117
Achievable clustering accuracy is dependent on imaging acquisition condition	119
Physical meaning of optimal threshold values	119
Fluorophore characterization	122
Comparison with other superresolution processing algorithms	123
Methods.....	124
Simulation of FtsZ structures	124
Simulation of circular clusters.....	125
Simulation of fluorophore blinking kinetics.....	126
Superresolution image reconstruction with localization-based PSFs.....	128
Superresolution molecule density measurement	129
Calculation of maximal activation rate	129
Clustering algorithm.....	130
Jaccard index of cluster accuracy.....	131
Preparation and purification of mEos2.....	131
<i>In vitro</i> sample preparation	132
<i>E. coli</i> sample preparation and fixation	132
PALM Imaging conditions	133
Molecule detection in experimental data	133

Appendix 1: Calculation of Spatial Resolution	134
References	137
Curriculum Vitae	152

List of Figures

Figure 1.1 Schematic representation of the divisome.....	4
Figure 1.2 Interactions between divisome constituents.	5
Figure 2.1 Two-color immuno-superresolution imaging of FtsZ and FtsZ-GFP.	16
Figure 2.2 Measurement of spatial resolution.	18
Figure 2.3 3D images of the <i>E. coli</i> Z-ring.....	19
Figure 2.4 Z-ring dimensions.....	20
Figure 2.5 Cluster simulations that best replicate Z-rings observed by iPALM.	22
Figure 2.6 3D images and dimensions of ZapA-rings.....	24
Figure 2.7 Time-lapse analysis of Z-ring dynamics during the cell cycle.....	25
Figure 2.8 Analysis of Z-ring density and time-dependent septum closure rate for BW25113 cells.	28
Figure 2.9 Analysis of Z-ring dimension, density, and time-dependent septum closure rate for MC4100 and MCZ84 cells.	34
Figure 2.10 Analysis of Z-ring dimension, density, and time-dependent septum closure rate for $\Delta minC$ and $\Delta matP$ cells.	36
Figure 2.11 Time-lapse analysis of FtsZ-GFP in other wt and mutant strains.....	38
Figure 2.12 Analysis of Z-ring dimension and density for all wt strains and conditions.....	41
Figure 2.13 Comparison of septum closure and cell elongation rates.	42
Figure 2.14 Immunoblot analysis of FtsZ, FtsZ-mEos2, and FtsZ-GFP expression levels.	56
Figure 2.15 Dimension measurements from superresolution data.....	61
Figure 3.1 Key concepts and acquisition schematics for each superresolution technique.....	68
Figure 3.2 Super-resolution image generation and dimension measurement.....	78

Figure 3.3 Analysis of molecule clustering.....	83
Figure 3.4 Colocalization analysis.	87
Figure 4.1 Fluorophore blinking affects superresolution image quality.....	93
Figure 4.2 Effects of threshold selection on Z-ring width measurement.	98
Figure 4.3 Effects of threshold selection on mean and relative molecule density.....	102
Figure 4.4 Effects of threshold selection on molecule density distribution in the Z-ring.....	104
Figure 4.5 Accuracy of images generated with different threshold pairs.	105
Figure 4.6 Quantitative measurements of a simulated cluster dataset.	107
Figure 4.7 Relationship between Jaccard index, measurement error, and activation rate across different simulated datasets.....	109
Figure 4.8 Characterization of Δt_{repeat} for mEos2.	110
Figure 4.9 Examples of intersection identification in the $ (N - N_{ref}) / N_{ref} $ plot.....	112
Figure 4.10 <i>In vitro</i> characterization of mEos2.	114
Figure 4.11 Characterization of mEos2 in fixed E. coli cells.....	114
Figure 4.12. Determination and application of optimal threshold pair to an experimental image.	116
Figure 4.13 Optimal t_{Thresh} values are related to the mean off time.	120
Figure 4.14 Optimal d_{Thresh} values are related to the spatial resolution.	121
Figure 4.15 Validation of kinetic and spatial simulation parameters.	121
Figure 4.16 Representative simulations of superresolution images.	125
Figure 4.17 Schematic of spot clustering algorithm.	130

Part I:

The Processes that Drive Cytokinesis in Bacteria

Chapter 1 :

Introduction to Bacterial Cytokinesis

The Bacterial Divisome

During cell division, a mechanical force is required to constrict the cell envelope against the turgor pressure of the cytoplasm. In bacteria, this force is supplied by the highly conserved 'divisome' machinery, which assembles at midcell prior to the onset of cell division (Adams and Errington 2009). Although many molecular constituents of the divisome have been identified, the mechanism by which it generates a constrictive force remains unclear.

Divisome constituents can be divided into three groups according to their locations and functions during cell division. The first group forms a dynamic, cytoplasmic scaffold to recruit all other divisome constituents (Figure 1.1, blue). The second group encompasses a large ensemble of transmembrane and periplasmic proteins that are involved in the synthesis and remodeling of the septal cell wall (Figure 1.1, orange). The third group of divisome proteins coordinates cell constriction with chromosome segregation (Figure 1.1, magenta). The members of each of these groups in *E. coli* are described below.

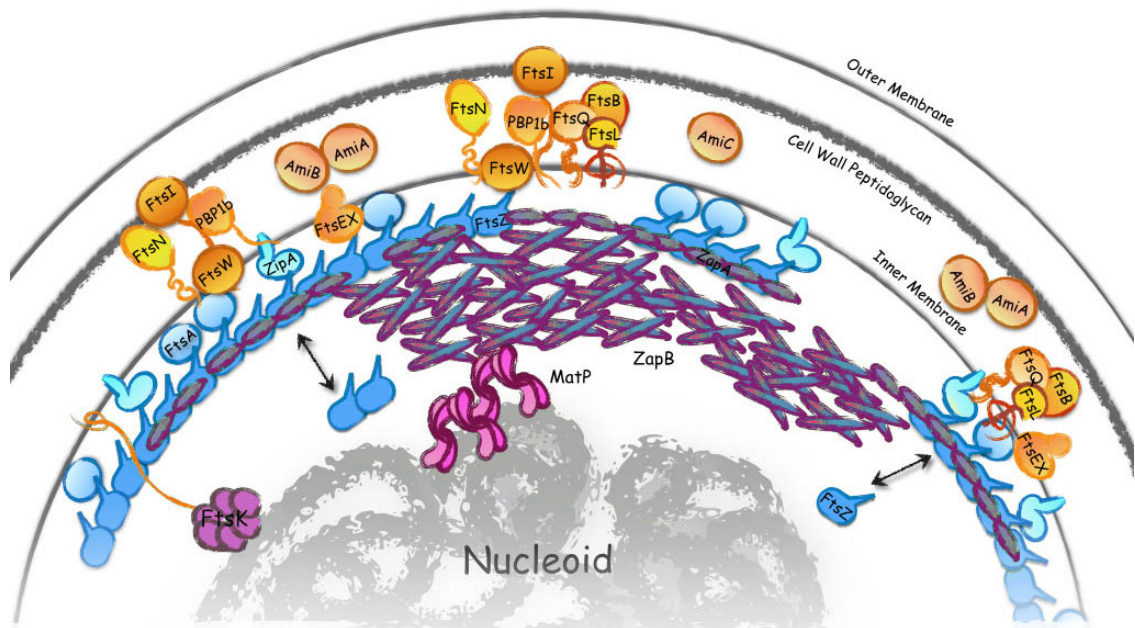


Figure 1.1 Schematic representation of the divisome.

Divisome constituents can be divided into three groups: the membrane-tethered Z-ring (blue shades), the periplasmic peptidoglycan modifiers (orange shades), and the factors that link the Z-ring to the chromosome (magenta shades).

The cytoplasmic scaffold

The first group of divisome proteins to arrive at midcell (Figure 1.1, blue) comprises the highly-conserved tubulin homolog, FtsZ, and its membrane tethers (FtsA and ZipA in *E. coli* (Pichoff and Lutkenhaus 2002))_ENREF_1. FtsZ is the most widely-conserved divisome protein found in almost all prokaryotes in addition to some archaea, chloroplasts, and mitochondria (Erickson 1997). As a tubulin homolog, FtsZ can hydrolyze GTP and polymerize in a nucleotide-dependent manner (de Boer, Crossley et al. 1992; RayChaudhuri and Park 1992; Chen, Bjornson et al. 2005; Erickson, Anderson et al. 2010). These protofilaments can adopt different curvatures depending on the bound nucleotide (Erickson and Stoffler 1996; Lu, Reedy et al. 2000; Mingorance, Tadros

et al. 2005) as the monomer-monomer interface is more bent in the presence of GDP than in the presence of GTP (Chen and Erickson 2011; Li, Hsin et al. 2013). Lateral affinity between FtsZ protofilaments (Lu, Stricker et al. 2001; Shin, Vollmer et al. 2013) allows them to further assemble into a variety of bundles, sheets, and helices under different *in vitro* conditions (Popp, Iwasa et al. 2010).

FtsA and ZipA bind to the same region of FtsZ, its C-terminal tail, to recruit FtsZ subunits to the membrane (Haney 2001; Pichoff and Lutkenhaus 2005). This membrane tethering promotes polymerization of FtsZ molecules into a ring-like structure, or 'Z-ring', at the cytoplasmic face of the inner membrane. This Z-ring is very dynamic, with all three components turning over with half times between 10 - 30 s (Mosyak, Zhang et al. 2000; Stricker, Maddox et al. 2002; Anderson, Gueiros-Filho et al. 2004; Geissler, Shiomi et al. 2007).

In addition to this tethering role, FtsA and ZipA are also required for recruitment of the 'downstream' membrane-associated and periplasmic divisome constituents (Egan and Vollmer 2013). This recruitment is achieved through an extensive protein interaction network (Figure 1.2) that spans the cell envelope (Goehring and Beckwith 2005; Egan and Vollmer 2013).

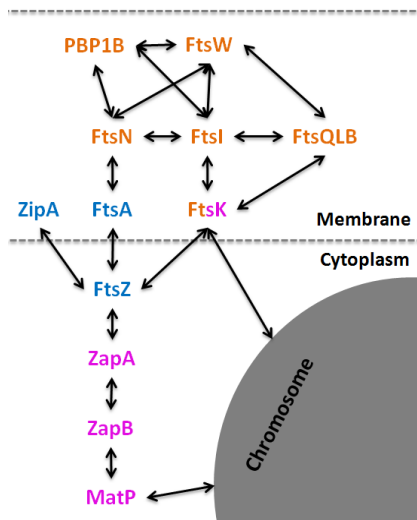


Figure 1.2 Interactions between divisome constituents. Protein names are colored according to the scheme in Figure 1.1: FtsZ and its membrane tethers (blue shades), periplasmic peptidoglycan modifiers (orange shades), and factors that link the Z-ring to the chromosome (magenta shades). Only interactions verified by non two-hybrid assays are shown. Adapted from (Egan and Vollmer 2013).

Although both FtsA and ZipA are essential and required to recruit the downstream divisome proteins in *E. coli*, ZipA is only conserved in γ -proteobacteria (Hale and de Boer 1997) while FtsA is more widely conserved. Furthermore, the mutation *ftsA** has been shown to bypass the essentiality of ZipA in *E. coli* (Geissler, Elraheb et al. 2003). This finding suggests that ZipA may serve to regulate the polymerization state, and thus interaction capability, of FtsA and/or FtsZ, rather than to directly recruit the downstream proteins (Pichoff, Shen et al. 2012).

The periplasmic cell wall modifiers

Subsequent to Z-ring assembly at midcell, the downstream divisome proteins (Figure 1.1 and Figure 1.2, orange) arrive at midcell after a delay that spans $\sim 20\%$ of the cell cycle (Aarsman, Piette et al. 2005). The cause of this delay remains unclear as the current model for the recruitment of these proteins relies on protein-protein interactions (Figure 1.2), which should be established very quickly in a small bacterial cell (Aarsman, Piette et al. 2005). This downstream class of divisome proteins include the enzymes FtsI (aka PBP3) and PBP1b, which perform the majority of septal peptidoglycan (PG) synthesis during cell constriction (Sauvage, Kerff et al. 2008). FtsI is a transpeptidase that generates peptide cross-links between glycan chains in the cell wall (Begg, Takasuga et al. 1990; Nguyen-Disteche, Fraipont et al. 1998; Sauvage, Derouaux et al. 2014). PBP1b interacts with FtsI at midcell (Figure 1.2) and has bifunctional glycosyltransferase and transpeptidase activity (Suzuki, Nishimura et al. 1978; Sung, Lai et al. 2009).

The PG synthesis activities of FtsI and PBP1b are regulated by interactions with FtsW, FtsN, and the FtsQLB complex (Egan and Vollmer 2013). The function of the FtsQLB complex is least understood among these divisome proteins, but recent findings that the *Staphylococcus aureus*

FtsQ homolog (DivIB) can directly bind PG (Bottomley, Kabli et al. 2014) suggests a direct role in sensing or modifying PG structure. One established role of FtsQLB is the recruitment of FtsW to midcell (Mercer and Weiss 2002). FtsW is an integral membrane protein (Lara and Ayala 2002) that is required for the recruitment of FtsI to midcell (Mercer and Weiss 2002; Pastoret, Fraipont et al. 2004). The interactions that establish this recruitment may allow FtsW to regulate FtsI activity during PG synthesis. Originally, FtsW was given a more definite role in PG synthesis when it was classified as the flippase that transfers lipid II, a cell wall precursor, from the inner leaflet of the inner membrane to the outer leaflet (Mohammadi, van Dam et al. 2011). However, recent work suggests that lipid II is transferred by the protein MurJ rather than FtsW (Sham, Butler et al. 2014). Thus, the full role of FtsW in PG synthesis remains unclear.

FtsN is one of the most abundant periplasmic divisome proteins, at ~ 1000 copies per cell (Aarsman, Piette et al. 2005). Through its interaction with FtsA, FtsN serves as the major connection point between the cytoplasmic Z-ring scaffold and the downstream periplasmic proteins (Figure 1.2). In addition to these extensive protein-protein interactions, FtsN is able to bind PG through its SPOR domain (Ursinus, van den Ent et al. 2004; Gerding, Liu et al. 2009; Arends, Williams et al. 2010). This ability of FtsN to interact with the Z-ring, downstream divisome proteins, and PG suggest that it may be primed to serve two roles. First, its ability to sense whether all parts of the divisome have 'matured' (recruited all necessary components) would allow it to serve as an ideal trigger for cell constriction (Lutkenhaus 2009; Weiss 2015). Second, FtsN may serve in a quality control role to ensure that septal PG is well-formed during the progress of constriction (Gerding, Liu et al. 2009). This role is supported the fact that FtsN overexpression leads to a prolonged constriction time (Aarsman, Piette et al. 2005).

The chromosomal linkage

The third group of divisome proteins (Figure 1.1 and Figure 1.2, magenta) links the divisome to the chromosome to coordinate cell wall constriction with chromosome segregation. The first identified protein in this category was FtsK, which is a transmembrane protein (Bigot, Saleh et al. 2005) that interacts with and recruits many periplasmic divisome components (Figure 1.2). The cytoplasmic domain of FtsK is an AAA+ ATPase with DNA translocation activity (Vale 2000; Aussel, Barre et al. 2002; Bigot, Saleh et al. 2005) that aids in chromosome dimer resolution (Aussel, Barre et al. 2002) and efficient chromosome segregation (Liu, Draper et al. 1998; Stouf, Meile et al. 2013).

Recently, another DNA-binding protein, MatP, was identified as a component of the divisome through its interaction with the divisome protein, ZapB (Mercier, Petit et al. 2008; Espeli, Borne et al. 2012) (Figure 1.2). ZapB forms polymeric structures that interact with ZapA to promote proper Z-ring organization at midcell (Galli and Gerdes 2010; Galli and Gerdes 2012; Buss, Coltharp et al. 2013). Together, FtsZ, ZapA, and ZapB form a multi-layered protein network which is connected to the chromosome via the ZapB-MatP interaction (Buss, Coltharp et al. 2015). This connection plays an important role in positioning the Z-ring properly at midcell and in coordinating cell constriction with chromosome segregation (Espeli, Borne et al. 2012; Bailey, Bisicchia et al. 2014; Buss, Coltharp et al. 2015).

Proposed Force Generation Mechanisms

Among the three groups of divisome proteins, the Z-ring has been regarded as the primary force generator—its contraction is thought to actively drive inner membrane invagination, which is then followed by new septal PG growth (Erickson, Anderson et al. 2010). This primary role for

FtsZ in constrictive force generation is suggested by FtsZ's homology with eukaryotic tubulin, GTPase activity, nucleotide-dependent polymerization, and wide genetic conservation among bacteria (Erickson, Anderson et al. 2010). Experimentally, this role is supported by *in vitro* observations that purified, membrane-tethered FtsZ can assemble into ring-like structures to deform and constrict liposome membranes (Osawa, Anderson et al. 2008; Osawa, Anderson et al. 2009; Osawa and Erickson 2011) (Osawa and Erickson 2013; Szwedziak, Wang et al. 2014).

The cytoskeletal homology of FtsZ naturally suggested that bacteria may utilize a motor-driven cytokinetic ring analogous to the eukaryotic actomyosin ring, and initially prompted a period of unfruitful search for a Z-ring-associated motor protein (Bramhill and Thompson 1994; Osawa and Erickson 2006). Today, the field has turned to more FtsZ-centric mechanisms, in which a constrictive force is generated by FtsZ alone (Erickson 2009). These proposed mechanisms by which FtsZ could generate force arise from two well-studied features of FtsZ filaments. The first is the inherent curvature of FtsZ filaments, which should cause preferential alignment of membrane-tethered filaments along the curved, circumferential cell axis rather than the straight, longitudinal axis (Erickson, Anderson et al. 2010; Sun and Jiang 2011). This inherent curvature should also cause aligned FtsZ filaments to impose a bending force when tethered to less-curved surfaces (Erickson, Anderson et al. 2010). The typical curvature radius of purified FtsZ filaments from *E. coli* is 100 nm (Chen, Bjornson et al. 2005; Gonzalez, Velez et al. 2005; Mingorance, Tadros et al. 2005), which is smaller than the typical *E. coli* cell radius (400 - 500 nm). This curvature difference indicates that FtsZ bending forces are possible *in vivo*, at least until the radius of the constricting midcell septum decreases to ~ 100 nm.

One prominent class of proposed bending mechanisms is the so-called "hydrolyze-and-bend hypothesis," which contends that chemical energy from GTP hydrolysis drives FtsZ filaments into higher curvature conformations, leading to membrane constriction (Allard and Cytrynbaum 2009; Erickson 2009). The preference of GDP-bound FtsZ for higher-curvature conformations than those of GTP-bound FtsZ is supported by electron micrographs and crystal structures of purified FtsZ (Lu, Reedy et al. 2000; Chen and Erickson 2011; Li, Hsin et al. 2013). However, *in vitro* liposome deformation is still observed using slowly-hydrolyzable GTP analogs or using FtsZ variants with negligible GTPase activity (Osawa, Anderson et al. 2008; Osawa, Anderson et al. 2009; Osawa and Erickson 2011; Szwedziak, Wang et al. 2014), suggesting that GTP hydrolysis is not required for force generation. Furthermore, genetic studies with FtsZ mutants indicate that dysfunctions due to diminished GTPase activity can be readily suppressed by mutations elsewhere in the chromosome (Mukherjee, Saez et al. 2001; Osawa and Erickson 2006). These studies suggest that cell division is not primarily driven by GTP hydrolysis, but the direct effect of GTPase activity on constriction rate has not yet been tested.

The second feature of FtsZ filaments that may provide constrictive force is their ability to associate with each other laterally (Lan, Daniels et al. 2009). The fast turnover of FtsZ filaments, combined with their lateral affinity for each other, should drive them into more condensed arrangements, maximizing the number of lateral interactions. Given a fixed number of FtsZ subunits and a fixed slice of cellular space in which they can polymerize, this condensation could generate a constrictive force tending toward smaller and smaller ring diameters (Lan, Daniels et al. 2009). *In vivo*, condensation of FtsZ filaments could additionally be driven by proteins shown to promote Z-ring bundling: ZapA (Gueiros-Filho and Losick 2002; Low, Moncrieffe et al. 2004; Small, Marrington et al. 2007; Mohammadi, Ploeger et al. 2009; Dajkovic, Pichoff et al. 2010),

ZipA (RayChaudhuri 1999; Hale, Rhee et al. 2000), and FtsA (Dai and Lutkenhaus 1992; Pichoff and Lutkenhaus 2002). Evidence that over-expression of any of these proteins leads to disruption of normal cell division (Dai and Lutkenhaus 1992; Ma, Ehrhardt et al. 1996; Hale and de Boer 1997; Galli and Gerdes 2012) suggests that an overly-dense Z-ring may not be functional (Lan, Daniels et al. 2009), but the influence of FtsZ density on constriction progress has not been directly assessed.

Importantly, the bending- and condensation-induced forces are not mutually exclusive, and have been combined in computation models (Ghosh and Sain 2008; Horger, Velasco et al. 2008; Surovtsev, Morgan et al. 2008; Paez, Mateos-Gil et al. 2009). Furthermore, these FtsZ-centric mechanisms most likely also exist within the context of other force-generation systems *in vivo*. The Z-ring may deform the inner membrane and guide the positioning of periplasmic divisome proteins, which in turn direct inward growth of peptidoglycan and generate a pushing force at midcell (Lan, Wolgemuth et al. 2007; Meier and Goley 2014). Observations that cell wall constriction is stalled in the absence of peptidoglycan remodeling indeed argue for a substantial contribution from the peptidoglycan remodeling machinery in cell wall constriction (Wientjes and Nanninga 1989; Pogliano, Pogliano et al. 1997). However, the relative contribution, and thus physiological relevance, of either the FtsZ-centric force or that provided by peptidoglycan synthesis and remodeling remains unknown.

Although FtsZ-centric constrictive force generation has been the prevailing hypothesis in the field, these proposed mechanisms have been difficult to test *in vivo* due to the essentiality of FtsZ, the limited ability to spatially resolve the small Z-ring structure, and the lack of sensitive methods to monitor Z-ring contraction and septum closure rates during constriction. Thus, in

the following work, superresolution fluorescence microscopy was applied to resolve both Z-ring structure and septum closure rates with high precision.

Chapter 2 :

**Contributions of the Z-ring, cell wall synthesis
and chromosome segregation in driving *E. coli*
cytokinesis**

Introduction

This chapter describes the application of quantitative superresolution imaging in combination with other biophysical techniques and genetic manipulations to determine whether the Z-ring indeed plays a rate-limiting role in driving cell wall constriction in *E. coli* cells. These analyses revealed that the rate of septum closure is unaffected by many substantial alterations to the Z-ring. These alterations include FtsZ's GTPase activity, FtsZ density in the Z-ring, the timing of Z-ring disassembly, and the absence of Z-ring assembly regulators. Instead, the rate of septum closure was determined to be proportional to the rate of cell elongation prior to and during constriction. This finding suggests that cell wall PG synthesis, the activity carried out by the second group of divisome proteins, plays a limiting role in septum closure. Furthermore, in the absence of MatP, a key chromosome-binding protein in the third group of divisome constituents, the septum closes significantly faster than the corresponding cell elongation rate. This effect cannot be explained by altered Z-ring structure, density, or dynamics, thus indicating a significant role for chromosome segregation in regulating septum closure.

Taken together, the results described below challenge the FtsZ-centric view of constrictive force generation, highlight the role of septal PG synthesis and chromosome segregation in driving and modulating septum closure during constriction, and support a holistic view of constrictive force generation by the divisome.

Results

3D structure of the *E. coli* Z-ring

As described in Chapter 1, proposed Z-ring force generation models predict that Z-ring structure would be remodeled in different ways during constriction (i.e. thickening (Ghosh and Sain 2011),

widening (Horger, Velasco et al. 2008), condensing (Lan, Daniels et al. 2009), or disassembly (Ghosh and Sain 2008; Surovtsev, Morgan et al. 2008; Allard and Cytrynbaum 2009)). To determine whether the Z-ring undergoes such structural remodeling *in vivo*, the single-molecule based superresolution technique, photoactivated localization microscopy (PALM)(Betzig, Patterson et al. 2006) was applied. Previously, two-dimensional (2D) PALM imaging of the *E. coli* Z-ring was conducted using a photoactivatable fluorescent protein fusion FtsZ-mEos2 (Fu, Huang et al. 2010; Coltharp, Kessler et al. 2012; Buss, Coltharp et al. 2013; Buss, Coltharp et al. 2013; Buss, Coltharp et al. 2015). Those studies showed that the Z-ring is not a smooth structure, but instead comprises clusters of FtsZ protofilaments that loosely associate into a three-dimensional (3D) bundle(Fu, Huang et al. 2010; Buss, Coltharp et al. 2013). This heterogeneous morphology has also been observed with several different fluorescent protein tags(Buss, Coltharp et al. 2013), in different bacterial species (Leisch, Verheul et al. ; Strauss, Liew et al. 2012; Holden, Pengo et al. 2014; Rowlett and Margolin 2014), by immuno-superresolution imaging targeting native FtsZ (Leisch, Verheul et al. 2012; Buss, Coltharp et al. 2013; Coltharp, Buss et al. 2015), and by superresolution imaging of FtsZ-binding proteins (Buss, Coltharp et al. 2013; Rowlett and Margolin 2014; Coltharp, Buss et al. 2015), and in an early electron cryotomography (ECT) study (Li, Trimble et al. 2007). Figure 2.1 further demonstrates that an FtsZ-GFP fusion co-localizes with native FtsZ in midcell clusters by performing two-color superresolution imaging using antibodies against native FtsZ and GFP. These new results further indicate that the cluster-like organization of the Z-ring is not caused by fluorescent protein fusion, but is likely an intrinsic property of FtsZ polymerization and dynamics *in vivo*.

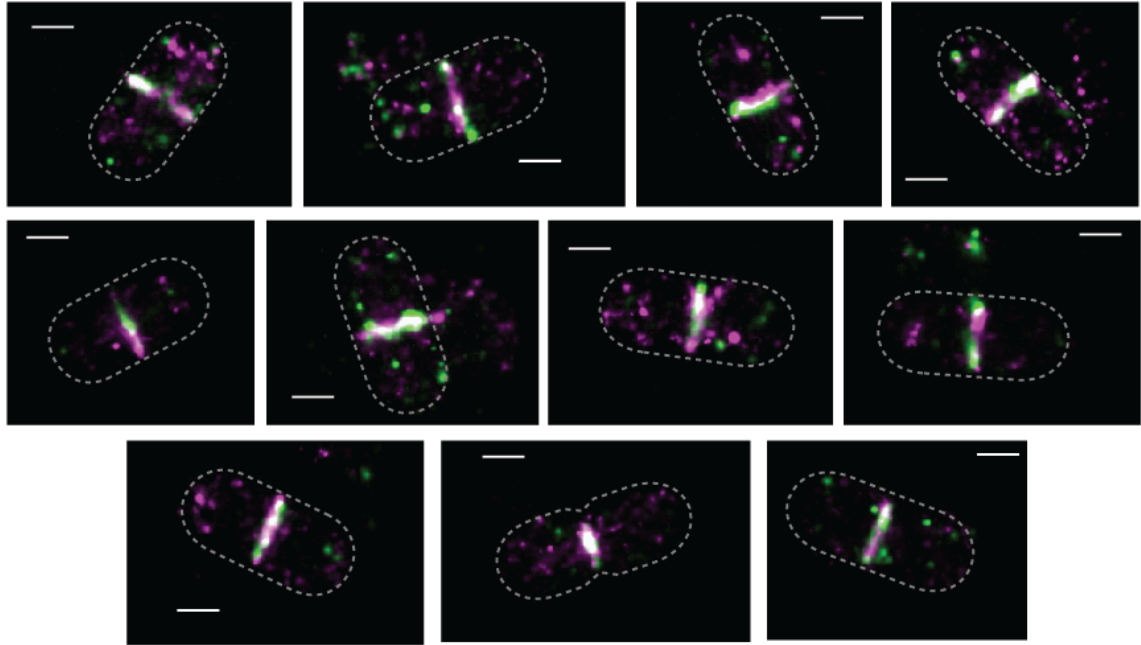


Figure 2.1 Two-color immuno-superresolution imaging of FtsZ and FtsZ-GFP.

Representative images are shown of wt *E. coli* BW25113 cells expressing FtsZ-GFP labeled with rabbit anti-FtsZ and mouse anti-GFP primary antibodies, then Alexa Fluor® 568 goat anti-rabbit (magenta) and Alexa Fluor® 488-goat anti-mouse (green) secondary antibodies. White regions indicate co-localization of labeled FtsZ and FtsZ-GFP. Cell boundaries are approximated by gray dotted outlines. Scale bars, 500 nm.

To provide a nanoscale characterization of the Z-ring structure in 3D, iPALM (interferometric PALM) imaging (Shtengel, Galbraith et al. 2009; Buss, Coltharp et al. 2015) was applied to *E. coli* Z-rings labeled with FtsZ-mEos2. iPALM identifies a molecule's z-position using the interference of its emitted light along two optical paths and provides the best z-resolution currently available to fluorescence-based superresolution imaging (Klein, Proppert et al. 2014). Using the mEos2 fusion protein, spatial resolutions of ~33 nm, ~26 nm, and ~ 18 nm in the x, y, and z, dimensions, respectively, were achieved (Table 2.1, Figure 2.2).

Table 2.1 Spatial resolution and Z-ring dimensions from iPALM and PALM measurements.

a. 3D fixed iPALM									
strain	media	fusion construct	resolution FWHM (nm)				n	apparent ring width FWHM (nm)	apparent ring thickness FWHM (nm)
			x	y	z				
DH5α wt	M9	FtsZ-mEos2	28	22	16	105	103 ± 3	67 ± 2	
BW25113 wt	M9	FtsZ-mEos2	32	23	16	63	104 ± 4	61 ± 2	
BW25113 wt	M9	mEos2-ZapA	29	26	17	43	90 ± 4	54 ± 2	
b. Live-cell 2D PALM									
strain	media	fusion construct	resolution FWHM (nm)		n	apparent ring width FWHM (nm)	deconvolved ring width FWHM ^a (nm)		
			xy						
BW25113 wt	M9	FtsZ-mEos2	55		81	93 ± 2	73 ± 3		
BW25113 wt	M9	mEos2-ZapA	41		126	79 ± 2	67 ± 2		
BW25113 wt	EZ-RDM	FtsZ-mEos2	44		59	85 ± 2	71 ± 3		
DH5α wt	M9	FtsZ-mEos2	60		116	107 ± 2	87 ± 3		
BW25113 <i>ΔminC</i>	M9	FtsZ-mEos2	51		100	94 ± 2	78 ± 2		
BW25113 <i>ΔmatP</i>	M9	FtsZ-mEos2	41		112	84 ± 2	73 ± 3		
MC4100 wt	M9	FtsZ-mEos2	59		98	95 ± 3	71 ± 4		
MCZ84 <i>ftsZ84</i>	M9	FtsZ84-mEos2	51		219	91 ± 2	73 ± 2		

^a The deconvolved FWHM allows comparison of dimensions acquired with varying spatial resolutions (see Materials and Methods).

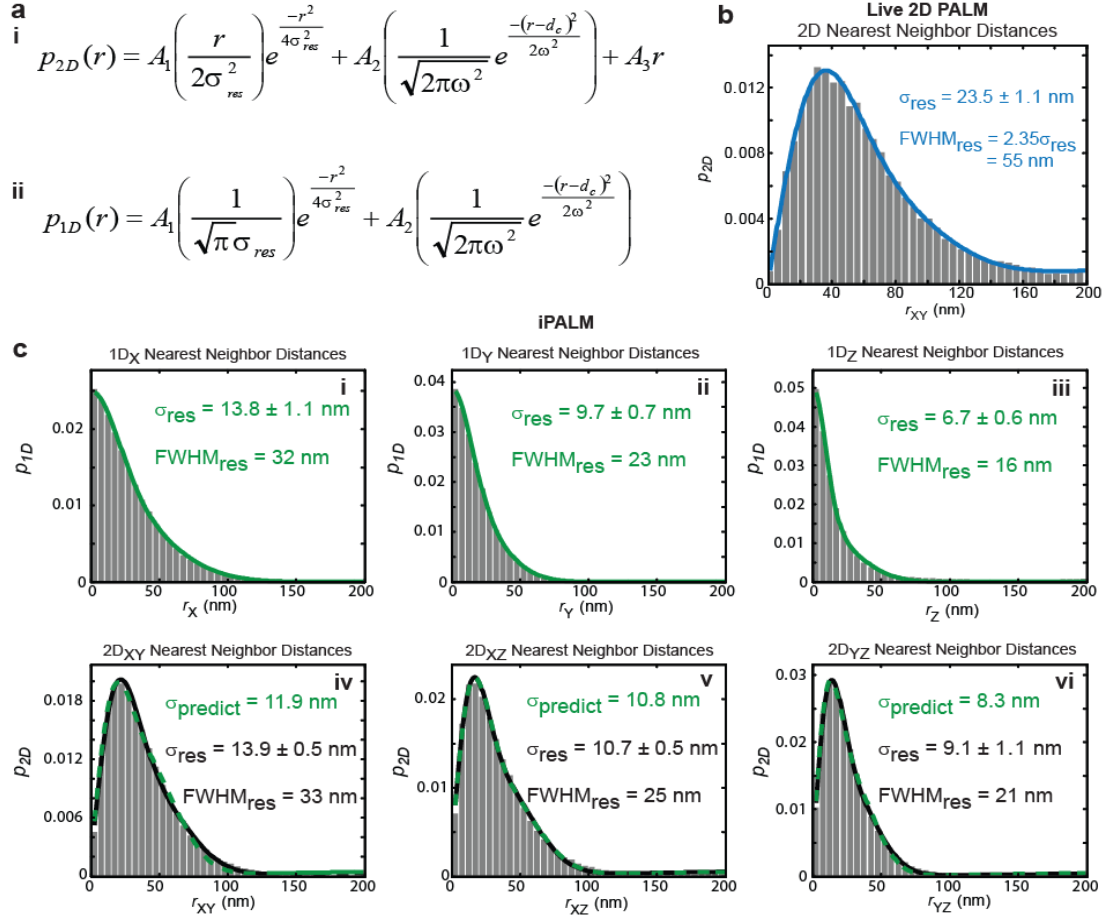


Figure 2.2 Measurement of spatial resolution.

(a) Equations describing the distribution (p) of distances (r) between nearest neighbors in adjacent frames of live PALM or iPALM data with a given localization precision, σ_{res} . The equation for distances measured using two dimensions (p_{2D}) (i) was adapted by Endesfelder *et al.* (Endesfelder, Malkusch *et al.* 2014) from the distribution of 2D distances expected for repeat localizations of the same molecule (Churchman, Flyvbjerg *et al.* 2006; Coltharp, Kessler *et al.* 2012) to account for the possibility that a localization's nearest neighbor in an adjacent frame may be a different molecule. This adaptation is represented in the 2nd and 3rd terms of the equation in (i) by the Gaussian parameters ω and d_c , and the relative weighting factors A_1 , A_2 , and A_3 . Because the spatial resolution in iPALM measurements is not isotropic, here the equation describing distances measured in one dimension (p_{1D}) (ii) was adapted in the same manner from the expected distribution of 1D distances between repeat localizations of the same molecule (Churchman, Flyvbjerg *et al.* 2006) with analogous parameters ω , d_c , A_1 , and A_2 . This new equation allows separate measurement of the X, Y, and Z resolutions. (b) Representative distribution of XY distances between nearest neighbors in adjacent frames (gray bars) for 2D PALM localizations FtsZ-mEos2 in live BW25113 cells. The distribution was fit (blue) with the equation in (ai) to yield a Gaussian localization precision of $\sigma_{res} = 23.5 \pm 1.1 \text{ nm}$, which corresponds to a spatial resolution (FWHM of the Gaussian localization precision) of 55 nm. (c) Representative distributions of X (i), Y(ii), Z (iii), XY(iv), XZ (v), and YZ (vi) distances between nearest neighbors in adjacent frames (gray bars) for 3D iPALM localizations of FtsZ-mEos2 in fixed BW25113 cells. The 1D distributions (i - iii) were fit with the equation in (a(ii)) to generate the green curves and σ_{res} values of $13.8 \pm 1.1 \text{ nm}$, $9.7 \pm 0.7 \text{ nm}$, and $6.7 \pm 0.6 \text{ nm}$ in X, Y, and Z, respectively. These correspond to resolution values of 32 nm, 23 nm, and 16 nm, respectively. The 2D distributions (iv - vi) were fit with the equation in (ai) to generate the black curves and σ_{res} values of $13.9 \pm 0.5 \text{ nm}$, $10.7 \pm 0.5 \text{ nm}$, and $9.1 \pm 1.1 \text{ nm}$ in the XY, XZ, and YZ planes, respectively. These 2D σ_{res} should represent the root-mean-square (RMS) average ($\sigma_{predict}$) of the 1D σ_{res} values. The best fit to each 2D distribution using a fixed $\sigma_{predict}$ value is shown as the dashed green line. The similarity between the $\sigma_{predict}$ and fitted 2D σ_{res} values in (iv - vi) validates the relationship between the equations in (a).

Figure 2.3 shows representative iPALM images of fixed *E. coli* BW25113 and DH5 α cells ectopically expressing FtsZ-mEos2. These images show the punctate structure of the Z-ring, which is normally blurred into a smooth ring when viewed under a conventional fluorescence microscope (Fu, Huang et al. 2010; Buss, Coltharp et al. 2013). Interestingly, the images reveal non-midcell clusters of FtsZ-mEos2 located either near the cell periphery (Figure 2.3a, white arrows), or clearly displaced from the membrane (Figure 2.3a, cyan arrows), indicating the presence of oligomeric FtsZ species outside the Z-ring.

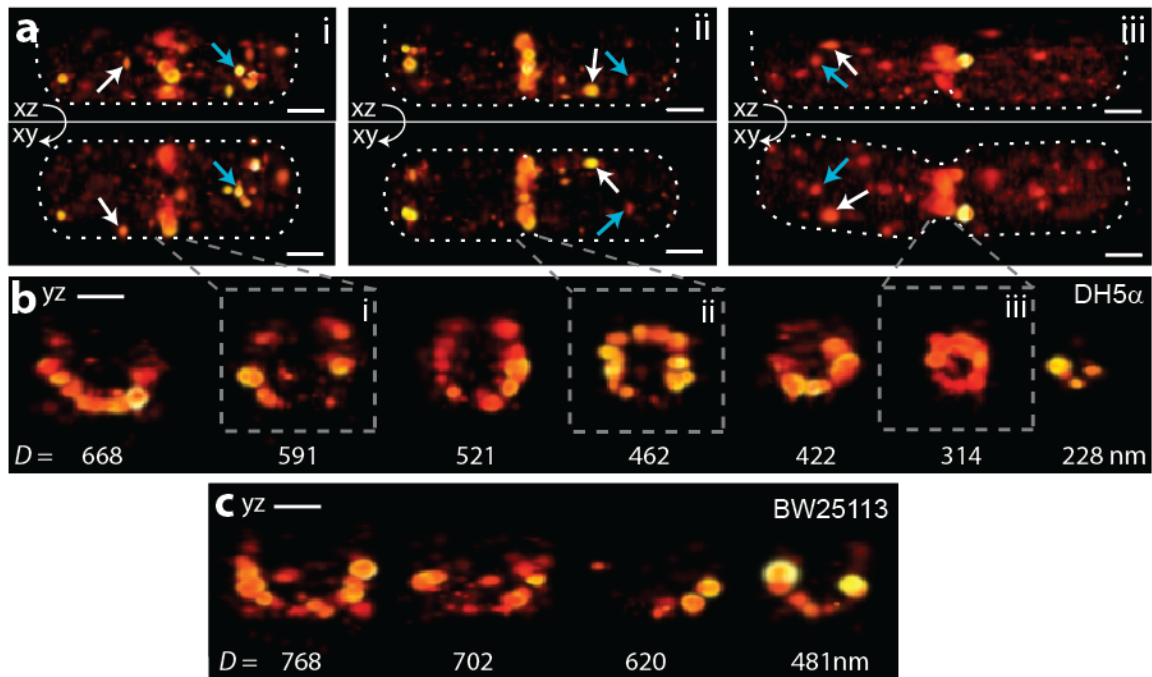


Figure 2.3 3D images of the *E. coli* Z-ring.

(a) iPALM images of three fixed DH5 α *E. coli* cells expressing FtsZ-mEos2 shown as xy (bottom) and xz (top) projections. Arrows illustrate cytoplasmic (cyan) and membrane-proximal (white) clusters of FtsZ-mEos2 outside the Z-ring. Cell outlines approximated by white dotted lines. (b) Cropped Z-rings of DH5 α cells shown as yz projections. Fitted ring diameters are shown below each Z-ring. Rings outlined in dashed boxes correspond to those shown in (a). (c) Cropped Z-rings of BW25113 cells shown as yz projections. Fitted ring diameters are shown below each Z-ring. Scale bars, 300 nm.

The cluster-like distributions of FtsZ-mEos2 within the ring are more apparent when the cropped midcell regions are projected onto the cell cross-section (Figure 2.3b-c). These projections show that FtsZ clusters are confined to a toroidal zone that defines the Z-ring. The apparent width and thickness of this zone was similar in the two *E. coli* strains (Table 2.1), with a combined mean Z-ring width of 103 ± 3 nm ($n = 168$, Figure 2.4a), consistent with previous measurements of 60 - 120 nm in *E. coli* (Fu, Huang et al. 2010; Carmon, Fishov et al. 2012; Buss, Coltharp et al. 2013) and *C. crescentus* (Biteen, Goley et al. 2012; Holden, Pengo et al. 2014). The mean Z-ring thickness in the radial direction was significantly smaller than the width (65 ± 1 nm, $p < 1 \times 10^{-30}$, $n = 168$, Figure 2.4a), but larger than the resolution-limited size of a single protofilament layer (< 35 nm). This result suggests that the Z-ring can accommodate multiple layers of FtsZ protofilaments along the radial direction of the cell.

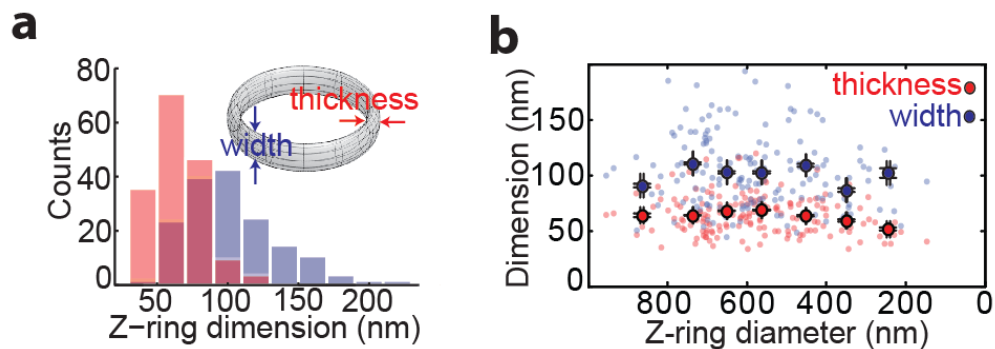


Figure 2.4 Z-ring dimensions.

(a) Distributions of Z-ring width (blue) and thickness (red) ($n = 168$) measured from iPALM images of FtsZ-mEos2 in DH5 α and BW25113 cells. Each histogram bin width is 20 nm. (b) Measured Z-ring width (blue) and thickness (red) plotted against corresponding Z-ring diameter ($n = 168$). Measurements for individual cells are shown as small, transparent, filled circles. Average measurements for cells binned by ring diameter (bin edges: 0, 300, 400, 500, 600, 700, 800, and 1000 nm) are shown as larger filled circles with black outlines. Error bars represent standard error of the mean.

To characterize the size and distribution of FtsZ clusters, autocorrelation and density histogram analyses (Veatch, Machta et al. 2012; Sengupta, Jovanovic-Talisman et al. 2013; Coltharp, Yang et al. 2014) of FtsZ clusters projected along the Z-ring's circumference were performed. These distributions were well-described by a model in which, on average, 10 - 20 FtsZ clusters (μm^{-1}) of 30 – 50 nm length (FWHM) are randomly distributed along the Z-ring (Figure 2.5). Confinement of these clusters to a $\sim 65 \times 100$ nm Z-ring cross-section (Table 2.1) indicates that FtsZ filaments typically do not grow longer than 100 nm in any direction, consistent with the 100 - 200 nm protofilament length observed *in vitro* (Romberg, Simon et al. 2001; Chen, Bjornson et al. 2005; Huecas, Llorca et al. 2008).

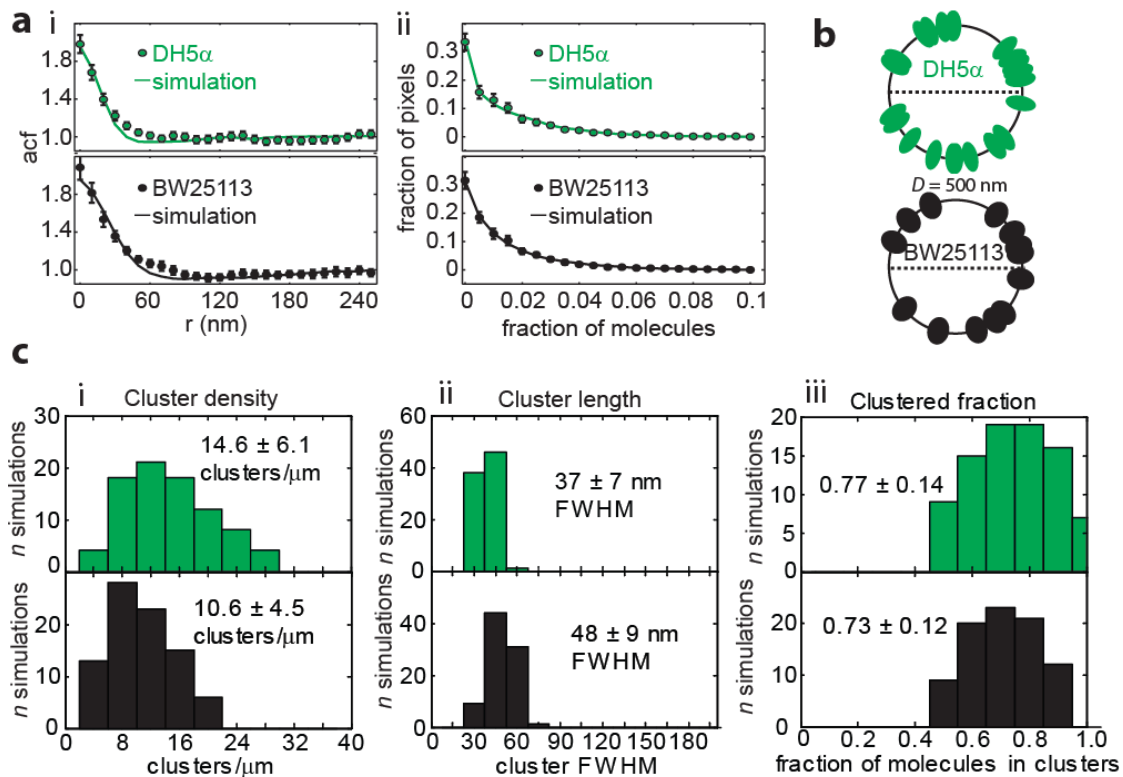


Figure 2.5 Cluster simulations that best replicate Z-rings observed by iPALM.

(a) Similarity between cluster simulations (see Supplementary Note 1 for simulation description) and the true distribution of molecules with the Z-ring was assessed using two measurements: (i) the spatial autocorrelation (acf) of molecule density along each ring's circumference, and (ii) the probability distribution of molecule density (calculated as the fraction of a single Z-ring's molecules residing in each 10 nm stretch of Z-ring circumference). The average distributions for experimental Z-rings are shown as filled circles for FtsZ-mEos2 expressed in DH5 α (green, $n = 100$) and BW25113 (black, $n = 60$) cells. The distributions arising from the best-fit simulation (lowest combined residuals for the acf and density distribution out of 8,500 simulations) is shown as correspondingly-colored solid lines. For DH5 α , the best-fit simulation was generated using a 13 cluster/ μm density and 32.5 nm cluster length with 75% of Z-ring molecules located in clusters and the remainder distributed uniformly around the ring. For BW25113, the best-fit simulation was generated using a 7 cluster/ μm density and 47.5 nm cluster length with 70% of Z-ring molecules located in clusters and the remainder distributed uniformly around the ring. (b) Schematic representations of the best fit simulations in (a), which define the typical spacing of the randomly-distributed clusters and their lengths along the circumference. The radial thickness of clusters in the schematic was defined by the average measured Z-ring thickness for each strain (Table 2.1). Although both cluster length and Z-ring thickness were defined as FWHM of normal distributions, these schematics depict the 95-percentile dimensions calculated from those FWHM values to better resemble the visualization of iPALM data as in Figure 1. (c) Distribution of cluster simulation parameters (i: cluster density, ii: cluster length, and iii: clustered fraction) for simulations with combined SSE values in the lowest 1 percentile (85 out of 8,500 simulations). These distributions are well-defined near the best fit values (a). Limits of the x-axes in (c) are defined by the parameter space sampled by all simulations.

Z-ring width and thickness remain constant during contraction

To investigate whether the Z-ring cross-sectional dimensions change during its contraction, pseudo time-lapse sequences were generated by arranging individual Z-rings according to their diameters (representative images shown in Figure 2.3b-c). Qualitative inspection shows that the Z-ring remains heterogeneous throughout the course of Z-ring contraction, and that the ring does not appreciably expand or decrease in size. Plotting measured Z-ring width and thickness values against the corresponding ring diameters of individual cells confirms that both dimensions remain largely constant during ring contraction (Figure 2.4b).

To verify that the observed trend is representative of native, unlabeled FtsZ, a similar analysis was performed on the ring structures formed by the Z-ring associated protein, ZapA, using an mEos2-ZapA fusion protein (Buss, Coltharp et al. 2015). ZapA binds to FtsZ to promote Z-ring assembly (Small, Marrington et al. 2007; Dajkovic, Pichoff et al. 2010), and has been used as a marker for FtsZ localization and dynamics (Monahan, Robinson et al. 2009; Peters, Dinh et al. 2011). Previously, the mEos2-ZapA fusion protein was shown to rescue the elongated cell phenotype of the *zapA* null mutant (Buss, Coltharp et al. 2015). iPALM images of mEos2-ZapA showed punctate structures similar to those of FtsZ-mEos2 (Figure 2.6a) (Buss, Coltharp et al. 2015). Dimension measurements revealed that these mEos2-ZapA clusters are confined to a zone of slightly smaller size than that of FtsZ-mEos2 (mean width of 90 ± 4 nm and thickness of 54 ± 2 nm, $n = 43$, Table 2.1, Figure 2.6b). Importantly, no significant changes in either the width or thickness of ZapA-rings were observed across cells of different diameters (Figure 2.6c), confirming that the Z-ring cross-sectional dimensions remain constant during ring contraction.

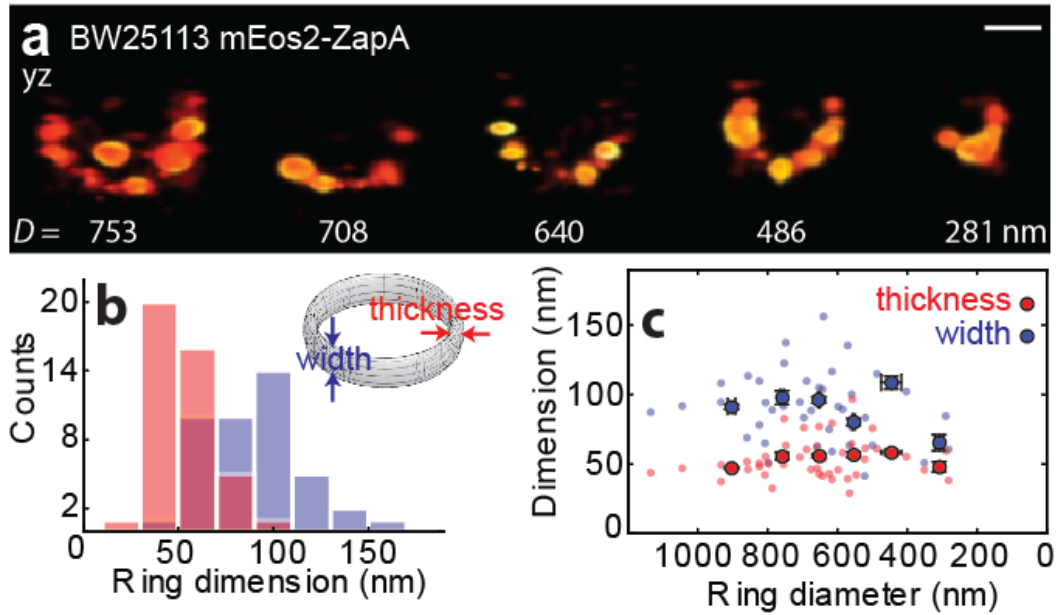


Figure 2.6 3D images and dimensions of ZapA-rings.

(a) iPALM images of cropped rings formed by mEos2-ZapA in BW25113 cells shown as yz projections. Fitted ring diameters are shown below each Z-ring. (b) Distributions of measured ZapA-ring width (blue) and thickness (red) ($n = 43$). (c) Measured ZapA-ring width (blue) and thickness (red) plotted against corresponding ring diameter ($n = 43$) showing that both dimensions remain stable throughout ring. Measurements for individual cells are shown as small, transparent, filled circles. Average measurements for cells binned by ring diameter (bin edges: 0, 400, 500, 600, 700, 800, and 1200 nm) are shown as larger filled circles with black outlines. Error bars represent standard error of the mean.

The Z-ring contracts in two apparent phases

iPALM imaging revealed the structure of the Z-ring during contraction with high precision, but the nature of fixed-cell imaging does not allow examination of the time course of Z-ring contraction during the cell cycle. Therefore, time-lapse fluorescence imaging was performed on dividing BW25113 cells expressing FtsZ-GFP (Figure 2.7a). Figure 2.7b shows a representative time trace in which the percentage of FtsZ-GFP localized to the midcell is plotted against cell cycle time for a single cell. This percentage value normalizes for FtsZ expression levels in different cells and has been used as an indicator of the amount of FtsZ in the Z-ring (Anderson, Gueiros-Filho et al. 2004; Geissler, Shiomi et al. 2007; Fu, Huang et al. 2010), as it is unaffected

by overexpression of up to 8-fold the endogenous FtsZ level (Fu, Huang et al. 2010), and the expression level of FtsZ throughout the cell cycle is constant (Rueda, Vicente et al. 2003; Weart and Levin 2003). The total expression level of FtsZ (endogenous FtsZ + FtsZ-mEos2, or endogenous FtsZ + FtsZ-GFP) in this study was generally less than 2-fold the endogenous FtsZ level (see Materials and Methods).

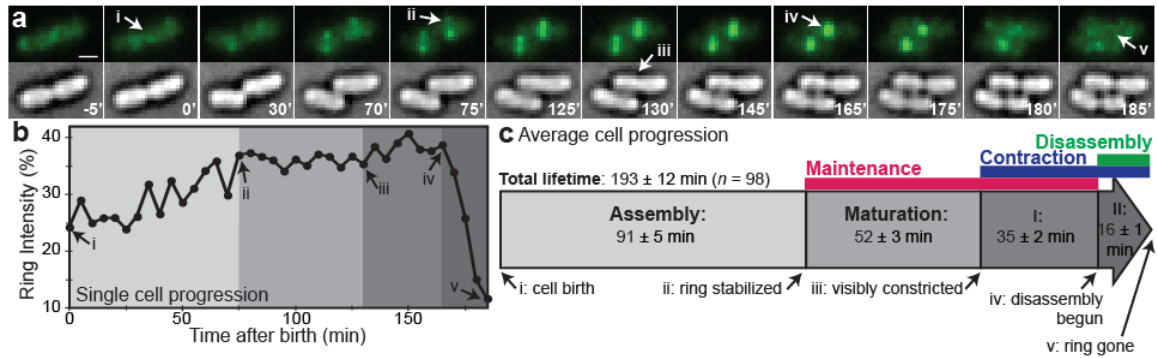


Figure 2.7 Time-lapse analysis of Z-ring dynamics during the cell cycle.

(a) Time-lapse fluorescence (top) and bright-field (bottom) montage of BW25113 *E. coli* expressing FtsZ-GFP. Arrows indicate cell cycle landmarks for the top cell: i, cell birth; ii, ring stabilization; iii, onset of visible constriction; iv, beginning of Z-ring disassembly; v, completion of cell division. Time-stamp (bottom right) displayed as minutes relative to cell birth. (b) Time-dependent Z-ring fluorescence (percentage of fluorescence in the ring relative to that of the whole cell) during the cell cycle of the top cell shown in (a). (c) Average durations of each cell cycle period for BW25113 cells growing in M9 medium at room temperature. Scale bar, 1 μ m.

The mean cell cycle time of BW25113 cells under this growth condition (room temperature (RT), M9 medium) is $\tau = 193 \pm 12$ min ($n = 98$, Table 2.2). Based on the fluorescence measurement, Z-ring dynamics during the cell cycle can be divided into three periods as observed previously (Erickson, Anderson et al. 2010; Tsukanov, Reshes et al. 2011): Z-ring Assembly (the time between cell birth and stabilization of the Z-ring at midcell), Z-ring Maintenance (during which Z-ring intensity remains largely constant), and Z-ring Disassembly (during which Z-ring intensity decreases, concluded by cell separation) (Figure 2.7c). Interestingly, corresponding bright-field images of cell contours revealed that visible indentation of the cell wall (Figure 2.7a, iii) does not coincide with, but precedes, the Z-ring Disassembly period (Figure 2.7a, iv) by 35 ± 2 min, on

average. Note that cell wall constriction actually initiates earlier than can be detected with diffraction-limited identification of cell wall indentation (Reshes, Vanounou et al. 2008). Thus, Z-ring contraction and septum closure begin prior to Z-ring disassembly, suggesting that GTPase-induced Z-ring disassembly does not drive septum closure as previously proposed in some theoretical models (Ghosh and Sain 2008; Surovtsev, Morgan et al. 2008; Allard and Cytrynbaum 2009).

Table 2.2 Durations of Z-ring cell cycle periods.

strain	media	<i>n</i>	Assembly ^a min (% cycle)	Maturation ^{a,b} min (% cycle)	Contraction I ^{a,b} min (% cycle)	Contraction II ^{a,c} min (% cycle)	τ ^d min
BW25113 wt	M9	98	91 ± 5 (45 ± 1)	52 ± 3 (27 ± 1)	35 ± 2 (19 ± 1)	16 ± 1 (9 ± 1)	193 ± 12
MC4100 wt	M9	78	51 ± 3 (42 ± 2)	32 ± 2 (29 ± 2)	22 ± 1 (20 ± 1)	10 ± 1 (9 ± 1)	114 ± 3
DH5 α wt	M9	40	96 ± 8 (51 ± 2)	54 ± 4 (31 ± 2)	17 ± 2 (10 ± 1)	14 ± 1 (8 ± 1)	181 ± 8
BW25113 wt	EZ- RDM	80	39 ± 3 (39 ± 2)	27 ± 2 (30 ± 2)	16 ± 1 (18 ± 1)	13 ± 1 (14 ± 1)	94 ± 2
MCZ84 <i>ftsZ84</i>	M9	77	66 ± 5 (51 ± 2)	25 ± 2 (21 ± 2)	19 ± 1 (16 ± 1)	13 ± 1 (11 ± 1)	123 ± 4
BW25113 Δ <i>matP</i>	M9	37	114 ± 10 (53 ± 3)	54 ± 5 (27 ± 2)	25 ± 3 (13 ± 1)	15 ± 1 (8 ± 1)	208 ± 9
BW25113 Δ <i>minC</i>	M9	45	108 ± 7 (50 ± 3)	51 ± 5 (24 ± 3)	36 ± 3 (17 ± 1)	19 ± 1 (9 ± 1)	215 ± 8

^a. Durations of cell cycle periods measured from time-lapse analyses as in Figure 2.7. All values listed as mean ± standard error.

^b. Combined duration of Maturation and Contraction I periods constitute the Z-ring Maintenance period.

^c. Contraction II is equivalent to the Z-ring Disassembly period.

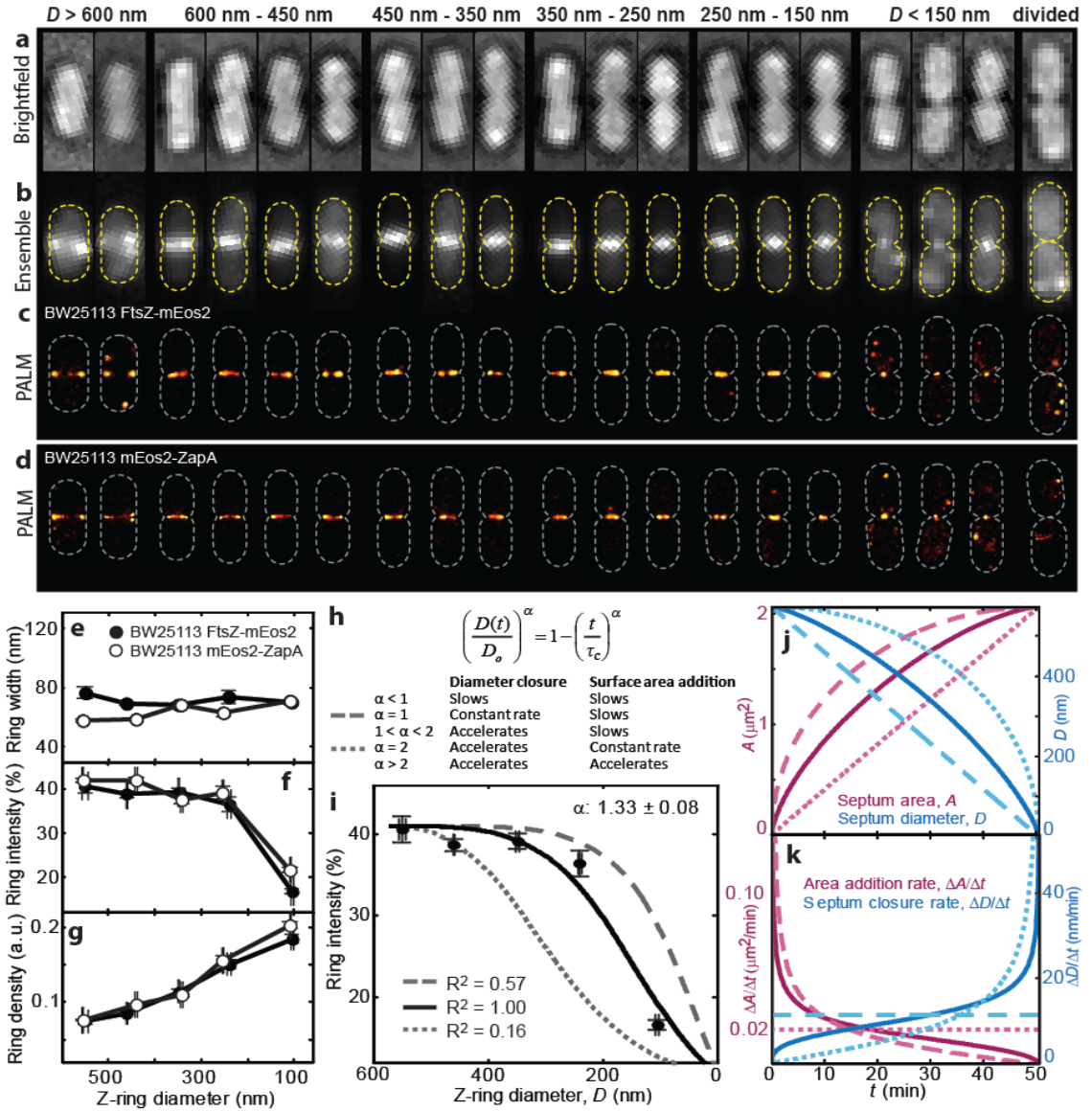
^d. Total cell lifetime.

To facilitate the description of this process, the period between the first visible cell wall indentation until the initiation of Z-ring disassembly will be referred to as Z-ring Contraction Phase I, and the subsequent Z-ring Disassembly period as Contraction Phase II. Note that by using this terminology, the Z-ring Maintenance period has been divided into two apparent phases: Z-ring Maturation and Contraction Phase I.

The Z-ring condenses as it contracts

The observation that the Z-ring contracts before disassembling suggests that Z-ring density (i.e. FtsZ concentration in the ring) likely increases during early stages of contraction. Previously it was proposed that condensation of the Z-ring, caused by favorable lateral interactions between FtsZ protofilaments, could generate a constrictive force during cell division (Lan, Daniels et al. 2009). However, quantifying Z-ring density requires measurement of both the amount of FtsZ in the Z-ring and Z-ring volume in the same cell. This was achieved by performing 2D PALM and ensemble fluorescence imaging of live cells. 2D PALM imaging allows precise measurement of Z-ring diameter, which is proportional to Z-ring volume throughout contraction as ring width and thickness do not change significantly (Figure 2.3d). This measurement, combined with measurements of FtsZ percentage at midcell from ensemble fluorescence images, provides the ability to compare relative Z-ring density at different contraction stages.

Live-cell PALM images of BW25113 expressing FtsZ-mEos2 revealed similar discontinuous, heterogeneous Z-ring morphologies (Figure 2.8c) as those in fixed-cell iPALM images (Figure 2.3a-b). The measured Z-ring width from live-cell PALM images (93 ± 2 nm, $n = 81$) also did not show any appreciable change at different diameters (Figure 2.8d), confirming the iPALM results (Figure 2.3d).



The amount of FtsZ in the Z-ring was measured as the percent of FtsZ-mEos2 fluorescence localized to midcell from ensemble images acquired prior to live PALM imaging. This measurement was made in the same manner as that in Figure 2.7b, and avoids the limited detection efficiency of PALM imaging as all fluorescent molecules are detected simultaneously in the ensemble image. The measurements revealed that the midcell percentage of FtsZ remained constant until the Z-ring diameter reached ~ 250 nm (Figure 2.8e), consistent with previous observations that the total intensity of fluorescently-labeled Z-rings stays relatively constant during early contraction (Z-ring diameter > 300 nm) in both *E. coli* (Lan, Daniels et al. 2009) and *B. subtilis* (Strauss, Liew et al. 2012) cells. In cells with smaller diameters, however, the midcell percentage of FtsZ precipitously decreased (Figure 2.8e). This behavior is consistent with that observed in time-lapse experiments (Figure 2.7b), and supports the existence of two Z-ring contraction phases.

The relative density of each ring was calculated by dividing the percentage of FtsZ-mEos2 at midcell (Figure 2.8e, y-axis) by the corresponding Z-ring diameter (x-axis), which is proportional to Z-ring volume. Figure 2.8f shows that Z-ring density continuously increases as its diameter decreases, reaching up to ~ 2.5 -fold its initial value, even as the percentage of FtsZ decreases at the end of contraction (Figure 2.8e). Identical behavior was also observed in the absence of fluorescently-labeled FtsZ using the mEos2-ZapA construct in the same BW25113 background strain (Figure 2.8e-f, empty circles), suggesting that the endogenous, unlabeled Z-ring behaves similarly. Thus, the Z-ring condenses throughout its contraction.

Measuring septum closure rate

Next, to assess whether any of the observed Z-ring behaviors play limiting roles in driving septum closure, methods to measure both the average and time-dependent septum closure rate (v_c) were established. The average septum closure rate was determined by first estimating the starting septum diameter, D_0 , as the mean Z-ring diameter measured from PALM images of cells identified to be at constriction onset by their corresponding brightfield images. The diameter of the membrane-associated Z-ring should closely reflect that of the growing septum. The starting diameter of BW25113 cells under the examined growth condition (RT, M9 medium) was determined to be $\langle D_0 \rangle = 573 \pm 27$ nm. Dividing this average D_0 by the constriction period, τ_c (Contraction Phase I + II), of individual cells observed by time-lapse microscopy results an average septum closure rate of $v_c = \langle D_0 \rangle / \tau_c = 12.5 \pm 0.4$ nm/min ($n = 98$, Table 2.3).

Table 2.3 Rates of septum closure and cell elongation.

strain	media	D_o^a	α^b	v_c^c	v_{ep}^d	v_{ec}^d	v_c/v_{ep}^e	v_c/v_{ec}^e
		nm (<i>n</i>)			nm/min	nm/min		
BW25113 wt	M9	578 ± 27 (13)	1.3 ± 0.1	12.5 ± 0.4	7.9 ± 0.3 (98)	12.1 ± 0.5 (98)	1.7 ± 0.1	1.2 ± 0.1
MC4100 wt	M9	546 ± 36 (12)	1.9 ± 0.3	19.3 ± 0.7	15.0 ± 0.4 (78)	21.2 ± 0.9 (78)	1.4 ± 0.1	1.2 ± 0.2
DH5 α wt	M9	447 ± 20 (15)	1.4 ± 0.4	17.0 ± 1.2	10.8 ± 0.4 (40)	17.5 ± 0.9 (40)	1.6 ± 0.1	1.1 ± 0.1
BW25113 wt	EZ- RDM	652 ± 34 (11)	1.3 ± 0.3	25.5 ± 1.0	18.5 ± 0.5 (80)	25.9 ± 0.9 (80)	1.4 ± 0.1	1.2 ± 0.1
MCZ84 <i>ftsZ84</i>	M9	519 ± 24 (15)	1.4 ± 0.2	18.0 ± 0.7	12.6 ± 0.4 (77)	18.1 ± 0.8 (77)	1.5 ± 0.1	1.1 ± 0.1
BW25113 Δ <i>matP</i>	M9	503 ± 26 (12)	1.4 ± 0.3	14.2 ± 0.9	6.4 ± 0.5 (37)	9.6 ± 0.7 (37)	2.4 ± 0.2	1.8 ± 0.2
BW25113 Δ <i>minC</i>	M9	496 ± 22 (12)	1.6 ± 0.6	10.2 ± 0.6	7.2 ± 0.3 (45)	13.2 ± 1.3 (45)	1.5 ± 0.1	0.9 ± 0.1

^a. D_o is average starting diameter measured from *n* PALM images.

^b. Acceleration parameter (α) fit using Equation 1 (see Methods). Reported error is 95% confidence fitting error.

^c. Average septum closure rate (v_c) measured as $\langle D_o \rangle * \langle 1/\tau_c \rangle$ where τ_c is the duration of Contraction Phase I + II (Table 2.2). Standard error value propagated from those of D_o and $1/\tau_c$.

^d. Elongation rates measured for *n* cells observed by time-lapse as $v_{ep} = \langle \Delta L_p / (\tau - \tau_c) \rangle$ and $v_{ec} = \langle \Delta L_c / \tau_c \rangle$ where ΔL_p is the change in cell length from cell birth to constriction onset and ΔL_c is the change in cell length during constriction.

^e. Ratios calculated as $\langle D_o \rangle * \langle (1/\tau_c) * (1/v_{ep}) \rangle$ or $\langle D_o \rangle * \langle (1/\tau_c) * (1/v_{ec}) \rangle$. Standard error propagated from those of D_o and $(1/\tau_c) * (1/v_{ep})$ or $(1/\tau_c) * (1/v_{ec})$.

Direct measurement of the time-dependent septum closure rate is difficult because prolonged superresolution imaging of the same cell leads to phototoxicity and is thus unreliable. This problem was circumvented by taking advantage of the fact that the same quantity, the midcell localization percentage of fluorescently labeled FtsZ (*p*), was measured in two separate

experiments against different experimental axes: cell cycle time (t) in time-lapse fluorescence imaging (Figure 2.7b) and septum diameter (D) in PALM imaging of different cells (Figure 2.8e).

These two datasets were combined using a generic, monotonic septum closure model:

$$\left(\frac{D(t)}{D_0}\right)^\alpha = 1 - \left(\frac{t}{\tau_c}\right)^\alpha \quad (1)$$

which depicts the time-dependent change in septum diameter D . In this model, D_0 is the diameter at constriction onset, τ_c is the duration of constriction, and t is the time elapsed since constriction onset. The exponent variable, α , reflects the change in closure rate over time (Figure 2.8g), with a value of $\alpha = 1$ corresponding to constant closure rate (Figure 2.8h-j, dashed lines). A value of $\alpha = 2$ corresponds to a model in which septum closure accelerates such that the rate of septum surface area addition remains constant (Figure 2.8h-j, dotted lines) (Reshes, Vanounou et al. 2008).

Simulations were performed to transform the time-lapse traces of FtsZ percentage at midcell onto the diameter axes of the live PALM data using Equation 1. Using least-squared fitting, an α value of 1.3 ± 0.1 was found to best describe the behavior of BW25113 cells under this condition (RT, M9 medium, Figure 2.8h-j, solid lines), corresponding to a rate regime where closure of the septum diameter accelerates, while addition of septum surface area decelerates during constriction (Figure 2.8h). Previous attempts to measure time-dependent septum closure rates have produced mixed results, likely because different stages of the contraction process were examined (Reshes, Vanounou et al. 2008; Stromqvist, Skoog et al. 2010).

90% reduction in FtsZ GTPase activity alters Z-ring density and dynamics, but not septum closure rate

The established methods to characterize Z-ring contraction and septum closure rates were next applied to mutations causing perturbations to Z-ring structure and function. The first examined perturbation was reduced FtsZ GTPase activity, as GTP hydrolysis-dependent FtsZ protofilament bending and/or disassembly have been prominent hypotheses for force generation by the Z-ring (Ghosh and Sain 2008; Surovtsev, Morgan et al. 2008; Allard and Cytrynbaum 2009).

Lowered GTPase activity was achieved using a mutant strain, MCZ84, which expresses an FtsZ variant (FtsZ84) from the native *ftsZ* locus (Dai, Xu et al. 1993). The G105S mutation of FtsZ84 confers a 90% reduction in GTPase activity (Bi and Lutkenhaus 1990; de Boer, Crossley et al. 1992; RayChaudhuri and Park 1992). Live-cell PALM imaging of an FtsZ84-mEos2 fusion protein expressed in MCZ84 revealed that the morphology and dimension of FtsZ84-rings were similar to those of its wt parent strain, MC4100 (Figure 2.9a-c). However, FtsZ84-rings exhibited higher midcell levels of FtsZ84-mEos2 (Figure 2.9d-e), as observed previously (Stricker, Maddox et al. 2002), resulting in higher ring densities throughout contraction (Figure 2.9f).

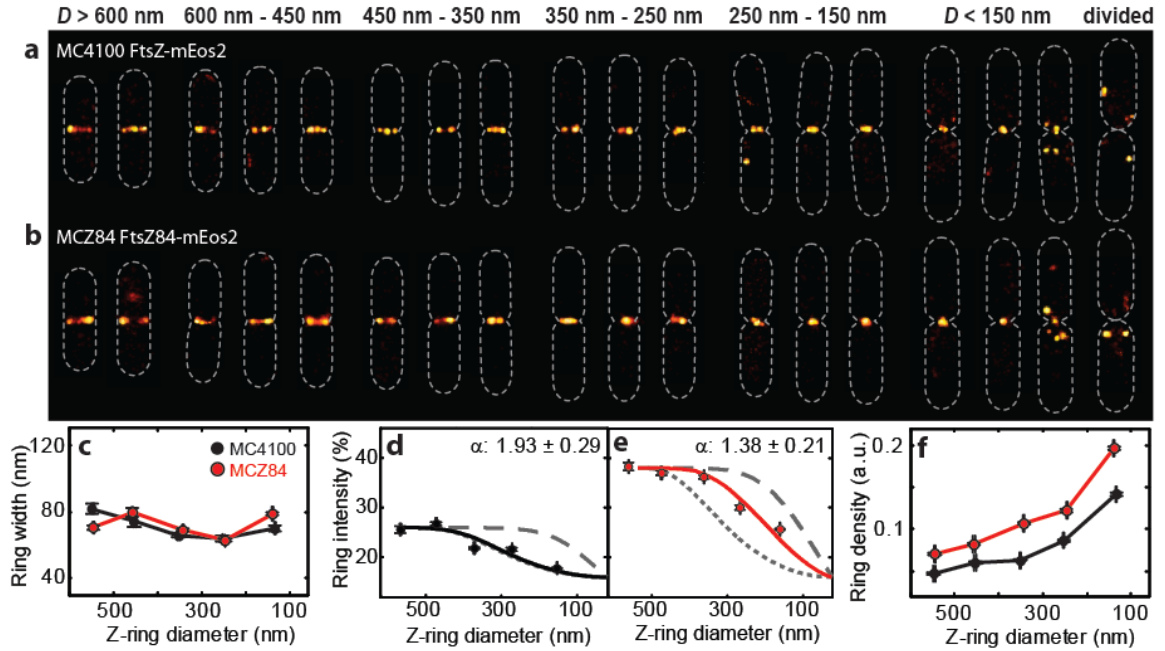


Figure 2.9 Analysis of Z-ring dimension, density, and time-dependent septum closure rate for MC4100 and MCZ84 cells.

(a-b) Superresolution PALM images of live MC4100 (a) and MCZ84 (b) cells expressing FtsZ-mEos2 or FtsZ84-mEos2, respectively, grouped by measured Z-ring diameter. Cell outlines approximated by dashed lines. (c-f) Ring width (c), intensity (d-e), and density (f) in MC4100 (black, $n = 83$) and MCZ84 (red, $n = 154$) cells expressing FtsZ-mEos2 or FtsZ84-mEos2, respectively, plotted against and binned by corresponding ring diameter. Bin edges: 0, 200, 300, 400, 500, 600 nm. Z-ring intensity measurements in (d) and (e) are overlaid with best-fit (solid), $\alpha = 1$ (dashed gray), and $\alpha = 2$ (dotted gray) models generated from time-lapse parameters of corresponding strain (Table 2.2).

Time-lapse analyses revealed that FtsZ84-GFP took significantly longer to stabilize at midcell in MCZ84 than wt FtsZ-GFP in MC4100 (66 ± 5 min, $n = 77$ vs. 51 ± 3 min, $n = 78$ for wt, $p = 0.01$, Table 2.2). However, the average septum closure rates measured in MCZ84 and MC4100 strains were not significantly different from each other (18.0 ± 0.7 nm/min, $n = 77$ for MCZ84 and 19.3 ± 0.7 nm/min, $n = 78$ for MC4100, respectively, $p = 0.34$). In addition, in both strains the time-dependent septum closure rates accelerate during the constriction period, although to different degrees ($\alpha = 1.4 \pm 0.2$ vs. 1.9 ± 0.3 for MCZ84 and MC4100, respectively, Figure 2.9d-e, Table

2.2). These results suggest that the GTPase activity of FtsZ influences Z-ring assembly and density, but does not alter the rate of septum closure during cell constriction.

***minC* and *matP* deletions alter Z-ring density and dynamics similarly, but septum closure rate oppositely**

Next, the Z-ring was perturbed by removing either MinC, a negative regulator of FtsZ polymerization, or MatP, a positive Z-ring assembly regulator. In *E. coli*, MinC oscillates between the cell poles to prevent aberrant, polar Z-ring formation (Raskin and de Boer 1999; Hu and Lutkenhaus 2000; Shiomi and Margolin 2007; Dajkovic, Lan et al. 2008; Shen and Lutkenhaus 2010). MatP is a DNA-binding protein involved in proper chromosome segregation (Mercier, Petit et al. 2008; Espeli, Borne et al. 2012; Stouf, Meile et al. 2013). MatP stabilizes Z-ring positioning at midcell through its interaction with the Z-ring associated proteins, ZapA and ZapB (Buss, Coltharp et al. 2013; Buss, Coltharp et al. 2015). The higher tendency of FtsZ to polymerize at places other than midcell in the absence of MinC or MatP should thus alter Z-ring density and the timescale of Z-ring assembly or disassembly, allowing assessment of the influence of these properties on the rate of septum closure.

Z-ring structures and dynamics were examined in a BW25113 Δ *minC* or BW25113 Δ *matP* strain using the FtsZ-mEos2 or FtsZ-GFP fusions. As expected, PALM images of FtsZ-mEos2 in BW25113 Δ *minC* cells (Figure 2.10a) often showed non-midcell FtsZ clusters, consistent with the role of MinC in preventing polar Z-ring formation (Guberman, Fay et al. 2008). The Z-ring also took longer to stabilize at midcell (108 ± 7 min, $n = 45$ vs. 91 ± 5 min, $n = 98$ for wt BW25113, $p = 0.01$). Interestingly, the effects of *matP* deletion on Z-ring morphology (Figure 2.10b) and assembly time (114 ± 10 min, $n = 37$, $p = 0.01$) were similar to those of *minC* deletion.

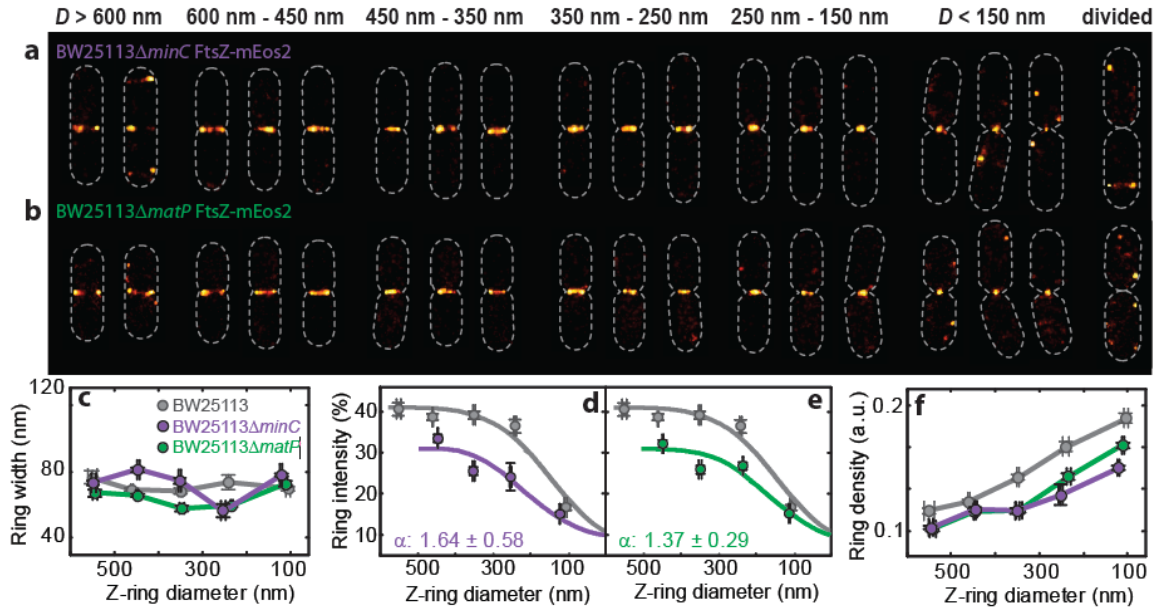


Figure 2.10 Analysis of Z-ring dimension, density, and time-dependent septum closure rate for $\Delta minC$ and $\Delta matP$ cells.

(a-b) Superresolution PALM images of live BW25113 $\Delta minC$ (a) and BW25113 $\Delta matP$ (b) cells expressing FtsZ-mEos2, grouped by measured Z-ring diameter. Cell outlines approximated by dashed lines. (c-f) Ring width (c), intensity (d-e), and density (f) in BW25113 $\Delta minC$ (purple, $n = 73$) and BW25113 $\Delta matP$ (green, $n = 68$) cells expressing FtsZ-mEos2 plotted against and binned by corresponding ring diameter. Bin edges: 0, 200, 300, 400, 500 nm. Z-ring intensity measurements in (d) and (e) are overlaid with best-fit (solid line) models generated from time-lapse parameters of corresponding strain (Table 2.2). Results for wt BW25113 (gray) are replicated from Figure 3 for comparison.

Further quantification revealed that the Z-ring began to disassemble at larger diameters in the absence of either MinC or MatP than in the wt BW25113 parental strain (Figure 2.10d-e), and that the relative Z-ring density remained 20 - 40% lower in either mutant than that in wt cells (Figure 2.10f). However, the Z-ring width remained unchanged (Figure 2.10c). Surprisingly, despite exhibiting similar effects on Z-ring structure and assembly dynamics, the two mutants exhibited different effects on septum closure rate: BW25113 $\Delta minC$ cells exhibited significantly slower rates ($v_c = 10.2 \pm 0.6$ nm/min, $n = 45$, $p = 0.004$) compared to wt BW25113 ($v_c = 12.5 \pm 0.4$ nm/min, $n = 98$), while BW25113 $\Delta matP$ cells exhibited significantly higher rates ($v_c = 14.2 \pm 0.9$ nm/min, $n = 37$, $p = 0.02$). The fact that similar decreases to Z-ring density and increases in

assembly time caused by deletion of *matP* or *minC* result in opposite changes to the rate of septum closure suggests that these Z-ring properties may not be limiting factors in driving septum closure.

Septum closure rate is coupled to cell elongation rate

The characterizations above have revealed that altered Z-ring structures, densities, and dynamics during the cell cycle do not result in systematic changes to septum closure rates. This lack of a unifying, FtsZ-centric theme prompted exploration of whether the other two divisome components may play more dominant roles in driving septum closure. To examine the relationship between septum closure and PG synthesis, the function carried out by the second group of divisome proteins (see 'Chapter 1:

Introduction to Bacterial Cytokinesis'), individual cell septum closure rates (v_c) were compared to cell elongation rates (v_e), calculated as cell length added per unit time. Under balanced growth, cell elongation is rate-limited by cell wall PG synthesis (Lee, Tropini et al. 2014; Rojas, Theriot et al. 2014), and thus cell elongation in rod-shaped *E. coli* directly reflects PG synthesis activity. As the topography of PG synthesis activity switches from lateral to septal localization at constriction onset (Wientjes and Nanninga 1989), elongation rates were calculated both prior to (v_{el}) and during (v_{ec}) constriction, reflecting the rate of lateral and septal PG synthesis, respectively.

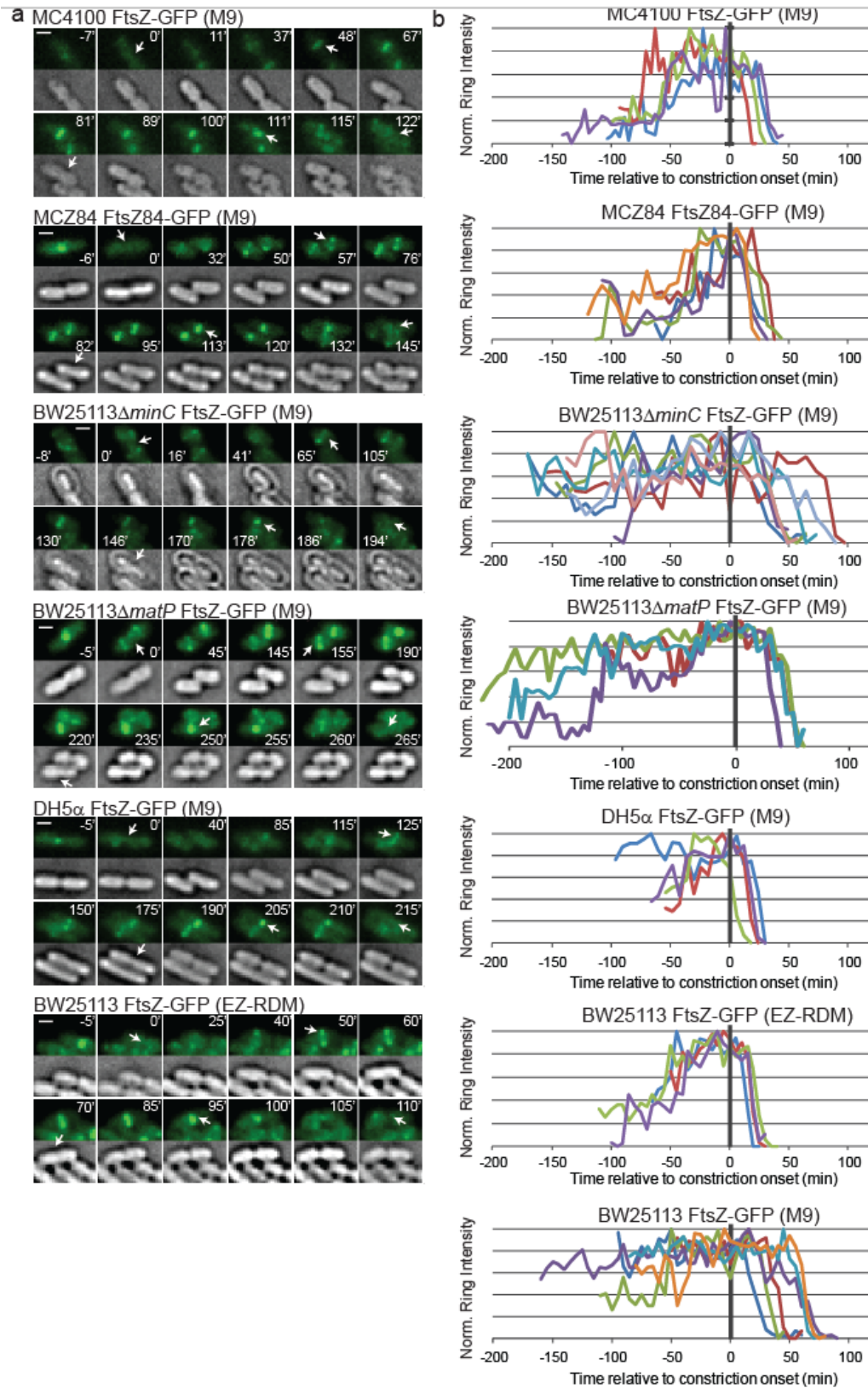
Single cell elongation rates were measured for the two wt strains tested (BW25113 and MC4100) and two additional conditions: wt DH5 α grown in M9 at RT ($\tau = 181 \pm 8$ min, $n = 40$) and the same BW25113 strain growing faster in rich defined medium (EZ-RDM) at RT ($\tau = 94 \pm 2$

min, $n = 80$). Time-lapse analyses and live-cell PALM imaging of the two additional strains showed similar Z-ring assembly dynamics (Table 2.2), two-phase Z-ring contraction (Figure 2.11), and continuous increase of Z-ring density throughout contraction (Figure 2.12). The two strains exhibited different average septum closure rates ($v_c = 17.0 \pm 1.2$ nm/min and 25.5 ± 1.0 nm/min for DH5 α and BW25113 (EZ-RDM), respectively), but similar rate accelerations ($\alpha = 1.40 \pm 0.44$ and 1.28 ± 0.30 , respectively).

Figure 2.11 Time-lapse analysis of FtsZ-GFP in other wt and mutant strains (see next page).

(a) Representative time-lapse fluorescence (top) and bright-field (bottom) montages of wt and mutant *E. coli* expressing FtsZ-GFP. Strain names are indicated above each montage. Arrows indicate cell cycle landmarks for a single cell, sequentially: cell birth; ring stabilization; onset of visible constriction; beginning of Z-ring disassembly; completion of cell division. Time-stamps displayed as minutes relative to cell birth. (b) Representative time-dependent Z-ring fluorescence (percentage of fluorescence in the ring relative to that of the whole cell) traces for wt and mutant strains. Z-ring intensity was calculated as in Figure 2, but then normalized such that the values varied

from 0 to 1 to allow easier comparison of different cells. Each color represents a different cell. All time-lapse traces are temporally aligned such that the time of constriction onset coincides with $t = 0$. In all strains, time traces exhibiting a delay between constriction onset ($t = 0$) and Z-ring disassembly (decay in normalized ring intensity) can be observed. Scale bars, $1 \mu\text{m}$.



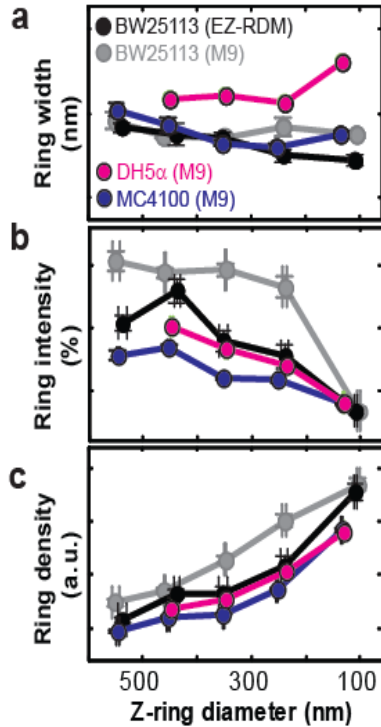


Figure 2.12 Analysis of Z-ring dimension and density for all wt strains and conditions.

Ring width (a), intensity (b), and density (c) plotted against and binned by corresponding ring diameter for live BW25113 (gray, $n = 66$), DH5 α (magenta, $n = 65$), and MC4100 (blue, $n = 83$) cells grown in M9 media, and BW25113 cells grown in EZ-RDM media (black, $n = 36$), all expressing FtsZ-mEos2. The BW25113 (M9) dataset (gray) replicates those in Figures 3 and 5 for comparison. Bin edges: 0, 200, 300, 400, 500, 600 nm. The first bin (500 - 600 nm) was not used for DH5 α due to its smaller starting diameter.

Comparison of septum closure rates and elongation rates for all four wt conditions revealed that the average rate of septum closure scales with both v_{el} and v_{ec} for all wt strains and conditions studied (Figure 2.13a-b, $r = 0.98$ and 0.99 , $p = 0.02$ and 0.01 , respectively). These correlations suggest that the different septum closure rates observed can indeed be attributed to differences in PG synthesis rates under different growth conditions, and that the chemical processes limiting the rate of cell wall PG synthesis before and during cell constriction may also limit the rate of septum closure.

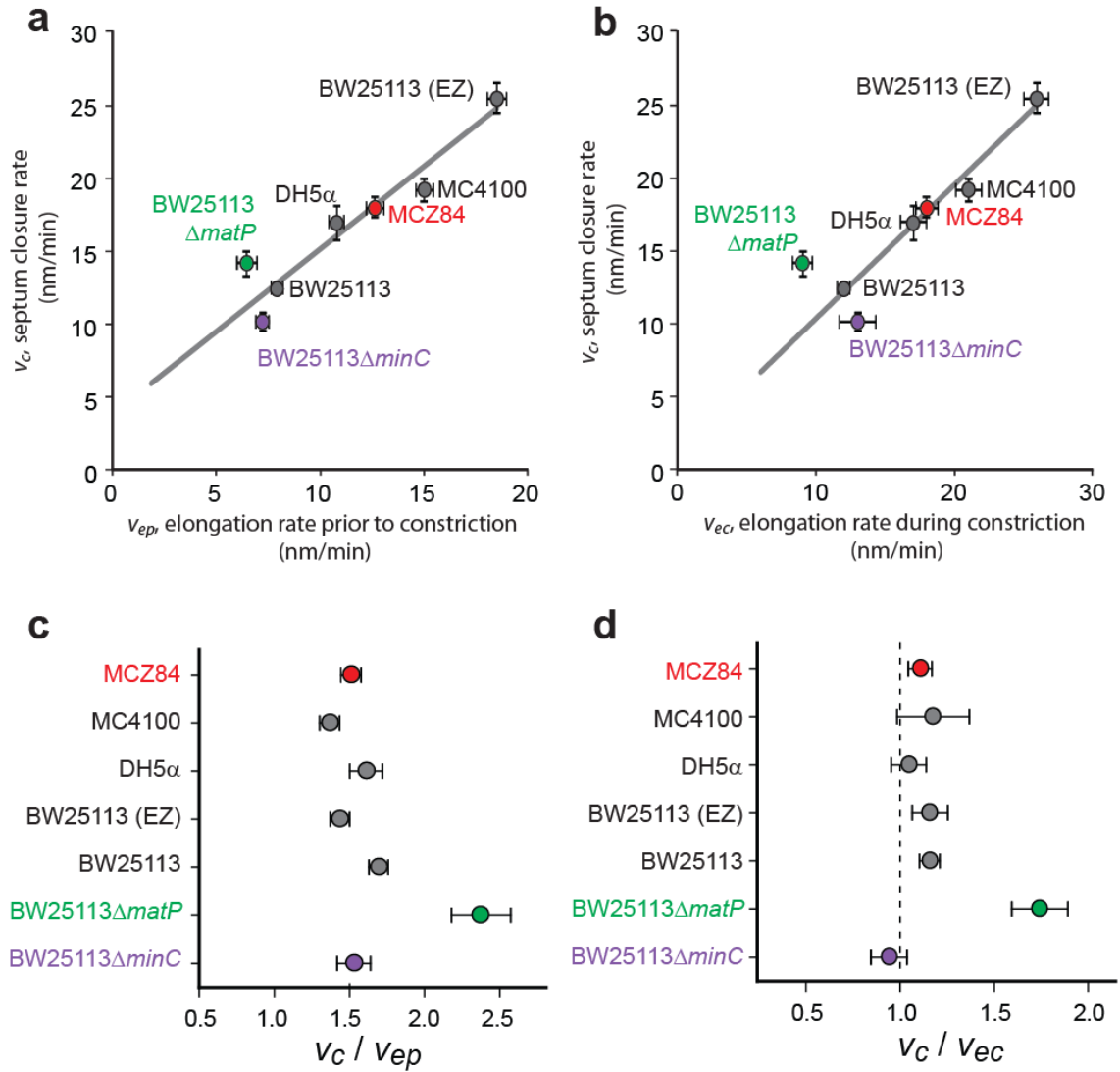


Figure 2.13 Comparison of septum closure and cell elongation rates.

(a-b) Average septum closure rate ($\langle v_c \rangle$) plotted against cell elongation rate prior to ($\langle v_{ep} \rangle$, a) or during ($\langle v_{ec} \rangle$, b) constriction for all wt (gray) and mutant (colored) *E. coli* strains. Color code corresponds to those in (c) and (d). Linear trend lines were fit using only wt strains. (c-d) Average ratio of septum closure rate relative to cell elongation rate prior to ($\langle v_c / v_{ep} \rangle$, a) or during ($\langle v_c / v_{ec} \rangle$, b) constriction for all wt (gray) and mutant (colored) *E. coli* strains. Dotted line illustrate $\langle v_c / v_{ec} \rangle = 1$ ratio.

Interestingly, the average ratio of v_c/v_{ec} , which compares the total diameter of the septum closed during constriction with the cell length added during that time, is close to unity for the four wt strains and conditions (Figure 2.13d). This unity ratio can be explained by the growth of hemispherical poles in *E. coli*, in which the starting septum diameter is equivalent to the final combined length of the poles. Thus, our measurements indicate that cell elongation occurs predominately through septal synthesis during constriction, as substantial contributions from lateral cell growth would result in $v_c/v_{ec} < 1$. This finding is consistent with previous measurements of PG synthesis activity, which was shown to switch from lateral to septal localization at constriction onset (Wientjes and Nanninga 1989).

Absence of MatP modulates the coupling between cell wall elongation and septum closure rate

Applying the same comparison of cell elongation and septum closure rates to the three mutant strains (Figure 2.13c-d, Table 2.2), revealed that the relative ratios $\langle v_c/v_{el} \rangle$ and $\langle v_c/v_{ec} \rangle$ of MCZ84 and $\Delta minC$ cells were similar to those of their respective wt parent (< 20 % difference, **Table 2.2**), but that those of $\Delta matP$ cells were substantially larger than all the other strains, with $\langle v_c/v_{el} \rangle = 2.18 \pm 0.17$ (vs. 1.69 ± 0.06 for wt BW25113 in M9, $p = 2.5e-4$) and $\langle v_c/v_{ec} \rangle = 1.75 \pm 0.15$ (vs. 1.16 ± 0.05 for wt BW25113 in M9, $p < 5e-5$), respectively (Figure 2.13b-d, Table 2.3). Thus, the septum closure rate observed in $\Delta matP$ cells is significantly faster than expected given its elongation rate and PG synthesis activity. Given that deletion of *matP* leads to defects in chromosome segregation (Espeli, Borne et al. 2012), deviation of the two ratios from all other

strains suggests that chromosome segregation can likely modulate the coupling between septal PG synthesis and septum closure during constriction.

Discussion

Z-ring Organization

This work has illustrated the 3D structural organization and remodeling of the contracting Z-ring with unprecedented resolution. The *E. coli* Z-ring was demonstrated to be composed of discontinuous, heterogeneously distributed FtsZ clusters loosely confined in a toroidal zone of ~ 100 nm in width and ~ 65 nm in thickness. Similar Z-ring heterogeneity has also been observed previously (Leisch, Verheul et al. ; Li, Trimble et al. 2007; Fu, Huang et al. 2010; Strauss, Liew et al. 2012; Buss, Coltharp et al. 2013; Holden, Pengo et al. 2014; Rowlett and Margolin 2014). The mean thickness of the toroidal zone FtsZ clusters occupy (~ 65 nm) is significantly larger than that of a single layer of FtsZ protofilaments, which would appear < 30 nm under the iPALM resolution. A multi-layered Z-ring, as suggested by the thickness measurement, is consistent with previous predictions (Fu, Huang et al. 2010; Carmon, Fishov et al. 2012). Although the resolution achieved here did not allow direct observation of the number or orientation of FtsZ protofilaments within the heterogeneous Z-ring, the small cluster size observed (30 - 50 nm, Figure 2.5) supports heterogeneity in FtsZ protofilament orientation, as the membrane curvature preference of short, ~ 50 nm protofilaments was estimated to be only ~ 0.1 kT (Sun and Jiang 2011).

While this large body of studies using different methodology in different organisms supports a punctate, clustered organization of the Z-ring, *in vitro*, membrane-attached FtsZ can form long, continuous protofilaments that wrap around liposomes (Milam, Osawa et al. 2012; Szwedziak,

Wang et al. 2014), and a recent ECT study observed long, single-layered protofilaments at cell division sites (Szwedziak, Wang et al. 2014). These studies support a smooth, continuous Z-ring organization. However, a continuous ring is not required for Z-ring function, as incomplete Z-rings can lead to cell wall indentation (Addinall and Lutkenhaus 1996). Both organizations are possible *in vivo* and likely reflect two dynamic states of the Z-ring modulated by the GTPase activity of FtsZ. It is known that GTP hydrolysis promotes the fracture of long FtsZ polymers (Mateos-Gil, Paez et al. 2012) and that subunit turnover dynamics are reduced in FtsZ GTPase mutants (Stricker, Maddox et al. 2002). Thus, active GTP hydrolysis may result in constant structural remodeling, and consequently a discontinuous, clustered Z-ring organization. This may explain why long FtsZ protofilaments were predominately observed with an overexpressed FtsZ GTPase mutant (D212A) background (Szwedziak, Wang et al. 2014). A discontinuous, dynamic structure may allow the Z-ring to reorganize promptly in response to cellular cues such as the SOS stress response (Dajkovic, Mukherjee et al. 2008; Chen, Milam et al. 2012) or changes in nutrient availability (Weart, Lee et al. 2007; Hill, Buske et al. 2013).

If Z-ring discontinuity is indeed important for Z-ring function, then the multi-layer configuration observed here can be viewed as a buffering system against fluctuations in FtsZ levels. Because the percentage of cellular FtsZ localized to the Z-ring is known to remain at $\sim 30\%$ in *E. coli*, even when FtsZ is over-expressed 8-fold (Fu, Huang et al. 2010), any increase in cellular FtsZ levels should cause a corresponding increase in FtsZ levels within the Z-ring. If FtsZ filaments could only form a single layer, an 8-fold increase in FtsZ levels would in turn lead to an 8-fold increase in the membrane-exposed Z-ring surface area, greatly reducing its discontinuity. Thus, by accommodating multiple layers, FtsZ clusters can maintain their discontinuity under increased FtsZ levels, which can occur when checkpoints related to nutrient availability or DNA

damage temporarily postpone cell division (Hill, Buske et al. 2013; Jonas 2014). The existence of a buffering system for increased FtsZ levels is supported by the higher tolerance of *E. coli* for FtsZ overexpression (viable at levels up to 8-fold (Fu, Huang et al. 2010)) compared to FtsZ depletion (not viable below $\sim 50\%$ FtsZ levels (Palacios, Vicente et al. 1996)).

Constriction Initiation

During the cell cycles of all wt and mutant *E. coli* strains, the first detectable cell wall indentation precedes the initiation of Z-ring Disassembly (Table 2.2). This finding suggests that disassembly of the Z-ring does not serve as a trigger to initiate cell wall constriction. An alternative triggering mechanism is suggested by the fact that the relative time spent in the Z-ring Maturation phase, prior to constriction, is very tightly-distributed ($\sim 30\%$ of the cell cycle, CV = 0.03) compared to the other phases (CV > 0.1, Table 2.2). This tight distribution suggests that the Z-ring maturation process is closely coupled to the cell growth rate. It is possible that this conserved Z-ring Maturation time represents a preparation phase prior to the onset of visible constriction.

What might this preparation phase entail? Previous studies indicate that some periplasmic components of the *E. coli* divisome (FtsI, FtsN, FtsQ, and FtsW) arrive at the Z-ring after a substantial delay, on the order of tens of minutes, or $\sim 20\%$ of the cell cycle time (Aarsman, Piette et al. 2005). This delay is longer than that expected for the kinetics of protein interactions, so it is unclear why the recruitment of these 'late' divisome proteins is delayed (Aarsman, Piette et al. 2005). One possibility is that the recruitment of these periplasmic proteins, some of which bind peptidoglycan, is facilitated by a particular peptidoglycan composition. The finding that FtsZ can direct peptidoglycan synthesis in the absence of these 'late' division proteins (de Pedro, Quintela et al. 1997; Varma, de Pedro et al. 2007; Potluri, de Pedro et al. 2012) suggests that

some alterations to midcell peptidoglycan may occur during this Z-ring Maturation phase to promote the recruitment of late division proteins. The involvement of peptidoglycan synthesis would explain the minutes-scale delay and our observed tight coupling of Z-ring Maturation time to growth rate, given that cell wall synthesis is limiting for cell growth (Rojas, Theriot et al. 2014). Thus, constriction initiation in *E. coli* may be modulated by division site preparation by FtsZ and early divisome constituents, followed by recruitment of late division proteins. The transient arrival of late divisome proteins may then positively reinforce their own recruitment by additional modification of the cell wall until visible constriction finally ensues (Gerding, Liu et al. 2009). This coupling between cell wall growth and constriction initiation is an attractive mechanism to ensure that the cell is properly doubled before dividing (Campos, Surovtsev et al. ; Weart, Lee et al. 2007).

Z-ring function during constriction

As a large body of work has already demonstrated, the Z-ring is the essential scaffold to recruit all other division proteins to initiate constriction (Adams and Errington 2009). The force-generating function and mechanisms of the Z-ring, however, have been highly debated (Erickson 2009). This work attempted to determine how the Z-ring generates constrictive force, if it does indeed drive septum closure, by observing the consequences of a perturbed Z-ring on septum closure rates. However, the observed effects consistently supported a contrary model in which the Z-ring does not drive septum closure.

First, the driving force generation mechanism cannot be limited by FtsZs GTPase activity, because the *ftsZ84* mutant showed essentially the same septum closure rate as its wt parent strain. Second, the mechanism cannot be dependent on Z-ring disassembly because cell wall

constriction initiated significantly earlier than Z-ring disassembly under all conditions (Table 2.2) and because the diameter at which individual Z-rings started to disassemble varied widely (from 600 nm to 250 nm) among different conditions (Figure 2.8d-e, Figure 2.9d-e, Figure 2.10b, and Figure 2.12b). Third, the driving mechanism cannot be dependent on Z-ring density (FtsZ concentration in the ring), because increased density in the *ftsZ84* mutant strain did not alter septum closure rate, while reduced density in the $\Delta minC$ and $\Delta matP$ strains led to opposite changes in septum closure rate. Fourth, the driving mechanism cannot be dependent on FtsZ's assembly dynamics during the cell cycle, as the three mutations (*ftsZ84*, $\Delta minC$, $\Delta matP$) all resulted in delayed Z-ring stabilization at midcell, but did not lead to systematic changes in the septum closure rate. These results indicate that the chemical process responsible for septum closure is most likely not driven by a process that is governed by FtsZ activity or concentration at the midcell.

The role of FtsZ's GTPase activity

If the GTPase activity of FtsZ is not a major driver of cell constriction, then what is its role? GTPase activity has been clearly implicated in modulating FtsZ dynamics within the Z-ring (Anderson, Gueiros-Filho et al. 2004). These dynamics may influence the force-generation ability of the Z-ring (Allard and Cytrynbaum 2009), but may also influence its ability to transduce any force generated by other cellular processes. Previous studies have shown that the same amount of force applied at different frequencies can generate different cellular outcomes, suggesting that turnover dynamics within a force-transducing structure could act as a band-pass filter (Hoffman, Grashoff et al. 2011). In the case of divisome dynamics, this band-pass feature could mean that only forces applied (from cell wall modification) at a proper frequency can be transduced efficiently by the Z-ring, or *vice versa*. Thus, the GTPase activity of FtsZ, and divisome

dynamics in general, may be an important regulatory system to help coordinate force generation across the cell envelope. This is supported by the similarity in turnover dynamics (10 - 30 s) between FtsZ and the other divisome proteins investigated so far (ZapA, ZapB, FtsA, ZipA, EzcA, PBP2) (Mosyak, Zhang et al. 2000; Anderson, Gueiros-Filho et al. 2004; Geissler, Shiomi et al. 2007; Buss, Coltharp et al. 2015).

The concept of harmonized dynamics between cytoplasmic and periplasmic divisome constituents is also related to the properties of a visco-elastic material, which behaves as a solid on timescales faster than its turnover dynamics, but as a fluid on longer time-scales that allow molecule turnover. This visco-elastic nature would allow the Z-ring to gradually adapt to the geometry of the invaginating septum on the minutes scale, while still maintaining a stiffness on short timescales to transduce or generate force. The observation that the Z-ring does not show appreciable disassembly in the MCZ84 mutant strain until much smaller ring diameters than the corresponding wt strain (Figure 2.9d vs. e) supports a role for FtsZ's GTPase activity in the gradual Z-ring remodeling required to accommodate the contracting ring diameter.

Factors driving cell constriction

While Z-ring perturbations showed no clear influence on septum closure rates, a strong correlation was observed between septum closure rate and cell elongation rate (Figure 2.13a-b). In particular, the rate of cell length elongation during constriction is identical to the rate of septum closure for wt cells (Figure 2.13d), suggesting that PG synthesis limits the rate of septum closure during constriction. This interpretation is also supported by early observations of prolonged constriction periods caused by mutations to FtsI or FtsQ (Taschner, Huls et al. 1988; Huls, Vischer et al. 1999; Aarsman, Piette et al. 2005), or by overexpression of FtsN (Aarsman,

Piette et al. 2005); these three proteins are all essential components of the divisome that are involved in new septum PG synthesis (Egan and Vollmer 2013). Consistent with this notion, analysis of the time-dependent change in septum closure rate was consistent with slowing septal surface area addition, but accelerating septum closure rate ($\alpha < 2$) in most cases (Table 2.2).

This study also shed light on another important factor that can modulate the rate of septum closure. The $\Delta matP$ strain modulated the coupling between septum closure rate and cell elongation rate during constriction as measured by the ratio of septum closure to cell elongation rate (Figure 2.13c-d). This effect is likely not caused by changes to Z-ring architecture because the same structural alterations were seen in the $\Delta minC$ strain, which did not show significant deviations from wt strains (Figure 2.13c-d). Because MatP is involved in nucleoid segregation (Espeli, Borne et al. 2012), and also has a role in stabilizing the Z-ring through its interaction with ZapB (Buss, Coltharp et al. 2015), this result likely suggests that the progress of cell envelope constriction and septum closure is coordinated with the progress of chromosome segregation so that the septum does not close over unsegregated chromosomes (Buss, Coltharp et al. 2015). This coordination is most likely mediated through DNA-binding divisome components (FtsK and MatP in *E. coli* (Mercier, Petit et al. 2008; Deghorain, Pagès et al. 2011; Espeli, Borne et al. 2012)), which have synergistic effects (Stouf, Meile et al. 2013).

It remains possible that the Z-ring does indeed generate a constrictive force during cell division, but that this force is not rate-limiting. The observed increase in Z-ring density during septum closure (Figure 2.8b) supports the existence of Z-ring condensation proposed to generate constrictive force (Ghosh and Sain 2008; Surovtsev, Morgan et al. 2008; Lan, Daniels et al. 2009;

Szwedziak, Wang et al. 2014). It is also possible, however, that the observed condensation is a natural consequence of lagging Z-ring remodeling in response to the gradually reducing septum diameter during cell wall constriction.

If the Z-ring does generate a small, non-rate-limiting force during constriction, it may serve primarily to direct the spatial and temporal activity of divisome constituents rather than to directly constrict the cell envelope. A recent computational modeling study has shown that a substantial force (> 400 pN) would be needed to constrict a static *E. coli* cell wall, but that the existence of cell wall turnover and remodeling can reduce the required force to as little as ~ 8 pN (Lan, Wolgemuth et al. 2007). This small contribution relative to that of cell wall remodeling is consistent with our finding that cell wall synthesis has a larger influence on the rate of septum closure than does Z-ring structure and function. This reasoning is further supported by the fact that the estimated magnitude of deformation force generated by FtsZ filaments reconstituted on liposomes is only on the order of 20 - 90 pN (Paez, Mateos-Gil et al. 2009; Horger, Campelo et al. 2010).

Summary

To summarize, these findings support a model in which the roles of cell wall synthesis and chromosome segregation dominate that of the Z-ring in defining the rate of septum closure. These results challenge the FtsZ-centric view of constrictive force generation in bacteria, and suggest that FtsZ should be viewed as a key regulator and mediator rather than major force generator.

Materials and Methods

Bacterial strains and plasmid construction.

All strains and plasmids used in this study are listed in

Table 2.4.

Plasmid pTH025 that expresses *ftsZ84-mEos2* was generated circuitously from pCH027 (Buss, Coltharp et al. 2013) as follows. The *tagRFP-T* gene was amplified from pCP-TagRFP-T (gift of Roger Tsien) by PCR using PfuTurbo (Agilent) with primers
ATTAGAGCTCGATGCGGGAGGCCTTGGTGGTGCAATGGTGTCTAAGGGCGAAGAG and
AATTGCGGCCGCTTACTTGTACAGCTCGTCCATGCCA, restricted with SacI and NotI (New England Biolabs), then ligated into pCH027 restricted likewise to generate pCH033 expressing *ftsZ-tagRFP-T*. The *ftsZ84* mutation (g310a -> G105S) was constructed in pCH033 using the QuikChange protocol (Agilent) for site-directed mutagenesis with primers
TGCTGCGGGTATGAGTGGTGGTACCGG and CCGGTACCACCACTCATAACCCGAGCA to generate pTH024 expressing *ftsZ84-tagRFP-T*. Subsequently, a portion of the *ftsZ* gene containing the *ftsZ84* mutation was restricted from pTH024 with XhoI and SacII (New England Biolabs) and ligated into pJB042 restricted likewise to generate pTH025.

The *ftsZ84* mutation (g310a -> G105S) was constructed in plasmid pXY021 from JW0093 (Kitagawa, Ara et al. 2005) using the QuickChange protocol (Agilent) for site-directed mutagenesis with primers TGCTGCGGGTATGAGTGGTGGTACCGG and
CCGGTACCACCACTCATAACCCGAGCA.

Table 2.4 Strains and plasmids used in this study

Strain	Genotype	Reference/source
BW25113	<i>F⁻ Δ(araD-araB)567 ΔlacZ4787(::rrnB-3) rph-1 Δ(rhaD-rhaB)568 hsdR514</i>	(Datsenko and Wanner 2000) CGSC #7636
JW1165	BW25113 <i>ΔminC::kan</i>	(Baba, Ara et al. 2006) CGSC #9075
JW0939	BW25113 <i>ΔmatP::kan</i>	(Baba, Ara et al. 2006) CGSC #12061
DH5α	<i>F⁻ Δ(argF-lac)169 φ80dlacZ58(M15) ΔphoA8 glnV44(AS) deoR481 rfbC1 gyrA96 recA1 endA1 thiE1 hsdR17</i>	Life Technologies
JOE309	MC4100 <i>ara+</i> (MC4100: <i>F⁻ araD139 Δ(argF-lac)169 flhD5301 fruA25 relA1 rpsL150(strR) rbsR22 Δ(fimB-fimE)632(::IS1) deoC1</i>)	(Chen and Beckwith 2001) Gift of Jon Beckwith
MCZ84	MC4100 <i>ftsZ84(Ts) leu-260::Tn10</i>	(Dai, Xu et al. 1993) CGSC #8259
Plasmid	Relevant genotype	Reference/source
pJB042	ColEI, <i>P_{T5-lac}::ftsZ-mEos2 cat</i>	(Buss, Coltharp et al. 2013)
pJB051	ColEI, <i>P_{T5-lac}::mEos2-zapA cat</i>	(Buss, Coltharp et al. 2015)
pTH025	ColEI, <i>P_{T5-lac}::ftsZ84-mEos2 cat</i>	This study
JW0093	ColEI, <i>P_{T5-lac}::6xHis-ftsZ-gfp cat</i>	(Kitagawa, Ara et al. 2005)
pXY021	ColEI, <i>P_{T5-lac}::6xHis-ftsZ84-gfp cat</i>	This study

Growth conditions and sample preparation

For imaging studies, cell cultures grown as described previously (Buss, Coltharp et al. 2015).

Briefly, saturated LB cultures were diluted by at least 1:100 in either M9+ (M9 supplemented

with MEM vitamins, MEM amino acids, and 0.4% glucose) or EZ-RDM media (Teknova) supplemented with 0.4% glucose and grown at room temperature (RT) until they reached OD_{600} between 0.2 and 0.5. Antibiotics were added when appropriate: 150 $\mu\text{g ml}^{-1}$ chloramphenicol and/or 50 $\mu\text{g ml}^{-1}$ kanamycin. For iPALM and live PALM imaging, expression of FtsZ-mEos2 (pJB042), FtsZ84-mEos2 (pTH025), and mEos2-ZapA (pJB051) were induced with 20 μM IPTG for two hours. Cells were then washed and allowed to grow for 1.5 - 2 hours or 3 hours at RT without inducer before collection for imaging (live PALM) or fixation (iPALM), respectively. FtsZ-GFP and FtsZ84-GFP were imaged using basal expression from JW0093 or pXY021, respectively. The level of FtsZ-mEos2 expression achieved with the 3 hour growth without inducer for iPALM was assessed previously to be $\sim 25\%$ of total FtsZ (Buss, Coltharp et al. 2015). The levels of FtsZ-mEos2 and FtsZ84-mEos2 achieved using the 1.5 - 2 hour growth without inducer for live PALM were assessed by quantitative immunoblotting as described previously (Buss, Coltharp et al. 2013) to be $\sim 70\%$ of total FtsZ in all strains (Figure 2.14). Levels of FtsZ-GFP and FtsZ84-GFP achieved by basal expression were similar to or lower than that of FtsZ-mEos2 and FtsZ84-mEos2 used for live PALM in all strains (Figure 2.14).

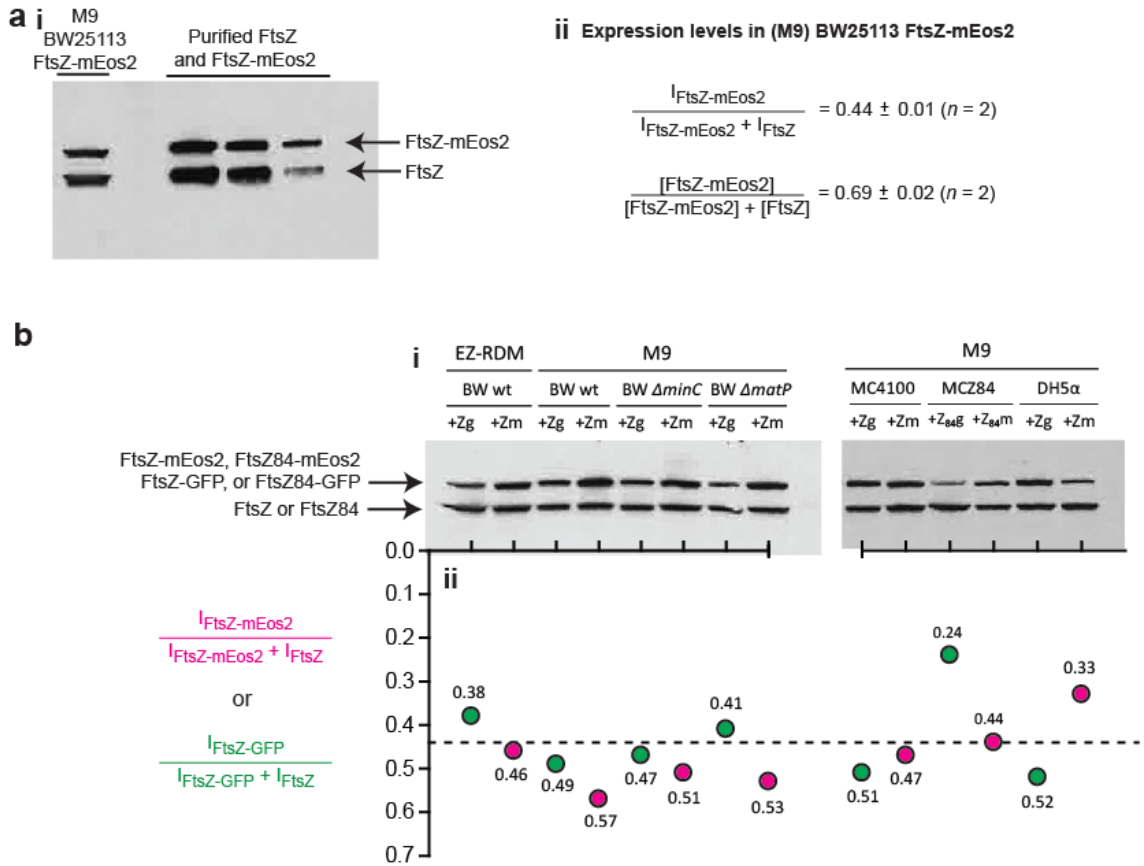


Figure 2.14 Immunoblot analysis of FtsZ, FtsZ-mEos2, and FtsZ-GFP expression levels.

(a) (i) Representative immunoblot of BW25113 cells expressing FtsZ-mEos2 in M9 prepared in the same manner used for live cell PALM imaging: 2 hour induction with 20 μ M IPTG followed by 2 hour growth without inducer (left lane). The right three lanes contain purified FtsZ and FtsZ-mEos2 as standards to quantify the relative amounts of FtsZ and FtsZ-mEos2 in the left lane. (ii) The relative band intensity of FtsZ-mEos2 compared to the total intensity of FtsZ-mEos2 and FtsZ in the BW25113 cells (top, ratio = 0.44 ± 0.01 , $n = 2$) corresponds to a relative concentration of FtsZ-mEos2 relative to total FtsZ-mEos2 and FtsZ concentration of 0.69 ± 0.02 (bottom, $n = 2$). (b) (i) Immunoblots of all strains and conditions used in this study. Abbreviations: BW, BW25113; Zg, FtsZ-GFP; Zm, FtsZ-mEos2. (ii) Relative band intensities for all strains and conditions used in this study are similar to that measured for BW25113 grown in M9 (a) with the exception of FtsZ84-GFP expression in MCZ84, which may be lower.

Fixation was performed using 4% (v/v) paraformaldehyde in PBS (pH 7.4) for 45 min at RT.

Immuno-fluorescence samples were prepared as described previously (Buss, Coltharp et al.

2013) using 1:100 and 1:150 dilutions of rabbit α -FtsZ (a gift from H. Erickson) and mouse α -GFP

(Life Technologies, A-11120), respectively. Secondary antibodies, Alexa Fluor[®] 568 goat α -rabbit

IgG (Life Technologies, A-11011) and Alexa Fluor® 488 goat α -mouse IgG (Life Technologies, A-11001) were subsequently applied at 1:140 and 1:200 dilutions, respectively.

Fluorescence imaging

iPALM data collection was performed as previously described (Buss, Coltharp et al. 2015).

Several datasets used in this study overlap with those used to examine different phenomena in a previous study (Buss, Coltharp et al. 2015). Molecule localizations from iPALM data were identified using PeakSelector v9.3 software (Shtengel, Galbraith et al. 2009). Live PALM and immuno-superresolution image acquisition and molecule localization were performed using custom MATLAB routines as described previously (Buss, Coltharp et al. 2013; Buss, Coltharp et al. 2013; Buss, Coltharp et al. 2015). Prior to live PALM imaging, a green fluorescence and brightfield snapshot of each cell was acquired for determination of cell morphology and Z-ring intensity. The resolution achieved for iPALM and PALM data was measured from the displacements of nearest neighbors in adjacent frames (Endesfelder, Malkusch et al. 2014) (Figure 2.2) and are listed in Table 2.1. Simultaneous two-color acquisition of immuno-superresolution data was achieved using an OptoSplit II (Cairn Research) device and overlaid using registration transformations obtained from images of multi-emission TetraSpeck beads (Life Technologies, T-7279) as described previously (Buss, Coltharp et al. 2015). The image registration error was 4.6 nm. All iPALM and live PALM images were visualized using the ViSP representation software (Beheiry and Dahan 2013) where each molecule was colored according to the local molecule density (neighbors within 30 nm). Immuno-fluorescence images were visualized using custom MATLAB (MathWorks) routines (Buss, Coltharp et al. 2013; Buss, Coltharp et al. 2015) and ImageJ (Schneider, Rasband et al. 2012). Time-lapse imaging of FtsZ-

GFP was performed at 4- to 8-minute time intervals as described previously (Buss, Coltharp et al. 2015).

FtsZ cluster simulation

Simulations of FtsZ clusters were generated by Monte Carlo methods with the following parameters. Z-rings were represented as one-dimensional (1D) structures in which all FtsZ molecules are projected onto the circumferential dimension of the ring. Each simulation condition was defined by three parameters: cluster density (ρ_c , number of clusters per μm), cluster length (l_c , FWHM of a cluster in which molecules are normally distributed about its center), and $f_{clustered}$ (the fraction of Z-ring molecules localized to clusters; the non-clustered molecules are assumed to be uniformly distributed around the ring). A fourth parameter, FtsZ molecule density (ρ_m , molecules per μm), was applied in the same manner for all simulation conditions. For each set of three simulation parameters, 500 Z-rings were simulated as follows:

1. Initialize Z-ring circumference, $circum = 3.14 \mu\text{m}$.
2. Sample molecule density ρ_m with replacement from the distribution of experimental measurements for the strain of interest (BW25113 or DH5 α).
3. Sample the number of clusters in this ring, n_c , from a Poisson distribution with mean, $\rho_c * circum * \rho_m / \langle \rho_m \rangle$. Simulations with higher values of ρ_m will have more clusters such that the average number of molecules in clusters remains similar across different rings in this simulation.
4. For each of n_c clusters:
 - Sample its center position (p_{center}) from a uniform random distribution between 0 and $circum$.
 - Sample its FWHM, $size_{FWHM}$, from an exponential distribution with mean, l_c . This exponential distribution of cluster sizes and molecules (next line) resembles a random aggregation model.

- Sample the number of molecules in this cluster, $n_{m-clust}$ from an exponential distribution with mean, $f_{clustered} * \rho_m / \rho_c$
 - For each of $n_{m-clust}$ molecules:
 - Sample its center position from a normal distribution with mean, p_{center} , and $\sigma = size_{FWHM} / 2.35$. This results in clusters with Gaussian shapes as observed in iPALM images. These cluster sizes thus include size amplification caused by finite localization precision, and the dimensions of the underlying structure is $\sqrt{size_{FWHM}^2 - resolution_{FWHM}^2}$.
5. Sample the number of non-clustered molecules in this ring n_{m-non} , from a Poisson distribution with mean, $\rho_m * circum * (1 - f_{clustered})$
 6. For each of n_{m-non} molecules:
 - Sample its center position from a uniform random distribution between 0 and $circum$.

The result of each simulation is a set of molecule coordinates for 500 simulated rings. The properties of these simulated coordinates and those of the experimental datasets were assessed as follows:

1. Crop each simulated or experimental ring to the central 600 nm to avoid edge effects.
2. Calculate the normalized molecule density histogram along the ring circumference: fraction of molecules residing in each 10 nm stretch of Z-ring circumference.
3. From this histogram, calculate (i) the spatial autocorrelation (acf) of molecule density along the circumference and (ii) the probability distribution of normalized molecule density (see Figure 2.5).
4. For each simulated or experimental condition, calculate the average of both curves calculated in 3.

Each simulation condition (set of parameters for ρ_c , l_c , and $f_{clustered}$) was compared to an experimental condition by assessing the sum of the squares of the residuals (SSRs) for both the acf (Figure 2.5a) and molecule density histogram (Figure 2.5b). Each SSR value was normalized by the median SSR value for that curve in all simulations. Then, the normalized SSR values for

the acf and density histogram of each simulation were combined as the root mean squared sum to generate SSR_{combined} . This combined value thus represents the collective deviation of each simulation from the experimental result. The distribution of simulation parameters resulting the lowest SSR_{combined} values are shown in Figure 2.5c.

Additional image processing, data analysis, and simulation

For iPALM images, Z-ring width was measured from the x-y projection as the full width at half maximum (FWHM) of molecule density. The molecule positions were then projected onto the cell's cross-section (x-z plane) and fit with a circle, whose diameter represents that of the Z-ring. Lastly, the apparent Z-ring thickness was measured as the FWHM of molecule density projected along the circumference of the fitted circle. See Figure 2.15a for an example. Note that the apparent ring width and thickness measured using the toroidal zone are generally larger than those of individual FtsZ clusters as some clusters are not perfectly aligned with each other.

Measurements of Z-ring width and diameter from live PALM images was performed using custom MATLAB software as described previously (Buss, Coltharp et al. 2015) and illustrated in Figure 2.15b. Because the spatial resolution of the optical setup used to perform the live PALM experiments improved during the course of this work, resulting in systematic changes to the apparent ring width values, Table 2.1 also lists 'deconvolved widths' for comparison. The deconvolved width was calculated by assuming that the measured ring FWHM is the root-mean-square sum of the deconvolved width and the spatial resolution, as would be expected if the underlying Z-ring profile is Gaussian (Coltharp, Yang et al. 2014).

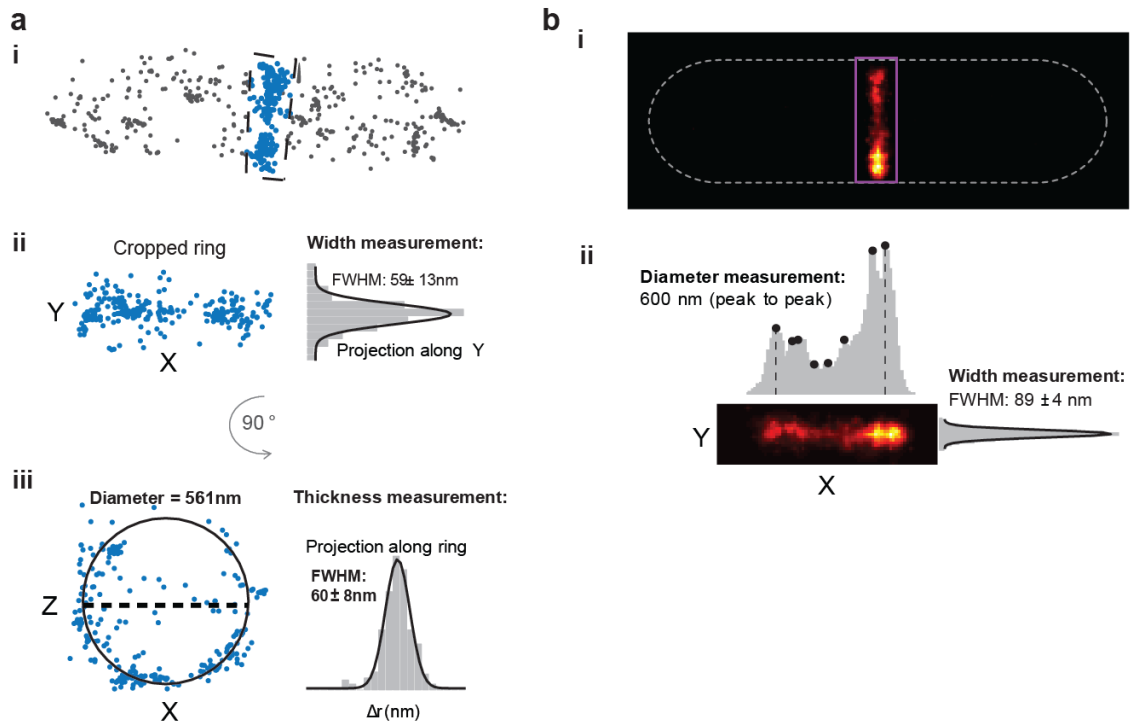


Figure 2.15 Dimension measurements from superresolution data.

(a) (i) For iPALM data, coordinates of molecules within the ring (blue) were cropped out to measure the ring dimensions. (ii) Ring width was measured by projecting all coordinates within the ring onto the Y axis (longitudinal cell axis), then fitting the molecule density histogram (gray bars) with a Gaussian distribution (black line) to obtain the FWHM dimension. (iii) Ring diameter (dashed black line) was measured by fitting a circle (left, solid black line) to the XZ projection of molecule coordinates (blue). This fitting worked well even if only a portion of the circle is sampled (as in TIRF imaging). Ring thickness was measured by generating a histogram of the distance of each coordinate within the ring from the fitted circumference (Δr , gray bars). The FWHM of a Gaussian (solid black line, right) fitted to this distribution was defined as the ring thickness. (b) (i) From live PALM images, ring dimensions was calculated from cropped ring images (magenta box). (ii) Ring diameter was determined as the distance between the two distal peaks (dashed lines) in the projected ring intensity along the X axis (cell width). Ring width was measured as the FWHM of a Gaussian (solid black line) fit to the ring intensity projected along the Y axis (longitudinal cell axis).

Measurements of the percent of FtsZ-mEos2 or FtsZ-GFP fluorescence localized to midcell relative to that in the whole cell were made from the green fluorescence image acquired prior to live PALM imaging with user-defined regions defining the ring and cell outlines. This value is 30 - 40 % prior to the start of cell division, irrespective of the fluorescent protein fusion, and

unaffected by overexpression of up to 8-fold the endogenous level of FtsZ (Anderson, Gueiros-Filho et al. 2004; Geissler, Shiomi et al. 2007; Fu, Huang et al. 2010). As the endogenous FtsZ concentration remains constant throughout the *E. coli* cell cycle (Rueda, Vicente et al. 2003; Weart and Levin 2003), this relative fluorescence measurement should reflect FtsZ quantities in the Z-ring proportionately throughout the entire contraction process, and allows direct comparison of cells with varying expression levels. Because growth in EZ-RDM resulted in higher cellular autofluorescence background than growth in M9, midcell percentage of FtsZ-mEos2 in BW25113 cells was calculated using a corrected total cell intensity calculated by subtracting the average total intensity of BW25113 cells not expressing fluorescent protein fusions from the measured total cell intensity.

Time-lapse montages were generated in ImageJ (Schneider, Rasband et al. 2012) using the StackReg plugin (Thevenaz, Ruttimann et al. 1998) to spatially align adjacent frames. The length of each Z-ring period was determined from time-lapse fluorescence and brightfield images of cells expression FtsZ-GFP. The end of a mother cell cycle (and thus daughter cell birth) was identified as the frame at which FtsZ-GFP fluorescence disappears completely (Figure 2.7) (Buss, Coltharp et al. 2015). Z-ring stabilization was defined as the frame after which the fluorescent Z-ring no longer sampled non-midcell regions. The first frame of visible constriction was determined from brightfield images. The beginning of Z-ring disassembly was defined as the last frame before continuous decrease in Z-ring fluorescence intensity at the end of the cell cycle. To avoid extensive signal overlap from adjacent cells, only cells located at the micro-colony periphery were analyzed. In mutant strains, only cells exhibiting normal, midcell division were analyzed.

Conversion of time-lapse traces of the percentage of FtsZ at midcell vs. time into traces of the percentage of FtsZ at midcell vs. septum diameter was achieved by simulation. For each strain, 2000 traces were generated by sampling with replacement from the duration distributions of Contraction Phase I and Contraction Phase II. Each time trace was generated by assuming that the percentage of FtsZ at midcell, p , remained constant at p_0 for the duration of Contraction Phase I, then decreased linearly to p_f during Contraction Phase II to generate p vs. t traces that are smoothed mimics of the time-lapse trajectories (Figure 2.7b and Figure 2.11b). The values of p_0 and p_f were taken from the starting and ending y-values of the p vs. D plots (e.g. Figure 2.8f). The time values of the simulated traces were then converted to diameter, $D(t)$, values according to Equation 1 to generate p vs. D traces using varying values of α . The τ_c value for each trace is the sum of the durations of its sampled Contraction Phase I and II periods. The D_0 value for each trace was taken as the average D_0 value for each strain.

Statistics

All reported errors are standard errors of the mean. All reported correlation values are Pearson's r . Two-tailed p -values for comparison of structural dimensions and time-lapse period durations were calculated using Student's t . Two-tailed p -values for comparison of septum closure rates (v_c) and rate ratios ($\langle v_c/v_{ep} \rangle$ and $\langle v_c/v_{ec} \rangle$) were calculated using randomization tests with 20,000 iterations.

Part II:

Quantitative Superresolution Fluorescence Microscopy

Chapter 3 :

Overview of Superresolution Fluorescence Microscopy

Adapted with permission from:

Coltharp, C., Xiao, J. Superresolution microscopy for microbiology. **Cellular Microbiology**
(2012).

and

Coltharp, C. Yang, X., Xiao, J. Quantitative analysis of single-molecule superresolution
images. **Current Opinion in Structural Biology** (2014).

Introduction

Light microscopy is a powerful and widely-used research tool in biology that has profoundly increased our understanding of cell biology. It employs visible light to resolve small cellular objects and dynamic processes in biological samples. The biological questions that can be investigated with light microscopy are limited by the imaging resolution, which defines the minimum distance between two distinguishable features. For conventional optical microscopes, the resolution is bounded by the diffraction of light, which causes the signal from a point source to spread as it travels to the detector. The shape of the resulting signal is termed the 'point spread function (PSF)' and can be well-approximated by a Gaussian distribution. The FWHM of this Gaussian determines the 'diffraction limit' of resolution, which is approximately half the wavelength of detected light (>250nm for most biocompatible fluorophores) (Rayleigh 1896; Katsu, Tsuchiya et al. 1984).

Electron microscopes (EM) can achieve superior resolution because the wavelength of an electron is subnanometer. However, it is difficult to specifically label proteins to allow their unambiguous identification under EM. Additionally, fixation or vitrification of samples, which is required for EM, is not compatible for live cell imaging.

Recently, a variety of superresolution fluorescence microscopy techniques have been developed to take advantage of the specific labeling and live-cell compatibility afforded by fluorescent light microscopy, while achieving resolutions (10-50 nm) approaching that of electron microscopy.

These techniques can be divided into three categories: first, methods based on single-molecule localization such as photoactivated localization microscopy (PALM) (Betzig, Patterson et al. 2006) and stochastic optical reconstruction microscopy (STORM) (Rust, Bates et al. 2006; Bates,

Huang et al. 2007); second, derivations of structured illumination microscopy (SIM) (Heintzmann and Cremer 1999; Frohn, Knapp et al. 2000; Sharonov and Hochstrasser 2006; Folling, Bossi et al. 2008); and third, point-scanning methods such as stimulated emission-depletion (STED) microscopy (Burnette, Sengupta et al. 2011; Bakshi, Siryaporn et al. 2012).

Single Molecule Localization Methods

Photoactivatable and photoswitchable fluorophores are the key to implementing localization-based superresolution techniques. These fluorophores can transition stochastically between bright and dark emission states by exposure to specific wavelengths of light. During superresolution imaging, activation light is kept at a low level such that within a diffraction-limited area only a single fluorophore is fluorescing at a time (Figure 3.1A). The positions of these single molecules are then localized with nanometer accuracy by fitting their intensity profiles with a Gaussian function that approximates the microscope's PSF. Positions collected from thousands of frames are then overlaid to reconstruct a superresolution image. During this acquisition time, fiducial beads are often added to the sample to track and calibrate stage drift.

This principle was first demonstrated in 2006 using photoactivatable fluorescent proteins (PALM)(Betzig, Patterson et al. 2006) and cyanine dye pairs (STORM) (Rust, Bates et al. 2006), and resolutions of 10nm and 20nm were achieved, respectively. Later, this principle was extended to conventional organic dyes, which have been shown to photoswitch robustly under proper buffer conditions (Fleming, Shin et al. 2010; Fu, Huang et al. 2010; Plass, Milles et al. 2011). The general principle of isolating single fluorophores can be further extended to nonphoton-driven switching. For example, PAINT (Point Accumulation for Imaging in Nanoscale

Topography) utilizes fluorophores that can only be detected when their fluorescence is enhanced ~ 1000 fold by binding reversibly to a lipid membrane (Zhu, Zhang et al. 2012).

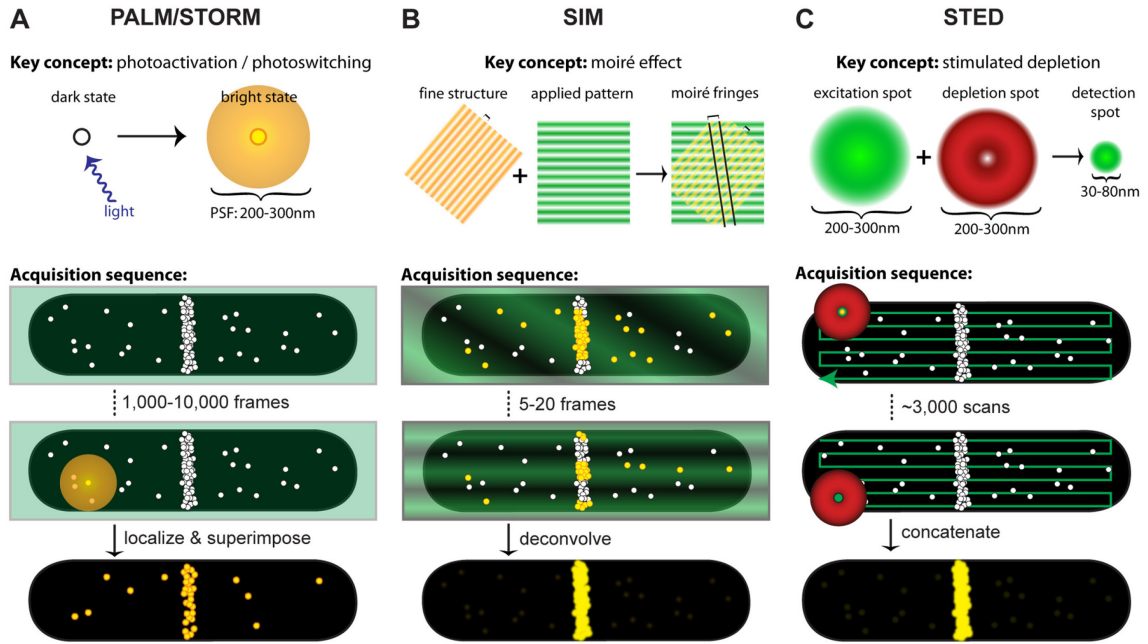


Figure 3.1 Key concepts and acquisition schematics for each superresolution technique.

In each schematic, molecule positions are shown as white circles, excitation light is represented in green, depletion light is represented in red, and fluorescing molecules are highlighted in yellow. In acquisition schematics, molecule positions mimic cellular distributions of the FtsZ protein, which is the only bacterial protein to be analyzed by all three methods. (A) Single-molecule localization-based techniques such as PALM and STORM apply low levels of activation light (violet arrow) so that single molecules are stochastically activated and localized. An activated molecule produces a diffraction-limited spot (diffuse yellow circle), which is fit with a Gaussian function to localize the molecule's position with nanometer precision. After hundreds to thousands of molecules have been localized, their positions are superimposed to create the superresolution image (bottom). (B) SIM utilizes the moiré effect, which results when an illumination pattern (green stripes) is applied to a specimen with fine structures that are smaller than the diffraction limit (e.g. closely-spaced yellow stripes or molecule positions). Interference between the illumination pattern and the sample produces moiré fringes (two are shown as diagonal black lines) that are spaced further apart than the underlying sample spacing, thus visualizing sub-diffraction-limited features. Several illumination patterns are applied to the sample, then spatial information extracted from the Fourier transforms of each image is combined to generate the superresolution image (bottom). Although the emission from fluorescing molecules (yellow circles) is diffraction-limited, the diffraction-limited profiles are omitted for clarity. (C) For STED imaging, concentric excitation and depletion beams (green circle and red donut, respectively) are projected onto a sample. Although fluorophores are excited throughout the diffraction-limited excitation spot (large green circle), the depletion beam (red donut) stimulates molecules outside the central 30-80nm region back to the ground state before they fluoresce, generating a superresolution PSF (small green circle). These beams are scanned across the specimen to collect the superresolution image (bottom).

Structured Illumination Microscopy (SIM)

SIM achieves superresolution by extracting fine structural details from the interference of a structure with predetermined illumination patterns. When a sinusoidal illumination pattern (Figure 3.1B, green shading) is applied to a fluorescent sample, an interference pattern results. The diffraction-limited fringes of this interference pattern, called moiré fringes, contain information about the underlying structural pattern of the sample that cannot be observed with conventional light microscopy. By applying a set of illumination patterns of different spacing and rotation angles to the same sample (Figure 3.1B), sub-diffraction-limited structural information of the sample can be extracted from Fourier transforms of the resulting interference patterns. (Lukosz 1963; Heintzmann and Cremer 1999; Frohn, Knapp et al. 2000; Gustafsson 2000). Standard implementations of SIM achieve two-fold improvement in lateral resolution (Frohn, Knapp et al. 2000; Sharonov and Hochstrasser 2006), but finer resolution can be achieved by taking advantage of nonlinear fluorescence responses (Shroff, Galbraith et al. 2007; Folling, Bossi et al. 2008). Thus far, applications of SIM in bacterial cells have employed the two-fold improvement afforded by commercial systems: Applied Precision DeltaVision OMX (Westphal, Rizzoli et al. 2008; Lieberman, Frost et al. 2012) and Nikon N-SIM (Kner, Chhun et al. 2009). The main advantage of SIM is that superresolution can be achieved with any conventional fluorescent protein because the resolution enhancement comes solely from the patterned illumination and image processing.

Stimulated Emission Depletion Microscopy (STED)

STED microscopy was the earliest far-field superresolution technique developed (Burnette, Sengupta et al. 2011; Bakshi, Siryaporn et al. 2012). The instrumentation is similar to a confocal

microscope with the addition of a depletion laser, which stimulates excited molecules back to the ground state in a donut-shaped region around the central confocal spot (Figure 3.1C). In this way, only molecules within 30 - 80 nm of the center of the excitation spot are detected. This depletion concept was extended to fluorophore photoswitching by using the donut-shaped depletion beam to switch fluorophores into the off state instead of stimulating emission (Grotjohann, Testa et al. 2011). This process, termed Reversible Saturable Optical Fluorescence Transitions (RESOLFT), mitigates the detrimental effect that the high power depletion beam may have on cell viability because the RESOLFT depletion beam is used at much lower power (~ 1 kW/cm²) than the stimulated depletion laser (100 - 500 MW/cm²) (Grotjohann, Testa et al. 2011).

Practical Considerations for Microbiology

Time Resolution

Because each superresolution image is the combined result of multiple frames or scans, the acquisition time for a complete superresolution image relative to the timescale of dynamics associated with a protein of interest is important for live cell imaging. In this regard, bacterial cells are ideal specimens for superresolution imaging because of their small sizes, which allow very small scanning or illumination areas to increase imaging speed and probe the real-time dynamics of bacterial proteins and cellular structures in live cells.

SIM has the fastest time resolution of the three categories described in this review. Each 2D SIM image requires only 5-20 frames for reconstruction, so one superresolution image can be generated in a few seconds, and imaging rates of up to 11Hz (one complete SIM image in 90ms) have been achieved for fields of view sufficient for bacterial samples (13 μ m x 13 μ m)(Kner,

Chhun et al. 2009). STED and RESOLFT microscopy have slower time resolutions than SIM due to the requirement for point-scanning. However, the small size of bacterial cells makes this much less of an issue, so STED images can be collected in several seconds, and a $1.8 \times 2.5 \mu\text{m}^2$ area has been imaged at up to 28 Hz (one complete STED image in 36ms) (Ando, Mizuno et al. 2004).

Single molecule localization-based methods have the slowest time resolution because thousands of frames are required to sufficiently sample a structure of interest. The Nyquist sampling criterion states that a desired resolution of X nm will be achieved if the sampling frequency is at least $X/2$ nm (Shannon 1949; Biteen and Moerner 2010; Coltharp, Yang et al. 2014). For example, to achieve a resolution of 30 nm, a structure should be labeled with one molecule every $15 \times 15 \text{ nm}^2$. Because of this criterion, compact structures are ideal candidates for live-cell superresolution imaging as they require fewer localizations for sufficiently sampling (e.g. a $45 \times 45 \text{ nm}^2$ structure requires 9 molecules and a $450 \times 450 \text{ nm}^2$ structure requires 900 molecules to achieve 30 nm resolution). Consequently, tight clusters and cytoskeletal elements can be sufficiently sampled in under a minute (Gustafsson 2005; Hein, Willig et al. 2008).

Imaging Duration

Another component of live-cell imaging is the number of time-lapse superresolution images that can be acquired. For SIM and STED imaging, the number of superresolution images that can be acquired is usually limited by fluorophore photobleaching. This can be very problematic for bacterial structures, which are often made up of only a few hundred of molecules. This limitation can be overcome by ectopically overexpressing the proteins of interest, but as described below, protein overexpression may limit the biological conclusions that can be drawn. For STED, it was reported that up to 30 superresolution images can be acquired without

significant photobleaching in live mammalian cells using the fluorescent protein citrine (Hein, Willig et al. 2008). However, this extended imaging time remains to be demonstrated in bacterial cells where protein expression levels are generally lower.

When imaging live cells by single-molecule localization-based techniques, the number of superresolution images that can be acquired is also limited by the protein expression level because each image needs to have sufficient sampling of the visualized structure. An additional constraint for these techniques is the cell viability under continuous laser exposure throughout the imaging sequence. Although the intensity of 405 nm light typically used to induce photoactivation and photoswitching is relatively low ($1 - 5 \text{ kW/cm}^2$) (Liu, Xing et al. 2014), prolonged exposure can result in reactive oxygen species that cause DNA damage. Since the transcriptional response to DNA damage begins at approximately 20 min after exposure to UV light in *E. coli* (Klein, Proppert et al. 2014), the duration of live-cell PALM imaging is typically kept to less than 15 minutes (Friedman, Vardi et al. 2005; Gustafsson 2005; Hein, Willig et al. 2008; Heilemann, van de Linde et al. 2009; Holden, Uphoff et al. 2011).

Probe Selection

The three methods described here have different fluorophore requirements, and the properties of these probes have been reviewed elsewhere (Fernandez-Suarez and Ting 2008; Kopek, Shtengel et al. 2012). Below is a brief account of the types of probes suitable for the three imaging categories with emphasis on specific probe selection considerations associated with bacterial cells.

Among the three methods described here, SIM has the most lax probe requirements, allowing any combination of excitation and emission wavelengths that can be accommodated by a

widefield fluorescence microscope. As mentioned above, photostability is crucial for time-lapse and 3D SIM imaging, and consequently most studies utilize bright organic dyes and, more recently, EGFP. STED requires dyes that can be specifically excited and depleted by spectrally-separated lasers (e.g. Alexa647N or citrine) and RESOLFT requires fluorophores that can be photoswitched thousands of times (e.g. rsEGFP). For single-molecule based localization methods, photoactivatable and photoswitchable proteins such as Dendra, Dronpa, mEos2, and PAmCherry are common genetic labels for PALM, while (d)STORM utilizes organic dyes such as the Cy3-Cy5 pair or Alexa647, which have been extensively characterized to determine optimal buffer conditions (Strahl and Hamoen 2010).

Improving the stability or photoswitching kinetics of superresolution fluorophore can vastly improve data throughput and quality. For example, because the precision of single-molecule localization is determined by the number of photons collected (Thompson, Larson et al. 2002), the frame rate of PALM/STORM measurements is limited by the exposure time required to collect sufficient photons from a single molecule. In addition, the prevalence of photoblinking among most fluorophores, which can cause false measurements of molecule density, must be taken into consideration or accounted for by the superresolution image reconstruction algorithm (Annibale, Vanni et al. 2011; Annibale, Vanni et al. 2011). Hence, the ideal fluorescent protein for PALM would have a high quantum yield during a single fluorescence burst, and photobleach very quickly so that new molecules can be activated at a faster rate.

Most superresolution studies in bacteria have used genetically-encoded fluorescent proteins. Although organic dyes often have superior photophysical properties, it is very difficult to achieve high efficiency labeling of intracellular proteins due to low cell wall permeability. Thus, most

dye-labeling schemes require cell wall permeabilization via lysozyme and detergent treatment, and are only compatible with fixed cells. Schoen *et al.* demonstrated this method using PicoGreen, which becomes 1000-fold brighter upon binding DNA (Shannon 1949).

Functionality of Labeled Protein

Fusing a fluorescent protein to a protein of interest may affect its function and localization pattern, especially if the fluorescent protein has a tendency to oligomerize (Zhang, Chang *et al.* 2012). To test for functionality, the fusion protein should be expressed and examined for full recovery of physiological activity in a null mutant of the native protein (Friedman, Vardi *et al.* 2005; Dempsey, Vaughan *et al.* 2011; Patterson 2011). If full activity recovery cannot be achieved, the fusion protein can be expressed ectopically so that it decorates the endogenous structure as long as the subcellular localization of the fusion protein is identical to that of unlabeled protein (Gustafsson 2005; Hein, Willig *et al.* 2008; Westphal, Rizzoli *et al.* 2008; Dempsey, Vaughan *et al.* 2011). Because each fluorescent protein may have a different interaction with a given protein or its cellular surroundings, probe selection may require testing several different fluorescent proteins (Dempsey, Vaughan *et al.* 2011) or linkers (Sengupta, Jovanovic-Talisman *et al.* 2011).

Expression Level

In general, superresolution techniques are more successful for proteins with naturally high expression levels. For both STED and SIM, higher expression levels provide higher contrast and allow acquisition of more image stacks for 3D or time-lapse imaging. For PALM and STORM, expression levels determine the degree of sampling within a structure and thus directly influence the effective imaging resolution. Overexpression of a protein of interest can enhance

image quality, but can also result in aberrant structures or measurements because most biological systems are fine-tuned to operate within a given concentration range. Whenever possible, superresolution studies should be conducted at physiological expression levels (Gustafsson 2005; Greenfield, McEvoy et al. 2009; Patterson 2011), and careful controls should be performed if overexpression is required.

Fixation

Although live cells provide the most physiological conditions for imaging, fixation is often necessary for some samples and measurements. For structures that move on the time-scale of imaging, fixation may be the only way to 'freeze' the movement and capture true structural dimensions without motion-induced blur. Fixation may also be required to localize fast-moving cytoplasmic proteins, which are usually undetectable in live PALM experiments. Furthermore, the most suitable way to measure molecule density is from fixed cells where molecule movement cannot obstruct counting measurements.

As with high-resolution EM samples, caution must be taken to avoid fixation-induced distortions to cellular structures, especially for membrane-associated proteins. Although formaldehyde and glutaraldehyde are common fixatives for EM, formaldehyde is most common for fluorescence imaging because glutaraldehyde often generates a high autofluorescence background (Fischer, Jacobson et al. 2008). Because fixation is reversible, fixed samples should be stored at 4°C and imaged as soon as possible (Fischer, Jacobson et al. 2008). If the imaged structures do not move on the timescale of imaging, comparison of fixed and live samples can provide assurance that fixation has not introduced noticeable aberrations (Lee *et al.*, 2011, Fu *et al.*, 2010).

Sample Immobilization

Preparation of bacterial samples is similar among all superresolution techniques, which have utilized two main methods of cell immobilization: adherence via Poly-L-Lysine (PLL) and compression via agarose gel pad. PLL adherence is very convenient, but has been shown to affect the proton-motive force (McKinney, Murphy et al. 2009; Fu, Huang et al. 2010) and protein localization (Fu, Huang et al. 2010; Buss, Coltharp et al. 2013) in *E. coli*. As a result, most live-cell studies immobilize cells with 1.5%-3% agarose gel pads (Gustafsson 2005; Biteen, Thompson et al. 2008; Hein, Willig et al. 2008; Westphal, Rizzoli et al. 2008; Kner, Chhun et al. 2009; Holden, Uphoff et al. 2011; Sengupta, Jovanovic-Talisman et al. 2011; Wheeler, Mesnage et al. 2011; Biteen, Goley et al. 2012; Szwedziak, Wang et al. 2012). Detailed instructions regarding sample preparation, imaging, and data analysis for PALM studies in bacterial cells have been described for *C. crescentus* (Greenfield, McEvoy et al. 2009) and *E. coli* (Colville, Tompkins et al. 2009).

Hardware and Software Complexity

Although the localization-based methods were the latest to be developed, their incorporation into microbiological study has far outpaced the other two methods as evidence by the number of studies reviewed here. This is most likely because of the minimal hardware modifications and expertise required to implement a PALM or STORM system. Construction of a STED microscope requires considerable investment and expertise, but the availability of commercial systems for both SIM (Applied Precision DeltaVision OMX and Nikon N-SIM) and STED (Leica TCS STED) make these methods viable options for shared facilities.

Image processing is conversely much simpler for STED than for localization methods or SIM.

Because the superresolution information of STED is encoded in the scanning beams, almost no

image processing is required and superresolution images can be observed in real time. SIM images can only be viewed after deconvolving the high resolution information from each set of fringes, and PALM/STORM experiments require detection and localization of hundreds to thousands of spots per bacterial cell. Improvement of the analysis algorithms for both SIM and PALM/STORM is ongoing, with several new publications per year. For PALM and STORM, improvements have focused on accurate localization of overlapping emitters (Holden, Uphoff et al. 2011; Zhu, Zhang et al. 2012) to improve imaging speed and correcting for overcounting artifacts caused by photoblinking (Annibale, Vanni et al. 2011; Sengupta, Jovanovic-Talisman et al. 2011; Veatch, Machta et al. 2012).

Quantitative Analyses

The single-molecule methods, PALM and STORM, are unique because they provide lists of molecule coordinates in addition to intensity-based superresolution images. Proper analysis of the molecule coordinates enables quantitative characterization of the density, size, composition, and spatial distributions of cellular structures at near-molecular precision. Such quantitative information is difficult to obtain by other imaging techniques.

Image-based Analyses

Rendering PALM and STORM images. The output data of single-molecule localization algorithms contain molecule coordinates and their associated localization precisions, which are used to render a superresolution image. An intuitive method to represent this data is by superimposing unit Gaussian distributions centered on each molecule's coordinates. These Gaussian distributions are analogous to the PSFs that cause the familiar blur in conventional images (Figure 3.2Ai), but with standard deviations specified by each molecule's estimated localization

precision (Figure 3.2Aii). Because the localization precision represents the uncertainty of each molecule's position, the intensities in this accumulated image represent relative probabilities that the detected molecules are located in each pixel but not the absolute number of molecules.

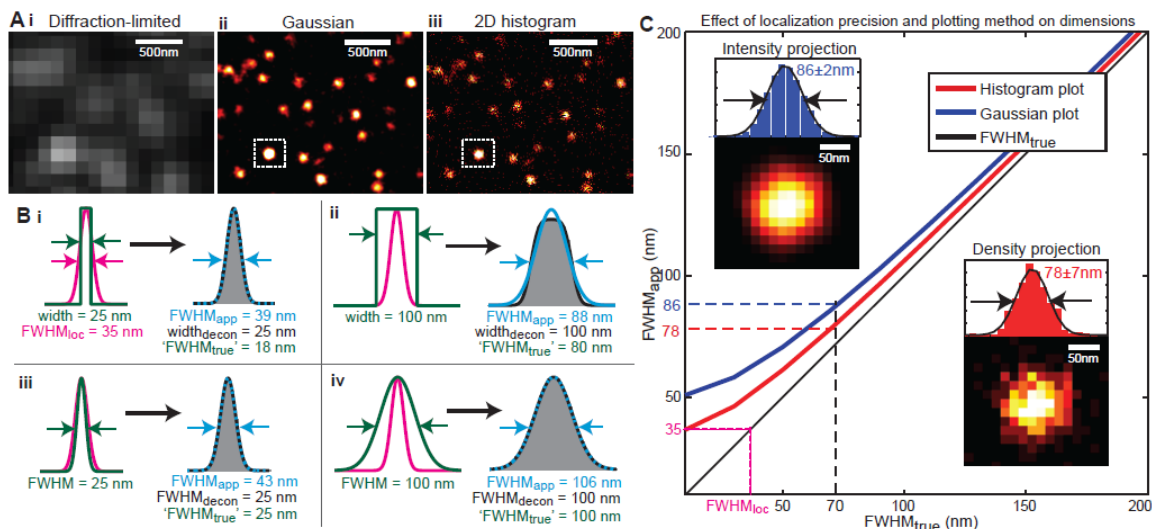


Figure 3.2 Super-resolution image generation and dimension measurement.

(A) Simulated clusters (70 nm FWHM) displayed as a diffraction-limited image (i), superresolution Gaussian plot (ii), and superresolution 2D histogram (iii). Sigma for each Gaussian spot in (ii) is specified as 15 nm localization precision. (B) Underlying structural cross section profiles (green) are convolved with Gaussian-distributed localization precision (magenta) to generate apparent profiles in superresolution images (gray). Fitting the apparent profile with a Gaussian distribution (cyan) yields the apparent width, $FWHM_{app}$. The true FWHM can be inferred using the relationship

$$FWHM_{true} = \sqrt{FWHM_{app}^2 - FWHM_{loc}^2}$$

which is only valid for inherently Gaussian-distributed structures (iii and iv), and yields erroneous measurements for other structures (i and ii). Prior knowledge of the underlying structures can yield the correct width via deconvolution ($width_{decon}$ and $FWHM_{decon}$). (C) Cluster FWHM measured from the 2D histogram (red) and Gaussian plot (blue) plotted against true FWHM. Insets: representative measurements of 70 nm clusters (white dotted outlines in A). Y-intercepts represent smallest measurable FWHM by each method, which is determined by localization precision (magenta).

An alternative representation that allows comparison of molecule counts is a two-dimensional histogram of number of molecules per pixel (Figure 3.2Aiii). Molecules can only be confidently assigned to a particular pixel in this histogram if the pixel size is larger than the typical localization precision. Quantifying the absolute number of molecules in a structure from this

histogram requires correction for over- and under-counting artifacts (see 'Counting Molecule Numbers' below). However, these artifacts apply universally to the entire image, so relative molecule counts within different regions and features can still be measured directly from a sufficiently-sampled histogram without further correction (Coltharp, Kessler et al. 2012).

Measuring structural dimensions. The dimension of a cellular structure is commonly measured from its cross-sectional projection (Bates, Huang et al. 2007; Fu, Huang et al. 2010; Wang, Quan et al. 2012). With sufficient sampling frequency, this apparent cross-section is the result of the convolution of the true structural profile and the Gaussian distribution defined by localization precision (Figure 3.2B) (Bates, Huang et al. 2007). Prior knowledge of structural shape can thus be used to deconvolve the true structural dimension from the apparent cross-section profile (see examples in **Error! Reference source not found.**Bi and ii). In the absence of prior structural knowledge, the underlying structure can be approximated by a Gaussian-distribution (Figure 3.2Biii and iv), in which case the measured apparent full-width at half-maximum ($FWHM_{app}$) is related to the true dimension ($FWHM_{true}$) and the localization precision ($FWHM_{loc} = 2.35\sigma_{loc}$) by $FWHM_{app} = \sqrt{FWHM_{loc}^2 + FWHM_{true}^2}$. Generally, dimensions of previously-uncharacterized structures are reported as fitted $FWHM_{app}$ because it allows convenient comparison of different structures observed with similar localization precision without imposing an assumption of structural shape (Fu, Huang et al. 2010; Buss, Coltharp et al. 2013). As illustrated in Figure 3.2C, the deviation of $FWHM_{app}$ from the true dimension is most apparent for dimensions comparable or smaller than $FWHM_{loc}$, while measurements of larger structures are closer to their true values.

It is important to note that an additional systematic error is introduced when images are rendered by superimposing Gaussian distributions (Figure 3.2Aii). This rendering method effectively convolves the localization precision twice and further increases apparent structural dimensions. However, this effect is only evident for structures having sizes comparable to or smaller than $FWHM_{loc}$ (Figure 3.2C, blue curve) (Baddeley, Cannell et al. 2010). Furthermore, because fitting the Gaussian-blurred image is more robust to factors such as sampling frequency and pixel size than fitting a molecule density histogram (Figure 3.2C, insets), dimensions are often still measured from the Gaussian-blurred image.

Counting Molecule Numbers

Correcting for overcounting due to fluorophore blinking. One important prerequisite for absolute molecule counting is to correct for multiple observations of the same molecule due to fluorophore blinking. Blinking results in overcounting and false clustering of molecules (Annibale, Vanni et al. 2011). All current methods that correct for blinking require characterization of fluorophore properties using a monomeric, sparsely-distributed control sample ($Control_{mon}$) imaged under the same optical and chemical conditions as experimental samples (Coltharp, Kessler et al. 2012; Sengupta and Lippincott-Schwartz 2012).

A straightforward method to alleviate blinking artifacts is to identify spots localized close in space and time as those originating from a single molecule (see 'Chapter 4:

Accurate Construction of Photo-activated Localization Microscopy (PALM) Images for Quantitative Measurements'). If the spot grouping method cannot be applied (e.g. when fast activation is required), true molecule clustering can be distinguished from blinking-related self-

clustering using a pair-correlation function (PCF) (Veatch, Machta et al. 2012). The PCF describes the pair-wise distance correlation between all localized spots (see 'Identifying Spatial Distribution Patterns' below), which is the sum of the true spatial correlation function and the self-correlation function caused by blinking. The self-correlation PCF can be measured from the control sample ($\text{Control}_{\text{mon}}$) and subtracted from the experimental PCF to characterize true molecule clustering (Veatch, Machta et al. 2012).

Finally, the absolute number of detected molecules in a region can be estimated by dividing the number of localized spots by the average number of localizations per molecule (determined from $\text{Control}_{\text{mon}}$) without applying other blinking corrections (Coltharp, Kessler et al. 2012; Buss, Coltharp et al. 2013). This method only corrects mean molecule numbers and does not remove false clustering, so should not be used for analysis of spatial distribution patterns or clustering.

Correcting for undercounting due to inefficient molecule detection. Inefficient

fluorophore labeling and detection lead to undercounting of molecules in a structure. Because antibody binding often results in large variability in labeling efficiency, studies concerning absolute stoichiometry of complexes often use genetic labels such as fluorescent protein or affinity tag fusions (Puchner, Walter et al. 2013). The labeling efficiency of genetic fusions can approach unity, but detection efficiency remains a major concern with any fluorescent label (Durisic, Laparra-Cuervo et al. 2014; Wang, Moffitt et al. 2014). To calibrate for detection efficiency, a tandem dimer of two fluorophores, either the same or of different colors, can be constructed (Annibale, Scarselli et al. 2012; Renz, Daniels et al. 2012; Nan, Collisson et al. 2013; Puchner, Walter et al. 2013; Zhao, Roy et al. 2014). The construct should not self-associate and should be imaged under the same condition as the experimental samples. Assuming identical

detection efficiency, p , for each fluorophore, the frequency of singularly-detected dimers (N_s) and dually-detected dimers (N_d) follows a binomial distribution (Puchner, Walter et al. 2013; Durisic, Laparra-Cuervo et al. 2014). The detection efficiency can be estimated from the ratio $N_d/N_s = p^2/2p(1 - p)$ or by fitting to a binomial distribution (Puchner, Walter et al. 2013). Then, the true number of molecules in a structure can be determined by dividing the observed number of molecules in a structure by the detection efficiency.

Identifying Spatial Distribution Patterns

A list of corrected molecule coordinates can be used to characterize the spatial arrangement or clustering of detected molecules. In general, two classes of methods, correlation- or threshold-based, are used. Correlation-based methods use unbiased statistical analyses to describe overall clustering of molecules in an image. Threshold-based methods use experimenter-defined thresholds to segment clusters in an image and hence allow characterization of individual cluster properties.

Quantification of average cluster properties using correlation-based analyses. One common correlation-based method is the aforementioned pair-correlation function (PCF). The PCF calculates the probability of one molecule appearing at a certain distance r from another one (Sengupta, Jovanovic-Talisman et al. 2011) and can be computed using 2D FFT (fast Fourier transform) (Veatch, Machta et al. 2012). For randomly distributed molecules, the PCF curve is constant (related to the density of molecules) at different r (Figure 3.3Ci). For molecules distributed in clusters, the probability of finding molecules within clusters (smaller r) is higher than that outside (larger r), and hence the PCF curve has higher values at short distances and decays at longer distances (Figure 3.3Ci, blue and purple lines). Theoretically, analytical or

simulated PCF models can be generated by defining the form of cluster size and separation distributions (e.g. exponential or Gaussian). These models can then be fit to experimental curves to extract properties such as the average number of molecules per cluster and the mean cluster size (Sengupta, Jovanovic-Talisman et al. 2011; Veatch, Machta et al. 2012). However, prior knowledge of how clusters are distributed is often not clear, making interpretation of PCF curves highly model-dependent.

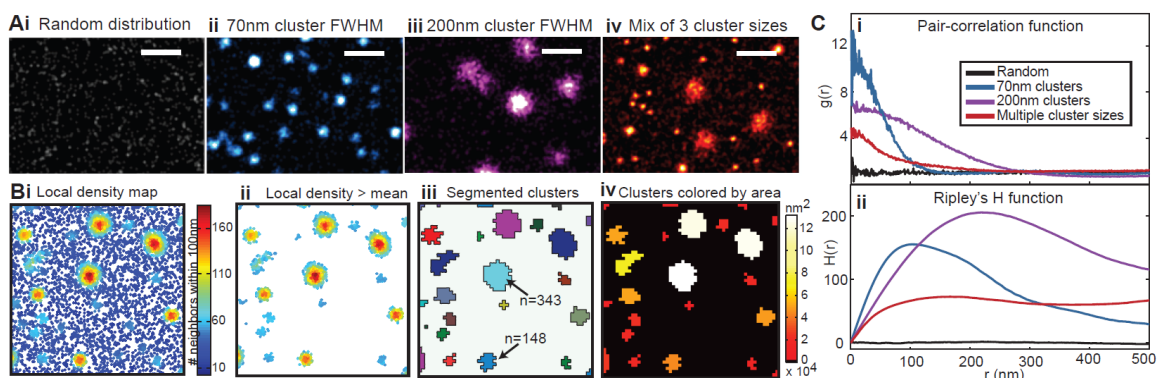


Figure 3.3 Analysis of molecule clustering.

(A) Simulated superresolution images of molecules distributed randomly (i), in small clusters (ii), in large clusters (iii), and in clusters of multiple sizes (iv). (B) Cluster identification and analysis from local density maps. (i) Local density of molecules is represented by the number of molecules within $100 \text{ nm} \times 100 \text{ nm}$ pixel. (ii) Clusters are clearly distinguished after removing molecules below a local density threshold (in this example, the threshold is the mean local density value). (iii) Clusters are segmented from a binary image generated from ii. The number of constituent molecules are shown for two clusters. (iv) Coloring each cluster by its area illustrates three populations of cluster sizes: large (white), medium (orange), and small (red). (C) Statistical analyses by pair-correlation function (PCF) (i) and Ripley's functions (ii) show distinct curve shapes for the simulations shown in A. For homogenous cluster distributions (blue, purple), cluster sizes can be approximated from the pair-correlation decay length (i) or the peak position of Ripley's H function (ii). However, extracting the mixed cluster sizes (red) is not intuitive for either curve. Scale bars, 500 nm.

Another method, Ripley's K function, $K(r)$, describes the average number of molecules that exist near another molecule within different radius (r) (Penttinen and Stoyan 2000). Conceptually it can be regarded as the cumulative form of the PCF. Similar to the PCF, Ripley's K function can easily discriminate clustered distributions from uniform distributions. In a uniform distribution,

$K(r)$, the number of molecules within a radius of r , is proportional to πr^2 . Normalization of $K(r)$ gives rise to Ripley's H function ($H(r) = \sqrt{K(r)/\pi} - r$), which is zero across all distances for a uniform distribution (Figure 3.3Cii, black curve). For a clustered distribution, $H(r)$ peaks at a characteristic r , which is related to the cluster size; the peak height depends on the mean molecule density in clusters (Figure 3.3Cii, blue and purple curves). Lagache et al. suggested another normalization of the Ripley's function for quantitative model fitting and easier parameter extracting (Lagache, Lang et al. 2013).

Both the PCF and Ripley's functions have been widely used to analyze different types of protein clusters such as membrane receptors (Kiskowski, Hancock et al. 2009; Sengupta, Jovanovic-Talisman et al. 2011; Lee, Shin et al. 2012; Veatch, Machta et al. 2012). This is because both functions' shape and amplitude can be intuitively compared with that expected from theoretical calculations to discriminate different models (Sengupta, Jovanovic-Talisman et al. 2011; Veatch, Machta et al. 2012). However, it is important to account for the self-clustering effect due to fluorophore blinking to avoid misinterpretation of clustering at short distances (see 'Counting Molecule Numbers' above). In addition, both methods work best when there is only one type of cluster —heterogeneous distributions of multiple cluster types in the same image result in PCF and Ripley's H curves that are difficult to interpret (Figure 3.3Ci and ii, purple curves).

Additionally, quantitative parameter extraction from either function is highly model-dependent, and different cluster properties can generate similar curves with both methods. Thus a prior biological understanding of cluster properties is often required (Hess, Gould et al. 2007; Kiskowski, Hancock et al. 2009). Finally, it is important to note that these functions exhibit edge effects when the neighbor-search region defined by r extends beyond the image boundaries. This results in significant underestimation of clustering and correlation at large r values. Thus,

PCF or Ripley's functions should not be interpreted at r values greater than $\sim 1/3$ of the smallest image dimension without first applying edge-correction methods (Ripley 1989; Haase 1995).

Detection and quantification of individual clusters using threshold-based methods.

Threshold-based methods are model-independent and rely on segmentation of images or grouping of spots from coordinate lists to isolate individual clusters. When clusters are sparsely distributed, molecules within the same cluster can be grouped together by their proximity using a distance threshold similar to that used for blinking correction (see 'Counting Molecule Numbers' above) (Gunzenhauser, Olivier et al. 2012; Nan, Collisson et al. 2013). When clusters are densely-distributed and/or when their sizes have wide distributions, more sophisticated methods are required. For example, tree-clustering methods based on informational theory can be used to group molecules belonging to the same cluster (Greenfield, McEvoy et al. 2009). Cluster boundaries can also be determined using thresholds of fluorescence intensity (Buss, Coltharp et al. 2013) or the local density of each molecule (e.g. number of nearby molecules or nearest neighbor distance) (Figure 3.3B) (Bar-On, Wolter et al. 2012; Scarselli, Annibale et al. 2012; MacGillavry, Song et al. 2013; Nan, Collisson et al. 2013; Ori, Banterle et al. 2013; Tarancon Diez, Bonsch et al. 2014). These thresholds can be normalized (e.g. local density normalized by the average local density) for application to samples with different expression levels or sampling, and are often optimized using simulations that mimic the experimental data (MacGillavry, Song et al. 2013).

Once cluster boundaries are identified, properties such as cluster area, molecule density, and symmetry can be characterized to describe how different biological states affect these features (Buss, Coltharp et al. 2013) (Figure 3.3B, iii-iv). These measurements can reveal assembly

mechanisms (Bar-On, Wolter et al. 2012), differences in oligomeric states (Nan, Collisson et al. 2013; Puchner, Walter et al. 2013) or relative constituent stoichiometry (Ori, Banterle et al. 2013) in different biological conditions. Ligand binding affinities have also been directly measured in individual cells by counting the number of sparsely-distributed receptor-ligand complexes at different concentrations of fluorescent ligand (Dietz, Fricke et al. 2014).

Colocalization

Multicolor superresolution imaging provides the ability to quantify colocalization with spatial resolutions that approach molecule dimensions. Colocalization observed at this scale is more likely to indicate true molecular interactions than colocalization detected with conventional fluorescence microscopy. This precision also results in higher sensitivity to chromatic aberrations between different fluorescence channels. These aberrations can be computationally corrected if first characterized using multi-colored fluorescent beads (Fletcher, Scriven et al. 2010). Another important consideration is that low sampling frequency caused by inefficient labeling and detection of fluorophores can decrease the apparent colocalization, leading to false negatives. Control experiments for measuring labeling and detection efficiency should be introduced to verify the colocalization results (Annibale, Scarselli et al. 2012; Renz, Daniels et al. 2012; Zhao, Roy et al. 2014).

Colocalization between different species can often be visually identified as intensity overlap in superresolution images (Figure 3.4Aiii) (Ribeiro, Vagnarelli et al. 2010; Lew, Lee et al. 2011; Zhao, Bruck et al. 2013). Comparing colocalization under different conditions, however, requires statistical analysis of the fluorescence intensity or molecule coordinates of each species. Intensity-based metrics used in conventional fluorescence microscopy have been critically

reviewed and compiled into an ImageJ plug-in by Bolte and Cordelières (Bolte and Cordelières 2006), and can be easily applied to superresolution images (Zhao, Bruck et al. 2013; Bielopolski, Lam et al. 2014). For example, the Manders' coefficient calculates the correlation between pixel intensities recorded in two different channels (Figure 3.4B, magenta bars). This metric is robust to regions of different sizes used for analysis (Figure 3.4B i vs. ii), but can produce false-negatives with under-sampled images (Figure 3.4B iii vs. iv).

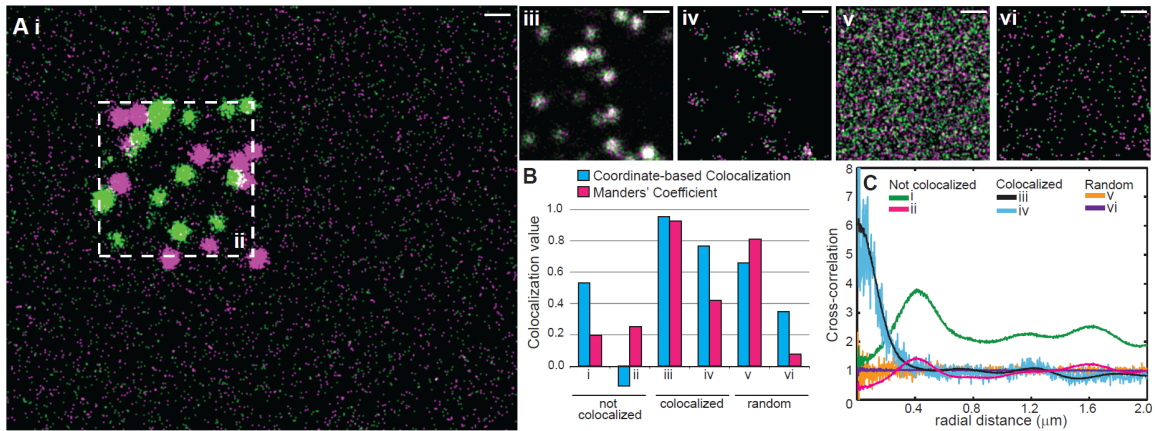


Figure 3.4 Colocalization analysis.

(Ai to Avi) Representative superresolution images with two simulated species (green and purple; white represents overlap). (i and ii) The two species form self clusters and are randomly distributed with respect to each other in a large region (i) or a small region (ii). (iii and iv) The two species form self clusters and colocalize with each other, but are detected with high (iii) and low (iv) efficiency respectively. (v and vi) the two species do not form self clusters, are randomly distributed, and detected with high (v) and low (vi) efficiency. (B). Comparison of the coordinate-based colocalization (CBC) algorithm (Malkusch, Endesfelder et al. 2012) and Manders' Coefficient analysis of images Ai to Avi. CBC values were calculated using $R_{max} = 1/3$ of the maximum distance between any two molecules. (C) Comparison of cross-correlation analysis of images Ai to Avi.

Coordinate-based methods analyze the distances between molecules to determine whether two species localize near each other (Malkusch, Endesfelder et al. 2012; Rossy, Cohen et al. 2014).

Malkush et al. developed a coordinate-based colocalization (CBC) algorithm to assign a

colocalization value for each molecule using the ranked correlation between the number of 'self' vs. 'other' molecules located within varying r values (Malkusch, Endesfelder et al. 2012). In addition to allowing comparison of average colocalization values of different images (Figure 3.4B), this method can provide a histogram or colocalization map, in which areas of high colocalization between two species can be visually identified (Malkusch, Endesfelder et al. 2012). Note that this method can exhibit edge effects for the same reasons outlined for the Ripley's and PCF functions above. Because edge effects influence both 'self' and 'other' molecules similarly, the two species can seem highly correlated at large r values, resulting in artificially high CBC values for small region sizes. Thus, it is a good practice to limit the maximum r value (R_{max}) used for the CBC calculations to 1/2 or less of the maximum observed distance between any two molecules (Figure 3.4B), and it may be useful to adapt an edge-correction method from Ripley's analysis (Ripley 1989; Haase 1995). Additionally, region size itself should also be considered when interpreting colocalization values provided by this and other coordinate-based methods. For example, although the two species of clusters in A_i are not coincident, they exhibit high colocalization values (Figure 3.4Bi) because both species are localized to the same general sub-region (Figure 3.4Bii). When only the sub-region is analyzed, low colocalization values are observed (Figure 3.4Bii). Hence, region size affects the interpretation of the colocalization values, and direct comparison between different images requires comparable region selection.

Other commonly-used coordinate-based methods are the aforementioned Ripley's functions and PCF (see 'Identifying Spatial Distribution Patterns' above). Both methods can be derived to accommodate multiple species and thus describe the degree of colocalization (Lehmann, Rocha et al. 2011; Sherman, Barr et al. 2011; Notelaers, Rocha et al. 2014). These methods generate distance-dependent cross-correlation curves of the whole image rather than providing

colocalization values for individual molecules (Figure 3.4C). Although the amplitudes of these cross-correlation curves depend on the size of the region of interest (Figure 3.4C i vs. ii), the distance value at which maximal correlation values are observed, or the average correlation decay length, is absolute and indicative of the average colocalization displacement between the two species (Veatch, Machta et al. 2012). Cross-correlation analysis is also robust to under-sampling, which adds noise but does not alter curve shapes (Figure 3.4C iii vs. iv). Moreover, cross-correlation analysis can distinguish random colocalization that results from high molecule densities from co-clustering (Figure 3.4C iii vs v). Note that these cross-correlation-based methods are not affected by the overcounting artifacts caused by fluorophore blinking, as they all calculate the correlation of one species with the other but not with itself (Veatch, Machta et al. 2012). This feature could be utilized to analyze whether a single species self-clusters with itself by labeling the same species with two different labels.

Outlook

The next revolution in superresolution imaging will likely involve the ability to simultaneously determine the activity of single molecules in addition to their locations, perhaps by incorporating other fluorescence techniques such as FRET (Grecco and Verveer 2011) or fluorescent protein complementation (Liu, Xing et al. 2014; Nickerson, Huang et al. 2014). In the more immediate future, the growing number of 3D implementations of PALM and STORM (Klein, Proppert et al. 2014) will require rapid adaptation of these techniques to 3D structural analyses. Furthermore, to increase the accessibility of these future advancements and the quantitative analyses presented here, the field requires development of robust toolkits to generate reliable control constructs (Schmied, Raab et al. 2014).

For microbiological specimens, superresolution imaging would benefit from several areas of fluorescent probe development. First, development of dyes that efficiently penetrate the cell wall would allow implementation of dSTORM investigations in live bacterial cells and the use of smaller genetic tags as binding targets. Furthermore, fluorescent probes that can be efficiently controlled with wavelengths of light longer than the commonly used 405nm will extend the time-lapse, live-cell imaging capability of localization-based methods. Finally, labeling strategies involving unnatural amino acids (Plass, Milles et al. 2011; Milles, Tyagi et al. 2012; Plass, Milles et al. 2012) or protease cleavage (Chattopadhyaya, Abu Bakar et al. 2008), which entail single amino acid substitutions, may provide ways to perform superresolution imaging with minimal perturbations to protein function.

Chapter 4 :

Accurate Construction of Photo-activated Localization Microscopy (PALM) Images for Quantitative Measurements

Adapted with permission from:

Coltharp, C., Kessler, R., Xiao, J. Accurate construction of photoactivated localization microscopy (PALM) images for quantitative measurements. **PloS one** (2012).

Introduction

Localization-based superresolution methods such as Photoactivated Localization Microscopy (PALM), Stochastic Optical Reconstruction Microscopy (STORM), and direct STORM (dSTORM) utilize the stochastic switching of fluorophores between dark and bright emission states to visualize fluorophore-labeled single molecules sequentially from the ensemble pool (Betzig, Patterson et al. 2006; Rust, Bates et al. 2006; Heilemann, van de Linde et al. 2008). The position of each molecule is localized with nanometer precision by fitting its spot intensity profile to a two-dimensional Gaussian function that approximates its point spread function (PSF) (Thompson, Larson et al. 2002). A superresolution image is then generated by overlaying the detected molecule positions. From the superresolution image or the original list of molecule positions, one can quantitatively measure the dimensions and molecule density (number of molecules per unit area) of nanometer-scale cellular structures.

Other PALM and (d)STORM studies have resolved the dimensions of structures such as the ParA bundles that segregate *Caulobacter crescentus* chromosomes (Ptacin, Lee et al. 2010), microtubule filaments (Bates, Huang et al. 2007; Heilemann, van de Linde et al. 2008), actin filaments (Heilemann, van de Linde et al. 2008), clathrin pits (Huang, Wang et al. 2008), budding HIV-1 virions (Lehmann, Rocha et al. 2011; Lelek, Di Nunzio et al. 2012), clusters of bacterial histone-like proteins (Wang, Li et al. 2011), and membrane receptor clusters (Geisbrecht, Bouyain et al. 2006; Hsu and Baumgart 2011). Furthermore, molecule density measurements have allowed investigation of the maturation (Shroff, Galbraith et al. 2008) and mechanical load (Chien, Kuo et al. 2011) of focal adhesions, the assembly of microclusters following T cell activation (Geisbrecht, Bouyain et al. 2006; Hsu and Baumgart 2011; Sherman, Barr et al. 2011), assembly of bacterial chemotaxis clusters (Greenfield, McEvoy et al. 2009), and the

reorganization of membrane protein clusters upon cholesterol addition or depletion (Sengupta, Jovanovic-Taliman et al. 2011). The growing body of examples highlights the great potential of obtaining quantitative information such as structural dimensions, stoichiometry, and molecule density from localization-based superresolution studies. However, care must be taken to ensure the reliability of superresolution data. Many factors influence the resulting superresolution images, including the method of image reconstruction (Baddeley, Cannell et al. 2010), acquisition conditions (van de Linde, Wolter et al. 2010; Wolter, Endesfelder et al. 2011), and movement of the structure of interest. This chapter focuses on one issue that significantly affects the accuracy of quantitative density measurements in PALM imaging — fluorophore blinking.

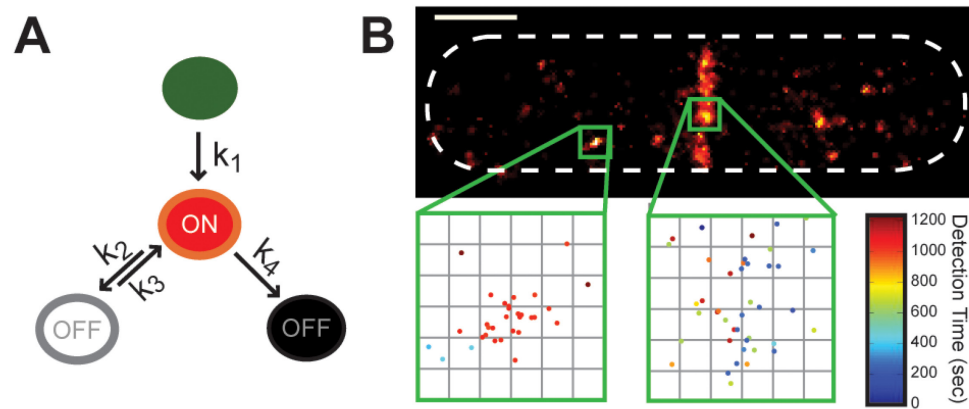


Figure 4.1 Fluorophore blinking affects superresolution image quality.

(A) Simplified kinetic scheme of a photoactivatable fluorophore such as mEos2. The fluorophore is irreversibly photoactivated with rate constant k_1 , can transiently access a nonfluorescent state with rate constant k_2 , return to the fluorescent state with rate constant k_3 , and irreversibly photobleach with rate constant k_4 . (B) Superresolution image of an *E. coli* cell expressing FtsZ-mEos2 generated with conventional clustering thresholds: spots within 167nm (1 camera pixel) and 50ms (1 frame) of each other were grouped together and plotted once. The cytoplasmic cluster (left inset) consists of spots detected very closely in time, suggesting that they came from the same fluorophore, whereas a dense section inside the Z-ring (right inset) contains spots detected throughout the experiment. Scale bar, 500nm. Inset grid size, 30nm.

Many photoactivatable fluorescent proteins have recently been shown to fluoresce intermittently, or “blink”, once activated (Annibale, Vanni et al. 2011; Annibale, Vanni et al. 2011; Endesfelder, Malkusch et al. 2011). Figure 4.1A shows a simplified reaction scheme of the intermittent fluorescing behavior of a generic photoactivatable fluorescent protein. An activated fluorophore can reversibly transit between a nonfluorescent state (white) and a fluorescent state (red), or can be irreversibly photobleached (black) from the fluorescent state. Intermittent fluorophore blinking leads to overcounting artifacts where single molecules are represented multiple times, resulting in images that are often characterized by a punctate quality (Annibale, Scarselli et al. 2010; Annibale, Vanni et al. 2011; Annibale, Vanni et al. 2011; Sengupta, Jovanovic-Talman et al. 2011).

To illustrate this point, Figure 4.1B shows a superresolution image of an *Escherichia coli* cell expressing the FtsZ protein fused to mEos2, a photoactivatable fluorescent protein and a popular choice for PALM imaging (McKinney, Murphy et al. 2009). In addition to the expected midcell Z-ring formed by FtsZ, the image shows bright cytoplasmic clusters of FtsZ-mEos2. The time-coded insets show that some of these clusters are comprised of spots that were detected very closely in time, in contrast to a region inside the Z-ring where multiple localizations were randomly detected in time. As the activation rate of new fluorophores is usually kept very low in superresolution imaging, these multiple localizations in the cytoplasmic cluster likely come from the same mEos2 molecule rather than multiple molecules.

In various attempts to account for photoblinking so that each molecule in a superresolution image is represented only once, several studies have employed a simple clustering algorithm to group multiple localizations of a single molecule based on the occurrence of these localizations

within certain time and distance thresholds (t_{Thresh} and d_{Thresh}) — if two localizations occur within t_{Thresh} and d_{Thresh} , they likely come from the same molecule and should be grouped together (Greenfield, McEvoy et al. 2009; Lillemeier, Mortelmaier et al. 2010; Annibale, Vanni et al. 2011; Sengupta, Jovanovic-Talisman et al. 2011; Lando, Endesfelder et al. 2012). Each group is then plotted only once in the superresolution image. This type of clustering algorithm was employed in the original demonstrations of STORM and PALM, where fluorescence spots detected within one camera pixel ($d_{Thresh} = 167\text{nm}$ for our system) and separated by up to one or three frames, respectively, were grouped together (Betzig, Patterson et al. 2006; Bates, Huang et al. 2007). Generous values for both thresholds can ensure that multiple molecule localizations are grouped together, but may result in false grouping of separate molecules and underestimation of molecule density. It was noted that these thresholds should be optimized based on each fluorophore's photophysical properties (Betzig, Patterson et al. 2006; Annibale, Scarselli et al. 2010), but a procedure to identify optimal t_{Thresh} and d_{Thresh} values that accurately group localized spots has yet to be developed.

In this study, experimental and simulated data were analyzed to determine how photoblinking kinetics and threshold selection affect the dimension and molecule density measurements described above. These analyses were performed on superresolution images of fixed *E. coli* cells expressing FtsZ-mEos2, whose heterogeneous distribution between midcell and cytoplasmic populations presents a challenging, but ideal, test case for the clustering algorithm. The observed effects were then explored and corroborated using simulated datasets in which fluorophore blinking was simulated according to the kinetic scheme shown in Figure 4.1A.

The simulations confirm that blinking-related overcounting increases absolute density measurements, but measurements of dimension and relative density are not affected. They also reveal that applying a clustering algorithm can result in inaccurate measurements of both density and dimension measurements unless proper threshold values are chosen and fluorophore activation is slow enough to allow accurate grouping of molecule localizations.

The above analyses identified a simple method for determining the maximum activation rate for a given sample and for selecting optimal t_{Thresh} and d_{Thresh} values to generate reliable superresolution images. The generality of this method was also explored using simulations of circular clusters of various sizes, which yielded similar results to the FtsZ simulations, suggesting that these principles are applicable to the measurements of cellular structures of different geometries.

In contrast to other recent methods that account for photoblinking (Annibale, Vanni et al. 2011; Sengupta, Jovanovic-Talisman et al. 2011), which summarize structural properties with global parameters, the optimized clustering method presented here provides the full, corrected, superresolution image and list of molecule positions, which can be quantified in various ways depending on the unique properties of different biological structures. This flexibility is especially useful for heterogeneous cellular structures with regions of high and low molecule density or unusual geometries. Lastly, because this method is a simple improvement of existing PALM clustering algorithms, its implementation is simple and straightforward.

Results

Dimension measurements are not affected by fluorophore blinking, but can be affected by applying a clustering algorithm

Structural dimensions are often measured from superresolution images by fitting feature intensity (or density) profiles to Gaussian distributions and extracting the full width at half maximum (FWHM) (Bates, Huang et al. 2007; Fu, Huang et al. 2010; Wang, Li et al. 2011). Figure 4.2A shows an example of how the width of the Z-ring is measured in this way. It is important to note that the measured FWHM of a feature is a convolution of the actual feature dimension with the achievable spatial resolution often described as a Gaussian function, the standard deviation of which is determined by the positional variation of multiple localizations of the same molecule (see 'Appendix 1'). The observed FWHM can be further broadened by the image construction method, which often entails plotting each localized molecule as a Gaussian spot with standard deviation equal to the localization precision (Baddeley, Cannell et al. 2010). Nevertheless, even with these statistical broadening effects, the FWHM serves as a convenient measurement for structural dimension comparison. Furthermore, with prior knowledge of the distribution of molecules within a structure, the true dimension can be deconvolved (Bates, Huang et al. 2007). For simplicity, in the following analyses Z-ring width is quantified as the apparent FWHM from a single Gaussian fit.

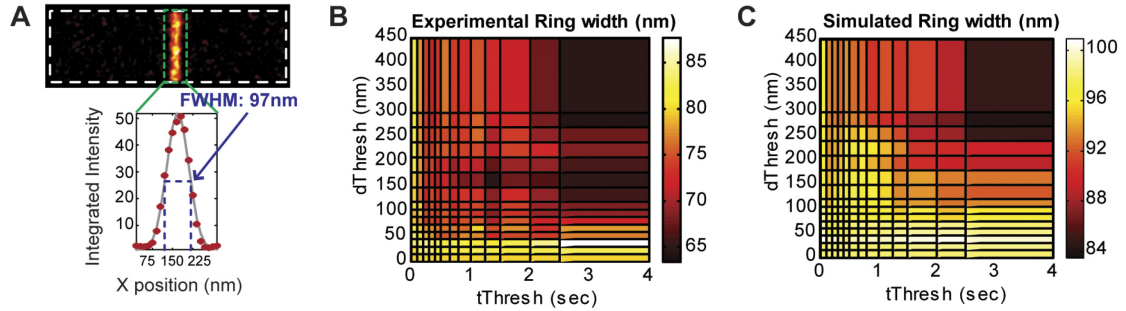


Figure 4.2 Effects of threshold selection on Z-ring width measurement.

(A) Representative Z-ring width measurement of a simulated image where each molecule is only represented once. The intensity along the short axis of the cell is projected onto one dimension (red circles), and then fit to a Gaussian distribution (gray line). The FWHM (97nm, blue dotted line) is calculated as $2.35 \cdot \sigma$, where σ is the fitted Gaussian standard deviation. (B) and (C) Z-ring width values (indicated by the heat map) calculated from images generated by applying different threshold pairs for an experimental dataset (B) and a simulated dataset (C). The simulated dataset was generated using the following parameters: $N_{\text{total}} = 2000$ (50% in the Z-ring), $\sigma = 15\text{nm}$, $\langle n_{\text{blink}} \rangle = 2$, $\langle \tau_{\text{off}} \rangle = 1$ frame, $\langle \tau_{\text{on}} \rangle = 1$ frame, $\langle \tau_{\text{act}}^0 \rangle = 5$ frames (1 frame = 50ms). The Z-ring width calculated from the reference image (A), where each molecule is represented only once, is 97nm, which is similar to the measurements made from images constructed using low values of t_{Thresh} or d_{Thresh} .

To determine the effect of threshold selection on dimension measurement, the clustering algorithm (see 'Clustering algorithm' in Methods section) was applied with varying t_{Thresh} and d_{Thresh} values to both experimental and simulated data. Different threshold pairs were applied to a single experimental dataset obtained with FtsZ-mEos2 to generate a series of superresolution images. Across the investigated threshold range (t_{Thresh} : 0 - 4 sec, d_{Thresh} : 0 - 450nm), Z-ring width varied approximately 1.5-fold (60 - 90 nm) with larger threshold values resulting in smaller width measurements (Figure 4.2B). The same trend was observed with measurements made from a simulated dataset (Figure 4.2C) where molecules were allowed to blink according to the kinetic scheme in Figure 4.1A (see 'Simulation of fluorophore blinking kinetics' in the Methods section for simulation procedure and parameters). Measurement of the "true" Z-ring width were measured from a reference image in which each molecule is only localized once. The Z-ring width measured from this reference image (97nm) represents the expected value from an image

with no photoblinking artifacts. Widths measured from images generated with most small threshold pairs ($t_{Thresh} < 1$ s and $d_{Thresh} < 100$ nm) were within the 95% confidence interval for the fitted Z-ring width in the reference image (94nm - 100nm), while extremely high threshold values yielded much smaller Z-ring width measurements.

The general decrease in Z-ring width measurement at large thresholds is due to false grouping of localizations that originated from multiple molecules, which affects dimension measurements in two ways. First, because the convolved Z-ring profile is described by a Gaussian distribution, groups that are comprised of multiple molecules have centroid positions weighted toward the center of the Z-ring. Plotting these centroid positions tightens the spatial distribution of the Z-ring and results in smaller width measurements. Second, very large thresholds can cause insufficient sampling of the Z-ring, resulting in further reduced width measurements.

Note that when no clustering is applied (t_{Thresh} and d_{Thresh} values of 0), the Z-ring width measured from the simulated data approximates that measured from the reference image. This can be understood if multiple localizations of the same molecule result in an increased amplitude but unchanged standard deviation of the Z-ring Gaussian distribution. This observation is consistent with previous studies where it was shown that multiple localizations of fluorophores improves the statistical sampling of underlying structures and can increase the apparent spatial resolution of a superresolution image (van de Linde, Wolter et al. 2010; Dempsey, Vaughan et al. 2011; Jones, Shim et al. 2011). Therefore, reliable dimension measurements can be obtained from a superresolution image that has not been processed using a clustering algorithm, as long as the structure of interest is sampled sufficiently. It is also evident that, if a clustering algorithm is applied, the thresholds should be low enough to avoid underestimation due to false clustering.

Effects of fluorophore blinking and clustering thresholds on density measurements

Counting the number of fluorescent molecules detected within a given structure provides information about the molecule density of the protein of interest when labeling stoichiometry and the fraction of fluorophores detected are taken into account. In a PALM experiment, the fraction of detected fluorophores is limited because not every fluorescent molecule can be activated and visualized on a finite timescale, and because a substantial fraction (up to 20%) may not be activatable due to misfolding or incomplete fluorophore maturation (Garcia-Parajo, Koopman et al. 2001; Ulbrich and Isacoff 2007). However, even with these limitations, molecule counting can still inform structural models by providing a lower bound of molecule density, which can suggest a minimum number of layers or subunits within a structure.

Fluorophore blinking results in erroneous amplification of fluorophore density due to repeat localizations. The following characterizations explore how t_{Thresh} and d_{Thresh} selection affects three types of measurements: mean density, relative density, and density distribution measurements. Mean density is a bulk measurement of the average number of molecules per unit area; relative density reports the fraction of molecules confined to a particular region of the structure; and the density distribution is described by the histogram of number of molecules detected per unit area. Fluorophore blinking amplifies both mean density and density distributions, which are absolute measurements of molecule counts, but relative density, which is the ratio between molecule counts in different regions, should not be affected if all molecules have the same ensemble blinking properties.

Mean density measurements are affected by fluorophore blinking and by applying a clustering algorithm

The effect of t_{Thresh} and d_{Thresh} selection on mean density (molecules per unit area) was examined using the same experimental and simulated datasets shown in the dimension measurement analysis in Figure 4.2 by analyzing how the total number of molecules (N) in the same cell area varies with different t_{Thresh} and d_{Thresh} pairs. Both experimental (Figure 4.3A) and simulated (Figure 4.3B) datasets display the same trend: larger thresholds yield lower mean densities (N /cell area) because more spots are grouped together. For the simulated dataset, determining the fractional difference of N from the true value obtained from the reference image, $|(N - N_{ref})/N_{ref}|$ revealed that reasonably accurate mean density measurements (<10% difference from N_{ref}) can be achieved by multiple threshold pairs along two valleys that intersect at $t_{Thresh} \approx 0.4$ s and $d_{Thresh} \approx 60$ nm (Figure 4.3C).

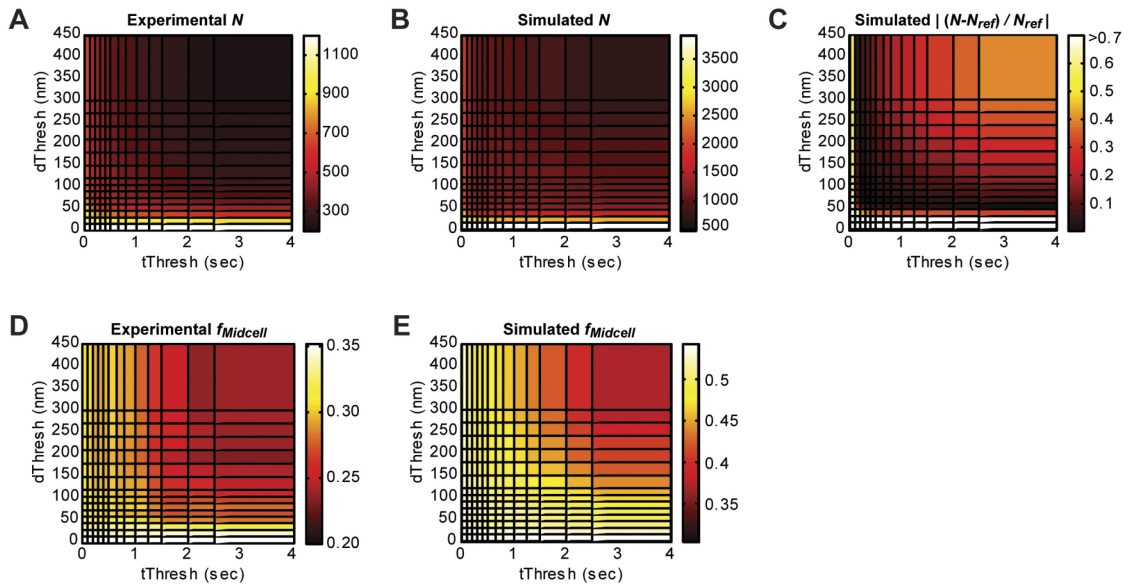


Figure 4.3 Effects of threshold selection on mean and relative molecule density.

(A) and (B) Total number of molecules, N , in images generated by applying different threshold pairs to an experimental dataset (A) and a simulated dataset (B). (C) Fractional difference $|(N-N_{ref})/N_{ref}|$ between each reconstructed simulated image and the number of molecules in the reference simulated image ($N_{ref} = 1248$). Images with small fractional differences (dark areas) are generated from threshold pairs found along two intersecting valleys. (D) and (E) Fraction of molecules located at the midplane ($f_{midcell}$) in images generated by applying different threshold pairs for an experimental dataset (D) and a simulated dataset (E). In the reference image, $f_{midcell} = 0.53$, which is most similar to the values calculated from images generated using low values of both $d_{Threshold}$ and $t_{Threshold}$. Datasets analyzed are the same as those shown in Figure 4.2.

Relative density measurements are not affected by fluorophore blinking, but can be affected by applying a clustering algorithm

The effect of $t_{Threshold}$ and $d_{Threshold}$ selection on relative density measurements was examined by measuring $f_{midcell}$, the fraction of molecules detected in the Z-ring relative to the whole cell.

Increasing values of both $t_{Threshold}$ and $d_{Threshold}$ resulted in smaller $f_{midcell}$ values for both experimental (Figure 4.3D) and simulated (Figure 4.3E) datasets. Comparison with the $f_{midcell}$ value calculated from the reference image (0.53) revealed that images generated with smaller thresholds yielded reasonably accurate relative density measurements ($< 10\%$ difference for $t_{Threshold} < 1$ s and $d_{Threshold} <$

105 nm). This is because molecules within and outside the structure of interest have the same blinking properties, allowing the effect of multiple molecule localizations to cancel out in a relative measurement. The underestimation of $f_{midcell}$ for larger threshold values is due to the greater likelihood of falsely grouping molecules in denser regions such as the Z-ring. These results confirm that, as with the Z-ring width measurement, relative density can be accurately measured from a superresolution image that has not been processed using a clustering algorithm (t_{Thresh} and d_{Thresh} equal to 0), as long as the structure of interest is sampled sufficiently.

Molecule density distributions are affected by fluorophore blinking and by applying a clustering algorithm

While mean and relative molecule densities describe global structural properties, the molecule density distribution provides additional information about the uniformity or heterogeneity of molecule positions within a structure. If molecules are uniformly distributed throughout the structure, the molecule density histogram should be well described by a Poisson distribution. Figure 4.4A shows the histogram of molecules detected per superresolution pixel (15 nm x 15 nm) within the Z-ring of the simulated dataset before any clustering algorithm is applied. A Pearson χ^2 goodness-of-fit test (Pearson 1900) shows that this distribution deviates from a Poisson distribution significantly ($p_{GOF} = 0$). This seemingly heterogeneous distribution of molecules inside the Z-ring, as judged by the significant deviation from Poisson distribution, is actually caused by multiple localizations of single molecules due to photoblinking. Figure 4.4B shows that the Z-ring molecule density of the corresponding reference image where each molecule is only localized once can be described by a Poisson distribution adequately ($p_{GOF} = 0.74$).

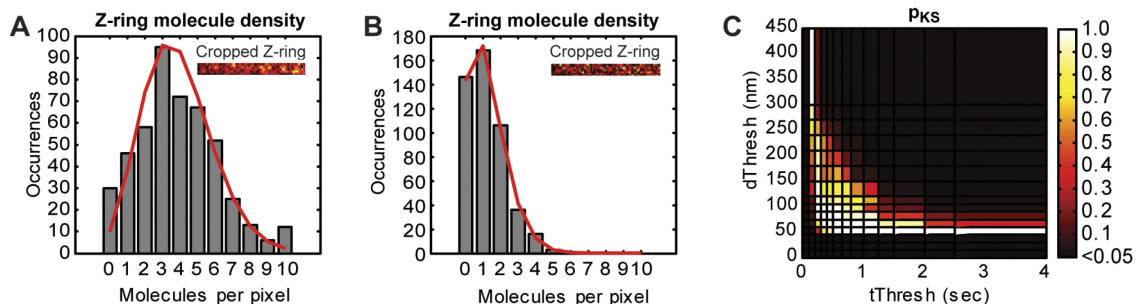


Figure 4.4 Effects of threshold selection on molecule density distribution in the Z-ring.

(A) Histogram (gray bars) of molecules per pixel (15nm x 15nm) inside the Z-ring of a simulated image that was not processed with a clustering algorithm. (B) Histogram (gray bars) of molecules per pixel of the corresponding reference image, where each molecule is represented only once. Poisson distributions simulated with the sample means, 3.9 (A) and 1.2 (B) molecules per pixel, are shown in red. The ratio of mean values reflects the localization of each molecule approximately three times due to the simulated photoblinking kinetics ($\langle n_{\text{blink}} \rangle = 2$, $\langle \tau_{\text{off}} \rangle = 1$ frame, $\langle \tau_{\text{on}} \rangle = 1$ frame). Poisson goodness-of-fit tests resulted in $p_{\text{GOF}} = 0$ for distribution in (A), suggesting that blinking results in deviations from a Poisson density distribution ($p_{\text{GOF}} = 0.74$ for the reference distribution in (B)). Insets show the cropped Z-ring regions used to generate the histograms. (C) p-values from the KS-test when the molecule density distribution of the Z-ring generated by the reference image (B) is compared with distributions in images generated with different threshold pairs. Distributions that resulted in $p_{\text{KS}} > 0.05$ are not significantly different from the distribution in the reference image. Dataset analyzed is the same simulated dataset shown in Figure 4.2 and Figure 4.3.

To identify the clustering thresholds that generate the correct molecule density distributions, Z-ring molecule density distributions generated with different t_{Thresh} and d_{Thresh} pairs were compared to the distribution from the reference image using the Kolmogorov–Smirnov (KS) test (Massey 1951). As with mean density, density distributions are similar to the reference distribution ($p_{\text{KS}} > 0.05$) along two intersecting ridges (Figure 4.4C), indicating that the thresholds in this region generate images that most faithfully represent the true molecule distributions.

Multiple threshold pairs can result in accurate measurements of both dimension and density measurements

This study has shown that the mean molecule density and density histogram measurements are significantly affected by fluorophore blinking, while dimension and relative density measurements are not. However, all four measurements are affected by the selection of t_{Thresh}

and d_{Thresh} . These measurements can be made within a reasonable range of the true value if correct threshold values are chosen. To find the threshold region that simultaneously represents all four measurements with reasonable accuracy, the relative errors obtained at different threshold pairs were combined for each measurement made from the simulated images described in Figure 4.2, Figure 4.3, and Figure 4.4. Figure 4.5A shows the region (white squares) where Z-ring width, $f_{midcell}$, and N measurements are within 10% of the reference values and density distributions were not significantly different from the reference distribution ($p_{KS} > 0.05$).

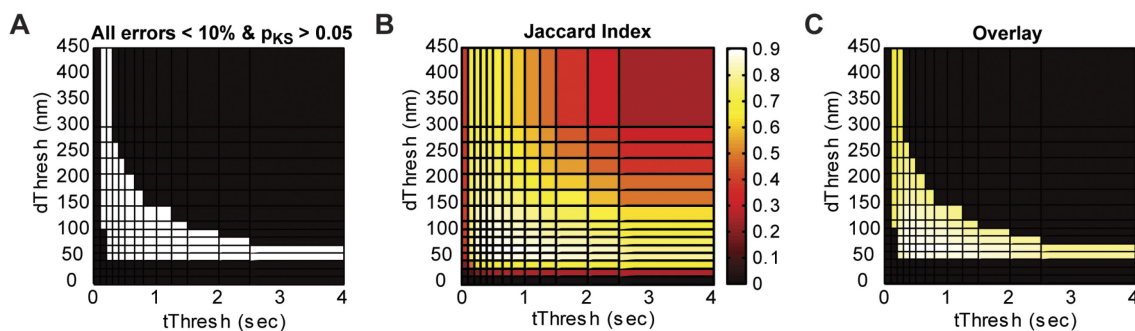


Figure 4.5 Accuracy of images generated with different threshold pairs.

(A) Region of threshold space (white squares) that resulted in $< 10\%$ difference from the reference measurements of Z-ring width, N , and $f_{midcell}$, and that yielded Z-ring density distributions not significantly different from the reference distribution ($p_{KS} > 0.05$). (B) Jaccard index values at each threshold pair. Higher Jaccard index values indicate more accurate single-molecule clustering. (C) The peak of the Jaccard index plot (B, white squares) is within the region where all four quantitative measurements are within 10% of the reference measurements (A). Dataset analyzed is the same simulated dataset shown in Figure 4.2, Figure 4.3, and Figure 4.4.

The Jaccard Index identifies images that are accurate on both the ensemble and single-molecule level

The combined error analysis selected a limited threshold range rather than a unique, optimal threshold pair. While this range of thresholds can satisfy all investigated quantitative measurements simultaneously, some threshold pairs in this range may not generate accurate

superresolution images in which the molecule counts and positions are correctly identified. This is because each of the measurements described above quantifies an ensemble structural property and may not be sensitive to errors at the individual molecule level.

To find the optimal threshold pair that not only provides reliable quantitative measurements, but also an accurate image at the single-molecule level, the clustering accuracy of each threshold pair was further assessed using the Jaccard index (Gower and Legendre 1986; Jackson, Somers et al. 1989). The Jaccard index compares how frequently localizations of the same molecule are correctly grouped together (true positives), how frequently localizations of different molecules are incorrectly grouped together (false positives), and how frequently localizations from the same molecule are not grouped together (false negatives) (see Methods for details). The Jaccard index, therefore, reflects clustering accuracy at the individual molecule level; higher Jaccard index values indicate more accurate grouping, and consequently more accurate image reconstruction.

The Jaccard Index was calculated as a function of t_{Thresh} and d_{Thresh} (Figure 4.5B) for the simulated dataset described above and observed a clear peak at $t_{Thresh} = 0.4$ s and $d_{Thresh} = 60$ nm. This peak position is within the optimal threshold region selected by the combined measurement error plot (Figure 4.5A). This agreement, illustrated by the overlay plot in Figure 4.5C, confirms that the t_{Thresh} and d_{Thresh} pair that most correctly groups localizations (maximizes Jaccard index) also generates an image that provides accurate quantification of dimension and density.

Structural geometry does not affect the positions of the optimum threshold pair and Jaccard index peak

Simulations of circular clusters were also examined to test whether differences in structural geometry or dimension can alter the observed effects of photoblinking or threshold selection on quantitative measurements. Figure 4.6 shows the quantitative analyses of one simulation that was generated with the same photoblinking parameters as the FtsZ simulation discussed in Figure 4.2, Figure 4.3, Figure 4.4, and Figure 4.5, but with molecules distributed among several clusters (Figure 4.6A) rather than a single Z-ring.

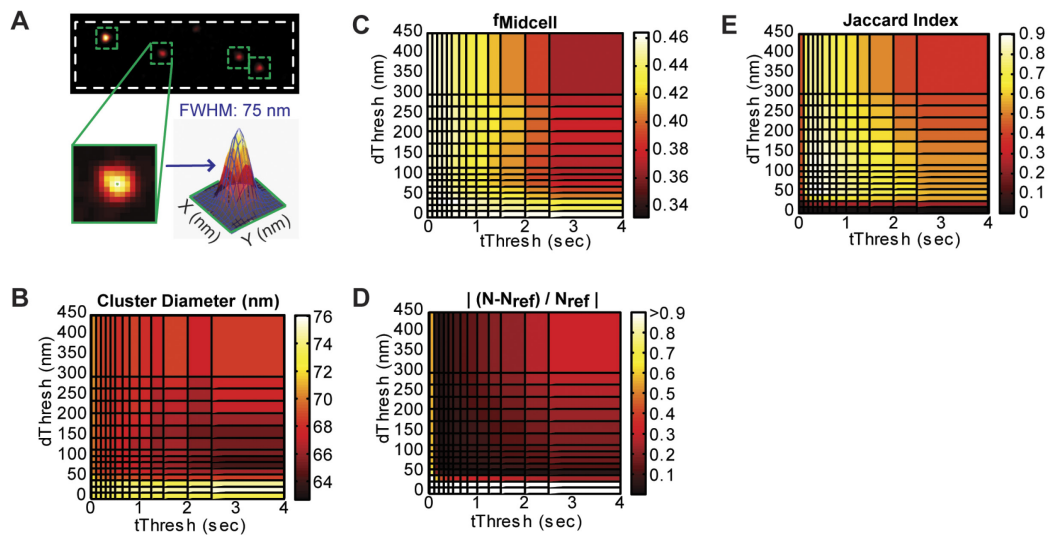


Figure 4.6 Quantitative measurements of a simulated cluster dataset.

(A) Representative cluster diameter measurement for a reference image with no repeat localizations. Each cluster is identified by eye, and then fit to a two-dimensional, symmetrical Gaussian distribution (blue mesh). The cluster diameter is measured as the FWHM, calculated as $2.35 \cdot \sigma$, where σ is the fitted Gaussian standard deviation. The average FWHM of these four clusters is 74 ± 1 nm. (B) Cluster diameter values (average of four clusters) calculated from images generated by applying different threshold pairs to the same simulated dataset. The measured diameters decrease with increasing threshold values, similarly to the Z-ring width measurement. (C) The fraction of molecules located in clusters ($f_{cluster}$) is most similar to that measured in the reference image (0.47) for low values of both d_{Thresh} and t_{Thresh} . (D) As with the Z-ring simulation, fractional difference between each reconstructed image and the number of molecules in the reference image ($N_{ref} = 1212$) is lowest along two intersecting valleys. (E) The Jaccard index peak position for the cluster simulation is similar to that in the Z-ring simulation where identical kinetic parameters were used (Figure 5B). This simulated dataset was generated using the following parameters: $N_{total} = 2000$ (50% in clusters), $\langle \text{molecules/cluster} \rangle = 200$, $\text{FWHM}_{cluster} = 50\text{nm}$, $\sigma = 15\text{nm}$, $\langle n_{blink} \rangle = 2$, $\langle \tau_{off} \rangle = 1$ frame, $\langle \tau_{on} \rangle = 1$ frame, $\langle t_{act}^0 \rangle = 5$ frames (1 frame = 50ms).

Despite the structural difference, the cluster simulation showed a similar trend when different threshold pairs are applied. Figure 4.6B and Figure 4.6C reproduce the general trends that larger threshold values result in smaller dimension measurements and relative density measurements, respectively. The intersection of valleys in the $|(N-N_{ref})/N_{ref}|$ plot (Figure 4.6D) and the Jaccard index peak (Figure 4.6E) coincide with those observed for the Z-ring simulation (Figure 4.3C and Figure 4.5B, respectively). The shared peak positions between simulations with different underlying structure suggests that structural geometry does not affect the position of the optimum thresholds (see Discussion).

Low measurement error is not sufficient to guarantee high Jaccard index

To further illustrate the relationship between Jaccard index and measurement error under a variety of conditions, simulated datasets were generated with different structural geometries, molecule densities, fluorophore blinking properties, and activation rates. For each simulation, the combined measurement error, ϵ_{all} (worst fractional error among the three bulk measurements: N , $f_{midcell}$ or $f_{cluster}$, and ring width or cluster diameter) was measured for each threshold pair. Figure 4.7A shows the relationship between ϵ_{all} generated by the minimum-error threshold pair and the corresponding Jaccard Index achieved by that threshold pair. Across a large range of fluorophore blinking properties and activation rates examined, most Z-ring (blue) and cluster (red) simulations could generate images with low measurement error (< 10%) using at least one threshold pair. However, not all of these images achieved high accuracy at the single molecule level (Jaccard index > 0.8). This result suggests that achieving accurate ensemble measurements is not sufficient to ensure that the corresponding list of molecule positions is reliable.

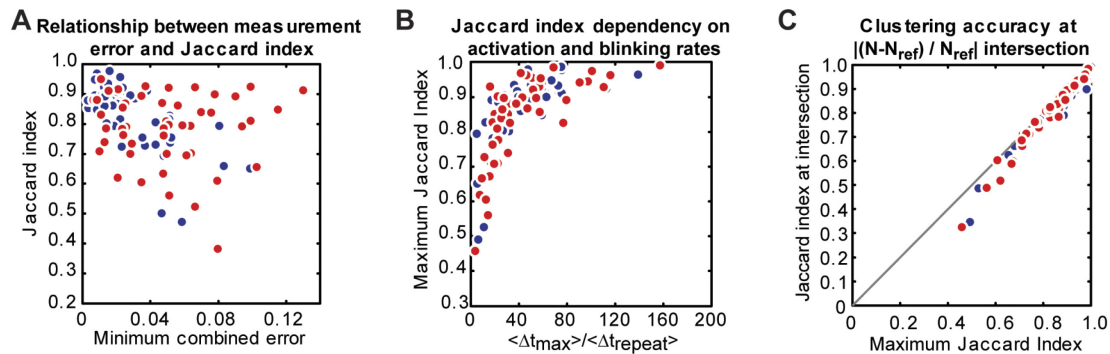


Figure 4.7 Relationship between Jaccard index, measurement error, and activation rate across different simulated datasets.

(A) Minimum combined measurement error, ϵ_{all} , for each dataset plotted against and the corresponding Jaccard index value. ϵ_{all} was defined as the worst fractional measurement error of the three bulk measurements: N , $f_{midcell}$, and ring width when compared to the reference image. Images with low measurement error do not always correlate with high clustering accuracy (Jaccard index), and thus cannot ensure reliable lists of molecule counts and positions. (B) Maximum Jaccard index plotted against the ratio of the average time between localizations in the 255nm x 255nm maximum density region, Δt_{max} , and the average time between repeat localizations of the same molecules, Δt_{repeat} , calculated for each simulated dataset. Simulations with higher ratios of $\Delta t_{max} / \Delta t_{repeat}$ result in higher Jaccard index values. (C) Comparison of maximum Jaccard index with Jaccard index identified at the intersection of the $|(N - N_{ref}) / N_{ref}|$ plot for each simulated dataset. The two values agree well when the maximum Jaccard index is greater than 0.8. In all plots, Z-ring simulations are shown in blue and cluster simulations are shown in red.

Fluorophore blinking kinetics and activation rate determine achievable accuracy in superresolution image reconstruction

As shown by the region where the maximum Jaccard index is < 0.8 in Figure 4.7A, some simulations could not yield high Jaccard indices regardless of threshold selection. This observation indicates that some combinations of fluorophore blinking properties and activation rates do not allow accurate image reconstruction using the clustering algorithm. This most likely occurs when the probability of molecule activation within a diffraction-limited area (255 x 255 nm² for mEos2 in our imaging condition) becomes comparable to the probability that a molecule blinks back on, making it difficult for the clustering algorithm to discriminate a repeat

localization of an activated molecule from the first localization of a new molecule, resulting in separate molecules falsely grouped as single molecules more frequently.

Two experimentally-measurable parameters allow investigation of which combinations of fluorophore blinking rate and activation rate ensure high achievable accuracy in superresolution image reconstruction. The parameter Δt_{max} defines the average time between subsequent localizations of all molecules within the diffraction-limited region of highest molecule density in a superresolution image. Δt_{max} can be easily calculated by dividing the total imaging acquisition time by the number of localizations detected in the maximum density region (see " in the Methods section). Δt_{max} therefore increases when activation is slower given the same fluorophore properties, and serves as a convenient measurement of activation rate. The second parameter, Δt_{repeat} , represents the average time between subsequent localizations of the same molecule, which is determined by fluorophore blinking kinetics, and can be measured from *in vitro* or *in vivo* experiments where single fluorophores are clearly identifiable (Figure 4.8A).

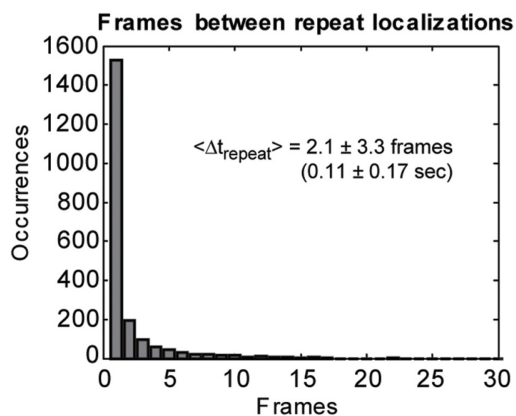


Figure 4.8 Characterization of Δt_{repeat} for mEos2.

Histogram of time (in frames) between sequential molecule localizations, Δt_{repeat} , from 1743 molecules resulting in 3815 localized spots and 2072 intervals between sequential localizations of the same molecules. Data from both *in vitro* samples and fixed cells expressing low levels of mEos2 were combined to generate this histogram. Most repeat localizations occur in consecutive frames (first bin, $\Delta t_{repeat} = 1$), but long dark intervals (> 10 frames) are sometimes observed. The sample mean is $\langle \Delta t_{repeat} \rangle = 2.1 \pm 3.3 \text{ frames}$ (0.11 ± 0.17 seconds).

To explore the relationship between these two parameters and achievable Jaccard index, Δt_{max} and Δt_{repeat} were calculated for the simulations analyzed in Figure 4.7A and plotted the maximum Jaccard index achieved for each simulation against the ratio of $\Delta t_{max}/\Delta t_{repeat}$ (Figure 4.7B). Simulations of both FtsZ (blue) and clusters (red) display a clear increase in maximum Jaccard index with increasing $\Delta t_{max}/\Delta t_{repeat}$, such that accurate clustering (Jaccard index > 0.8) can be achieved when the ratio is kept above 40, regardless of the underlying structure. This observation provides a simple criterion for screening imaging conditions, specifically activation rates, in order to reconstruct a highly accurate superresolution image.

Identifying the optimal threshold pair from an experimental dataset

Although the optimal t_{Thresh} and d_{Thresh} pair can be easily identified from the plot of Jaccard indices at various t_{Thresh} and d_{Thresh} values (Figure 4.5B and Figure 4.6E), the Jaccard Index cannot be calculated for experimental data where the photoblinking behavior of individual molecules is unknown. The overlap of the intersection of valleys in the $|(N-N_{ref})/N_{ref}|$ plot (Figure 4.3C and Figure 4.6D) with the Jaccard peak position (Figure Figure 4.5B and Figure 4.6E), however, may allow the identification of the optimal thresholds using an experimental observable.

To examine the correlation between the intersection of the valleys in the $|(N-N_{ref})/N_{ref}|$ plot and the threshold pair that gives rise to the peak Jaccard index value, the maximum Jaccard index of different simulations was next compared with the Jaccard index achieved using the threshold pair at the intersection of valleys in the $|(N-N_{ref})/N_{ref}|$ plot identified by eye (see Figure 4.9 for examples of intersection identification). Figure 4.7C shows that the maximal Jaccard index and the Jaccard index achieved at the intersection are in excellent agreement when the maximal Jaccard index is greater than 0.8. At these high values, the Jaccard index peaks are in general

broader, such that threshold pairs nearby the peak provide similar clustering accuracy. At low maximum Jaccard indices, the peak becomes sharper, leading to higher variability in achieving the maximum value by visual inspection. These results indicate that near-optimal threshold values can be identified from the intersection of the valleys in the $|(N - N_{ref}) / N_{ref}|$ plot under the ideal experimental conditions described above ($\Delta t_{max} / \Delta t_{repeat} > 40$, Jaccard index > 0.8).

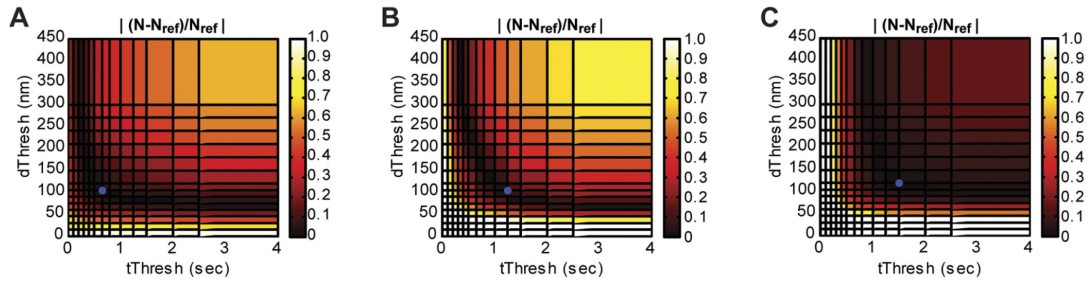


Figure 4.9 Examples of intersection identification in the $|(N - N_{ref}) / N_{ref}|$ plot.

Among the 92 simulations investigated, three categories of plot shapes were observed: symmetric (A), asymmetric (B), and diffuse (C). The optimal threshold pair identified by eye for each example is shown as a blue circle. For symmetric plots, the optimal threshold pair should be selected in the center of the intersection point. For asymmetric plots, the optimal threshold pair should be selected at the inflection point with the longest t_{Thresh} value. The identification of the intersection point in diffuse plots (C) may be difficult because the intersection area is broad. However, these plots result from kinetic parameters that yield very broad and high Jaccard peaks such that a broad range of thresholds around the intersection points yield almost equivalent and sufficient accuracy in resulting images. These representative plots were generated from simulated datasets with the following parameters (N_{total} -midplane % - $\langle n_{blink} \rangle, \langle \tau_{off} \rangle, \langle \tau_{on} \rangle, \langle \tau_{act} \rangle$): 500-30%-1,4,1,1 (A), 1000-30% -2,8,1,1 (B), 500-50%-3,4,1,20 (C) -- all τ values are reported in frames; 1 frame = 50ms).

Generation of the $|(N - N_{ref}) / N_{ref}|$ plot requires knowledge of the true number of molecules, N_{ref} .

This number can be calculated by dividing the total number of localized spots in the unprocessed image ($N_{unprocessed}$) by the average number of localizations per molecule (α) under a given imaging condition (illumination power, exposure time) such that $N_{ref} = N_{unprocessed} / \alpha$

(Lehmann, Rocha et al. 2011; Sengupta, Jovanovic-Talisman et al. 2011; Lando, Endesfelder et al.

2012). An alternative method developed by Annibale *et al.* extracts N_{ref} from fitting a semi-empirical equation to the dependence of N on t_{Thresh} at a fixed d_{Thresh} (Annibale, Vanni et al. 2011).

The parameter α is a bulk fluorophore property that can be obtained experimentally. Here, α_{mEos2} was measured by imaging sparsely distributed, immobilized mEos2 molecules *in vitro* under the same buffer and imaging conditions used for fixed cells. Individual mEos2 molecules could be clearly distinguished as well-separated clusters of localizations (Figure 4.10A). Figure 4.10B shows that the distribution of localizations per molecule approximates an exponential distribution with a fitted mean of 0.9 ± 0.1 . This fitted mean includes the population of molecules that did not last long enough to be detected in one frame, while α reflects the number of localizations per molecule that lasted long enough to be detected in at least one frame. Consequently, the value of α calculated by dividing the total number of localizations by the number of molecules is larger than the fitted mean. Under our imaging condition, $\alpha_{mEos2} = 2.4 \pm 2.8$ (s.d., N= 515) for purified mEos2. Furthermore, fixed *E. coli* cells expressing low levels of untagged mEos2 protein at extremely low activation level resulted in a similar value ($\alpha_{mEos2} = 2.1 \pm 4.3$, N= 1228) (Figure 4.11), suggesting that the blinking properties of mEos2 are similar *in vitro* and in fixed cells under the same buffer conditions. Therefore, the datasets were combined to obtain $\alpha_{mEos2} = 2.2$ (Figure 4.11C), which is within the range of values reported in previous studies under different conditions ($\alpha_{mEos2} = 1-3$) (Lehmann, Rocha et al. 2011; Lando, Endesfelder et al. 2012).

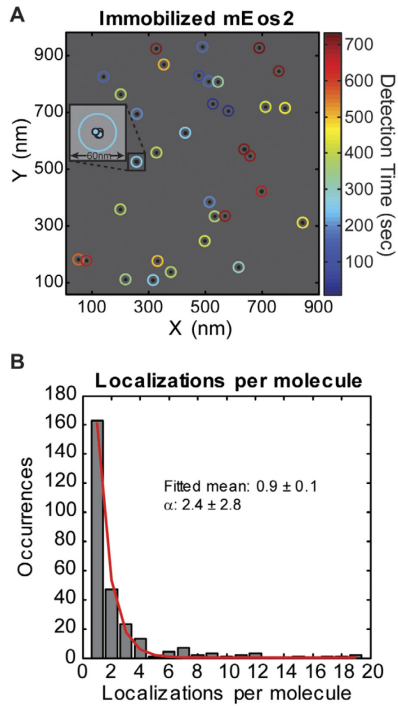


Figure 4.10 *In vitro* characterization of mEos2.

(A) A typical *in vitro* image of purified mEos2 molecules sparsely distributed on a cover glass, acquired using the same PALM imaging condition as the *in vivo* cell sample. All localized positions are indicated by small, filled circles that are colored by detection time. Localizations belonging to the same molecule are enclosed in a larger, open circle, which is colored by the mean detection time of all the enclosed localizations. The inset shows details of a single cluster, which contains four localizations (filled circles with black outlines). (B) Histogram of localizations per molecule from 515 molecules fitted with an exponential distribution (red line), which yielded a mean of 0.9 ± 0.1 localizations per molecule. The value of α (2.4 ± 2.8) represents the mean of observed molecules that lasted at least one frame, and is consequently larger than the fitted mean.

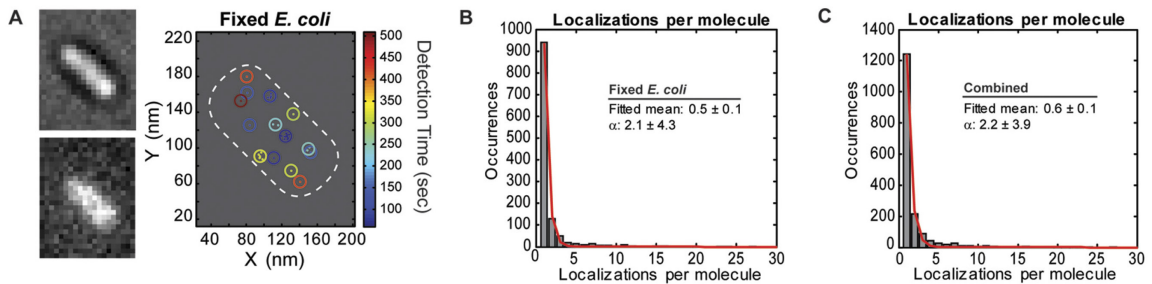


Figure 4.11 Characterization of mEos2 in fixed *E. coli* cells.

(A) Representative images from a single *E. coli* cell expressing mEos2. The brightfield (top left) and green fluorescence (bottom left) images are shown for comparison. The scatter plot (right) shows single molecule localizations (small dots) colored by detection time. Localizations that originated from the same molecule are grouped together (large circles). The cell outline is shown in white. (B) Histogram (gray) of localizations per mEos2 molecule (α) in fixed *E. coli* cells with the corresponding single-exponential fit (red). The fitted mean is 0.5 ± 0.1 localizations per molecule. The ensemble average is 2.1 ± 4.3 (std. dev., $N = 1228$) localizations per molecule. (C) Histogram (gray) and single-exponential fit (red) calculated after combining *in vitro* (B) and *in vivo* (Figure 8B) datasets, which yielded similar values. The fitted mean is 0.6 ± 0.1 localizations per molecule. The ensemble average is 2.2 ± 3.9 (std. dev., $N = 1743$) localizations per molecule.

Application of the optimal threshold pair to experimental data

The experimentally-determined value of α_{mEos2} were used to calculate the true N_{ref} for the experimental dataset described in Figure 4.2 and Figure 4.3, which was collected under the same imaging condition as the sparse mEos2 samples ($N_{ref} = N_{unprocessed} / \alpha_{mEos2} = 1204/2.2 = 547$). Both t_{Thresh} and d_{Thresh} were then varied to generate the plot of $|(N-N_{ref})/N_{ref}|$ (Figure 4.12A), which is qualitatively indistinguishable from that generated from simulated data (Figure 4.3C). From this plot, the intersection of the two valleys ($t_{Thresh} = 0.4$ s and $d_{Thresh} = 60$ nm) was identified as the optimal threshold pair, which was used to generate the optimal superresolution image (Figure 4.12B). The images generated using unoptimized clustering thresholds ($t_{Thresh} = 0.05$ s (1 frame) and $d_{Thresh} = 167$ nm) (Figure 4.1B) and without applying any clustering algorithm (Figure Figure 4.12C) exhibit several bright cytoplasmic clusters, some of which are almost completely removed in the optimal image (white arrows) while a few remain (green arrows). It was previously suspected that FtsZ forms polymeric structures outside the Z-ring (Erickson, Anderson et al. 2010), but because of the blinking-related artifacts described above, it has been difficult to interpret the cytoplasmic clusters observed in superresolution images. The optimal image clearly shows selective removal of blinking-related clusters, increasing our confidence in assigning the remaining cytoplasmic clusters to oligomeric states of FtsZ-mEos2 molecules.

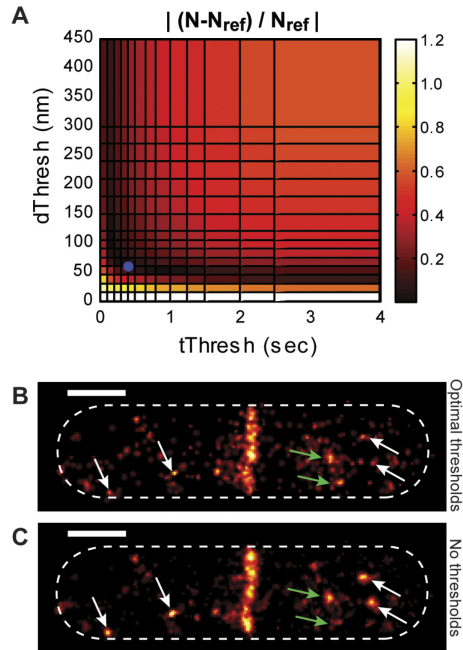


Figure 4.12. Determination and application of optimal threshold pair to an experimental image.

(A) $|(N - N_{ref}) / N_{ref}|$ plot of the experimental dataset used in Figure 1-3. The plot was generated using the N_{ref} number (547) calculated from the measured α value from combined *in vitro* and *in vivo* characterizations of mEos2 (Figure 8 and Figures S4). The optimal threshold pair was identified at 0.4 s and 60 nm (blue circle). (B) and (C) Images constructed using the optimal threshold pair (B) and without any clustering algorithm (C). Clusters that are reduced by the optimized clustering algorithm are indicated by white arrows. Clusters that remain bright in the optimal image, which may represent oligomeric states of FtsZ-mEos2, are indicated by green arrows. Scale bars, 500nm.

This dataset was acquired over 20 minutes, resulting in $\Delta t_{max} = 87$ frames. Using the mEos2 characterization data described above ($\Delta t_{repeat} = 2.1 \pm 3.3$ frames, Figure 4.8A), the ratio $\Delta t_{max} / \Delta t_{repeat}$ can be calculated to be ~ 41 , which is similar to the criterion provided in Figure 4.7B ($\Delta t_{max} / \Delta t_{repeat} > 40$). Consequently, the Z-ring width, $f_{midcell}$, and mean molecule density are within 15% of the expected values (Table 4.1). The Z-ring density distribution from both images was also analyzed using the Poisson goodness-of-fit test. In this case, both the original and the optimal image were well-described by a Poisson distribution ($p_{GOF} = 0.14$ and 0.56, respectively). This result suggests that the blinking behavior of mEos2 does not affect the molecule density

distribution of the Z-ring significantly at the achieved level of sampling ($\langle \text{molecules/pixel} \rangle = 0.5$ in the Z-ring).

Table 4.1 Quantitative measurements made from the optimized experimental image.

	Original image	True value	Optimal image	% difference from true value
Ring width	84nm	84nm*	77nm	8%
$f_{midcell}$	35%	35%*	30%	14%
N	1204	547**	517	5%

*True values for ring width and $f_{midcell}$ are those measured from the original image. **True value for N is the number of molecules in the original image divided by α_{mEos2} ($1204/2.2 = 547$).

Discussion

Selection of localization-based superresolution imaging method

This work has shown that reliable dimension and relative density measurements can be made from superresolution images with multiple fluorophore localizations due to photoblinking. For (d)STORM imaging, it has been shown that multiple localizations of single fluorophores can actually enhance image quality because repetitive sampling of the same molecule averages out the stochasticity in individual localizations, leading to convergence on the true molecule position (van de Linde, Wolter et al. 2010; Dempsey, Vaughan et al. 2011; Jones, Shim et al. 2011). Therefore, if the goal of a superresolution imaging experiment is to visualize overall structural dimensions and obtain relative density measurements, no clustering algorithm should be applied. In this regard, organic dyes that can undergo hundreds of switching cycles, such as those used in (d)STORM, are especially advantageous. The high photon yields of these dyes also improves the accuracy in localizing single molecules, hence enhancing the spatial resolution of the superresolution image (10 - 20 nm (Bates, Huang et al. 2007)).

If the goal of a superresolution experiment is to count the number of molecules accurately in a cellular structure so that stoichiometric information of molecular components can be obtained, photoactivatable fluorophores that are irreversibly activated and exhibit only a few localizations before permanent photobleaching are desirable. Photoactivatable fluorescent proteins such as mEos2 yield only a few localizations per molecule and provide the benefit of stoichiometric labeling via genetic fusion to a protein of interest, improving the accuracy of counting molecules. This work has shown that photoactivatable fluorescent proteins can yield accurate density measurements if activation is kept adequately slow and a clustering algorithm with carefully-selected thresholds is applied. Because conditions and fluorophores for (d)STORM are often optimized to yield long dark times between reversible switching events (large values of Δt_{repeat}) (van de Linde, Wolter et al. 2010; Dempsey, Vaughan et al. 2011), these experiments require prolonged imaging time if the goal is to achieve accurate clustering (see below). Therefore, PALM experiments employing photoactivatable fluorescent proteins such as mEos2, mEos3, and PAmCherry are better suited for molecule-counting than reversibly switchable dyes.

In a live-cell superresolution experiment, an additional consideration for accurate molecule counting is the movement of single molecules. These movements often occur on the millisecond imaging timescale, resulting in single molecules localized at multiple positions throughout a structure. In a similar manner to reversibly switching dyes, this can be beneficial because it allows for faster sampling of the entire structure with fewer fluorophores (Biteen, Thompson et al. 2008). However, molecule movement makes application of the clustering algorithm described above difficult because the optimal distance threshold will depend on the molecule's diffusion rate. Therefore, to obtain accurate molecule counting and absolute density within a structure, fixed-cell PALM experiments with carefully optimized fixation protocols that minimize

structural aberrations are most suitable. Further considerations and limitations in applying the clustering algorithm for fixed-cell PALM experiments are discussed below.

Achievable clustering accuracy is dependent on imaging acquisition condition

The method described here the optimal values of t_{Thresh} and d_{Thresh} from visual inspection of the $|(N-N_{ref})/N_{ref}|$ plot. The optimal values of t_{Thresh} and d_{Thresh} ensure that most repeat localizations are grouped together, minimizing false identification of repeat localizations as separate molecules. However, successful application of the optimized clustering algorithm requires low activation rates, where the probability that a new molecule will be photoactivated nearby an activated molecule before it is photobleached is low. High activation rates result in false grouping of separate molecules.

To minimize false molecule grouping, Δt_{max} needs to be more than 40-fold longer than Δt_{repeat} (Figure 4.7B). For the mEos2 protein characterized in this study, $\Delta t_{repeat} = 2.1$ frames in the (Figure 4.8). Consequently, a minimum Δt_{max} of 84 frames between localizations in the 225 x 225 nm² square of highest density is required. This criterion can be converted into a maximum detection rate of 0.24 molecules/ μm^2 per frame in the maximum density region (1 / 0.05 μm^2 / 84 frames), which also satisfies the conditions previously reported to avoid detection of overlapping fluorescent molecules (< 0.5 molecules/ μm^2 per frame on average (Wolter, Endesfelder et al. 2011)).

Physical meaning of optimal threshold values

Under an imaging condition that allows accurate superresolution reconstruction, the optimal values for t_{Thresh} and d_{Thresh} are related to the mean off time of fluorophore blinking ($\langle \tau_{off} \rangle$) and

the spatial resolution, respectively. Longer $\langle\tau_{off}\rangle$ values require larger values of t_{Thresh} to accommodate the longer dark times between spots so that most repeat localizations of the same molecule are grouped into the same cluster (Figure 4.13). Likewise, the d_{Thresh} value increases with the value of spatial resolution (**Error! Reference source not found.**), which is defined as the FWHM of Gaussian-distributed fluorophore localizations around the central molecule position, and determines the average distance between repeat molecule localizations (see 'Appendix 1'). The optimal d_{Thresh} value is approximately twice the spatial resolution, which is large enough to account for most repeat localizations of the same molecule (Figure 4.15E). The values obtained for the experimental image described above ($t_{Thresh} = 0.4$ s, $d_{Thresh} = 60$ nm) agree with the $\langle\tau_{off}\rangle$ timescale of mEos2 blinking kinetics observed in our study (0.10 s, Figure 4.15B) and previous studies (0.1 - 0.4 s)(Annibale, Vanni et al. 2011), as well as the typical spatial resolution of mEos2 molecules in our setup (42m; Figure 4.15D). Although this general correlation (Figure 4.13 and Figure 4.14) could also be used to estimate optimal threshold values, substantial variations in corresponding optimal threshold values exist due to other fluorophore photoproperties or structural parameters. Generation of the $|(N-N_{ref})/N_{ref}|$ takes all of these factors into account, while requiring similar effort in fluorophore characterization.

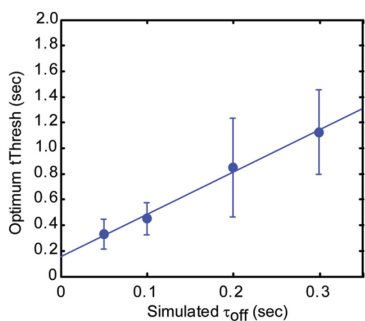


Figure 4.13 Optimal t_{Thresh} values are related to the mean off time. Datasets from both Z-ring and cluster simulations were grouped by simulated fluorophore off-time, τ_{off} , then t_{Thresh} values at the Jaccard index peak of each simulation were averaged (blue circles; error bars represent standard deviation) and plotted against the fluorophore off-time. The two parameters show a clear correlation, suggesting that the optimum t_{Thresh} value is largely determined by the mean fluorophore off time (linear fit: $Y = 3.3X + 0.14$, $R^2 = 0.99$). However, the large variation at some τ_{off} values suggest that other experimental factors affect the optimal t_{Thresh} value. A list of simulations used in this analysis can be found in Table S1 and S2.

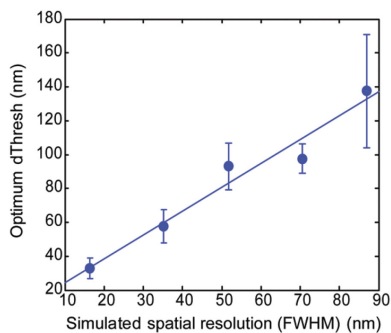


Figure 4.14 Optimal d_{Thresh} values are related to the spatial resolution. Datasets from Z-ring and cluster simulations were grouped by simulated spatial resolution (FWHM), then the d_{Thresh} values at the Jaccard index peak of each simulation were averaged (blue circles; error bars represent standard deviation) and plotted against the simulated spatial resolution. Spatial resolution was calculated as 2.35σ , where σ is the Gaussian standard deviation used to scatter localizations around the central molecule positions (see Methods and Text S1). The two parameters show a clear correlation, indicating that larger spatial resolutions result in larger values for optimum d_{Thresh} (linear fit: $Y = 1.4X + 10.2$, $R^2 = 0.96$). This plot was generated using the same datasets analyzed in Figure S5 (see Table S1 and S2 for parameter list).

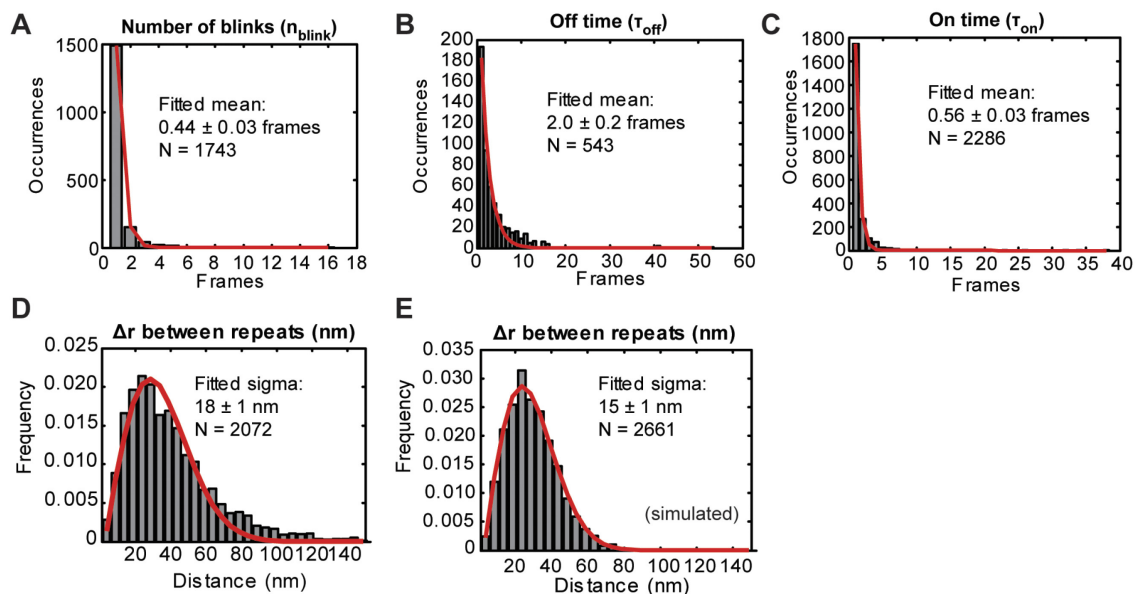


Figure 4.15 Validation of kinetic and spatial simulation parameters.

Combined datasets from both *in vitro* and *in vivo* characterizations of mEos2 were used to generate histograms of n_{blink} (A), τ_{off} (B), and τ_{on} (C), which are all described well by single-exponential distributions, validating the simple kinetic scheme used to simulate fluorophore dynamics in this work. Red curves indicate single-exponential fits that yielded mean values of: $\langle n_{blink} \rangle = 0.44 \pm 0.03$ (A), $\langle \tau_{off} \rangle = 2.0 \pm 0.2$ frames (B), and $\langle \tau_{on} \rangle = 0.56 \pm 0.03$ frames (C). (D-E) Histograms of the pair-wise distances between repeat localizations of the same molecule for experimental (D) and simulated (E) datasets. The histograms were fit to Equation 2 from Text S1 ($p(\Delta r) = (r/2\sigma^2) \cdot \exp(-r^2/4\sigma^2)$; red lines), yielding standard deviation, σ , of 18 ± 1 nm (D) and 15 ± 1 nm (E), respectively. The experimental dataset is the same combined dataset characterized in (A-C) above. The simulated dataset had a nominal σ of 15nm, and is the same dataset analyzed in Figures 2-5 ($N_{total} = 2000$ (50% midplane), $\sigma = 15$ nm, $\langle n_{blink} \rangle = 2$, $\langle \tau_{off} \rangle = 1$ frame, $\langle \tau_{on} \rangle = 1$ frame, $\langle \tau_{act}^0 \rangle = 5$ frames (1 frame = 50ms)).

Fluorophore characterization

Two fluorophore properties need to be determined to implement the method described. First, the average time between repeat molecule localizations, Δt_{repeat} , should be compared with the activation rate to identify imaging conditions that are suitable for accurate superresolution image reconstruction as described above. Second, the average number of observations per molecule, α , is required to generate the $|(N-N_{ref})/N_{ref}|$ plot. Both of these parameters should be determined using the same exposure time and excitation intensity as those used for the superresolution imaging. This can be done with either purified fluorophore or, ideally, with a fixed biological sample of low labeling density that is activated extremely slowly. It is also important to characterize a fluorophore under the same buffer conditions used for superresolution imaging because blinking kinetics are highly dependent on a fluorophore's chemical environment (Endesfelder, Malkusch et al. 2011). The conditions inside fixed cells should be equilibrated with external buffer conditions, but this is not the case for live cells. Since movement can complicate fluorophore characterization in live cells, fixed cells are ideal for the purposes of accurate molecule counting and density measurements.

The kinetic scheme used to describe the blinking behavior of mEos2 in this work is relatively simple and has been previously shown to sufficiently describe mEos2 (Annibale, Vanni et al. 2011). Although more complex schemes, in which multiple pathways lead to the observed dark or fluorescent states (Habuchi, Ando et al. 2005; McAnaney, Zeng et al. 2005; Yeow, Melnikov et al. 2006; Annibale, Scarselli et al. 2010; David, Dedecker et al. 2012), may also be applicable to mEos2 and other photoactivable fluorophores, this work has shown that the distributions of τ_{on} , τ_{off} , and n_{blink} observed from individual mEos2 molecules can be approximated well by single exponential distributions (Figure 4.15A-C).

Comparison with other superresolution processing algorithms

A few recent methods have addressed some of the effects of photoblinking on superresolution images. The method developed by Annibale *et al.* identifies the correct number of molecules (N_{ref}) in a superresolution image by fitting the dependence of N on t_{Thresh} to a semi-empirical function (Annibale, Vanni et al. 2011). In addition to providing an unambiguous way to determine the true N_{ref} in a heterogeneous image, the method presented here provides optimal t_{Thresh} and d_{Thresh} values to generate a reliable image that can be quantified in many different ways, and identified a quantitative criterion ($\Delta t_{max}/\Delta t_{repeat} > 40$) under which optimal image reconstruction is possible.

Other studies have applied pair correlation analyses to images of membrane clusters to extract mean density and cluster size (Sengupta, Jovanovic-Talisman et al. 2011; Veatch, Machta et al. 2012). By analyzing correlation functions of distances between detected spots, these studies have elegantly determined the relative contribution of blinking and true molecular interactions to the observed clusters in their superresolution images. Because the pair correlation analysis does not require classification of each localized spot, it can accommodate faster activation rates than the method described here. However, features of irregular shape and heterogeneous density may not be sufficiently characterized by the pair correlation analysis, which summarizes an entire image into a few parameters.

The optimized clustering algorithm described in this work complements these methods by generating a full superresolution image and accurate list of molecule positions that provide additional qualitative and quantitative information that cannot be described by one or a few global parameters. This study has examined a few quantitative analyses that can be performed

(dimension, mean density, relative density, and density distribution analysis), but each biological system may be characterized by unique quantitative features that can be measured from the images and list of positions our method provides. Additionally, because the method presented here is a simple modification to the superresolution image analysis algorithm first developed for PALM (Betzig, Patterson et al. 2006), it can be conveniently implemented in commonly used algorithms.

Methods

Simulation of FtsZ structures

Based on previous experimental PALM images (Fu, Huang et al. 2010), FtsZ molecules were simulated in the cell as two populations: midplane and cytoplasmic. Positions for cytoplasmic molecules were sampled from a uniform distribution across the entire cell area (1 μm x 3 μm rectangle). Positions for midplane molecules were sampled from a uniform distribution in a 110 nm x 1 μm rectangle at the midcell. Figure 4.16A shows a representative simulation of distributed midplane (red) and cytoplasmic (blue) molecules. Simulations presented in this work were comprised of 1000, 2000, or 5000, total molecules that were distributed with 30%, 50%, or 75% in the midplane population.

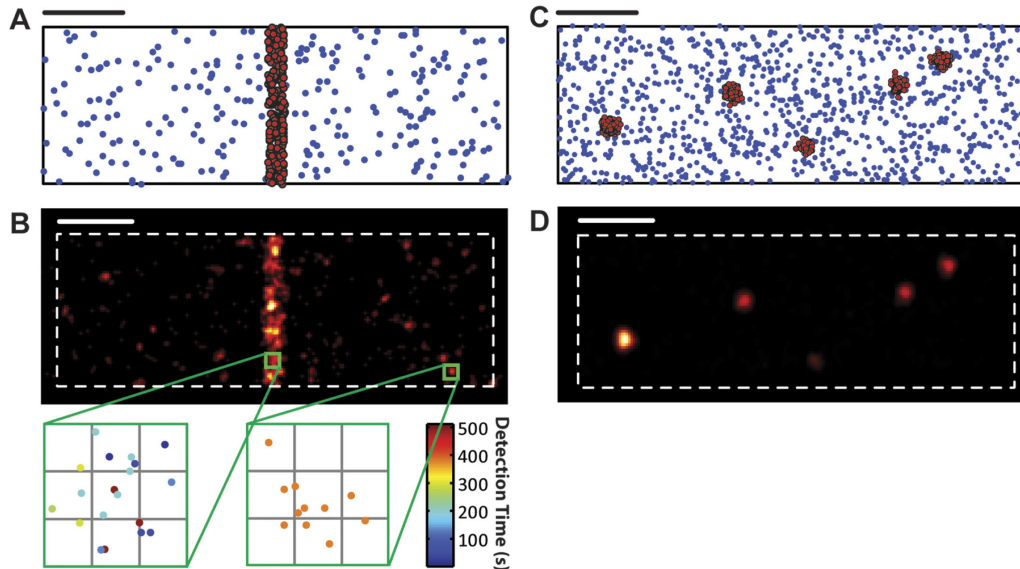


Figure 4.16 Representative simulations of superresolution images.

(A) Representative simulation of FtsZ locations within an *E. coli* cell. The total number of molecules, N , is 500. Molecules are divided into 50% midplane (red) and 50% cytoplasmic (blue). (B) Superresolution image generated from the data in (A) after simulating the following kinetic parameters: $\langle n_{blink} \rangle = 3$, $\langle \tau_{off} \rangle = 4$ frames, $\langle \tau_{on} \rangle = 1$ frame, $\langle \tau_{act}^0 \rangle = 7$ frames, and applying the same clustering algorithm used to generate Figure 1B: spots within 167nm (1 camera pixel) and 50ms (1 frame) of each other were grouped together and plotted once. The simulated image reproduces the time-correlated clusters observed in the experimental image (Figure 1B). (C) Representative simulation of clusters within an *E. coli* cell. The total number of molecules, N , is 2000. Molecules are divided into 50% clustered (red) and 50% cytoplasmic (blue) molecules, with the cluster diameter designated as 50nm FWHM. The number of molecules per cluster was sampled from an exponential distribution with $\langle \text{molecules/cluster} \rangle = 200$. (D) Superresolution image generated from the data in (C) after simulating the following kinetic parameters: $\langle n_{blink} \rangle = 2$, $\langle \tau_{off} \rangle = 1$ frames, $\langle \tau_{on} \rangle = 1$ frame, $\langle \tau_{act}^0 \rangle = 5$ frames, but plotting only the first localization of each molecule. Scale bars, 500nm. Grid size, 30nm.

Simulation of circular clusters

Each simulation of circular clusters required designation of the following parameters: total number of molecules in a cell, fraction of molecules within clusters, mean number of molecules per cluster, and cluster FWHM. The positions of molecules that were not within clusters (cytoplasmic molecules) were sampled in the same manner as described for the cytoplasmic molecules in the FtsZ simulation.

The integer number of clusters in a given simulation was calculated by dividing the total number of molecules in all clusters by the mean number of molecules per cluster. Then, the number of molecules in each cluster was sampled from an exponential distribution. The molecules within each cluster were scattered according to a symmetrical, two-dimensional Gaussian distribution with the designated FWHM, and the center of each cluster was distributed uniformly throughout the cell. Figure 4.16C shows a representative simulation of distributed clustered (red) and cytoplasmic (blue) molecules.

Simulation of fluorophore blinking kinetics

The kinetics of fluorophore activation and blinking were simulated by varying the following parameters:

1. Activation rate (k_1): rate at which new molecules are activated; inversely proportional to the number of unactivated molecules remaining
2. Blink off rate (k_2): rate at which a molecule is reversibly converted to the transient 'off' state
3. Blink on rate (k_3): rate at which a molecule is turned on from the transient 'off' state
4. Bleaching rate (k_4): rate at which a molecule is irreversibly turned off by photobleaching

Figure 4.1A shows a diagram of this simple kinetic scheme. Experimentally, k_1 is controlled by the intensity of the activation laser and k_4 is controlled by the intensity of the excitation laser.

The kinetic parameters were simulated using MATLAB[®] via Monte-Carlo simulations of fluorophore dynamics where exponential probability distributions were assigned for each of the following parameters:

1. Lag time between molecule activations (τ_{act}) was sampled from an exponential probability distribution with expected value of $\tau_{act}^0(N_{initial}/N_{remaining})$, which increases as the number of remaining molecules ($N_{remaining}$) that have not been activated decreases. τ_{act}^0 is the expected lag time at the initial number of molecules ($N_{initial}$).
2. The duration of each blink (τ_{on}).
3. The duration of dark times between blinks (τ_{off}).
4. Number of blinks per molecule (n_{blink}).

All times were rounded to the nearest integer number of frames (presented figures plot time in seconds using a 50 ms exposure time). Note that the kinetic parameters used in these simulations reflect observed fluorescence time traces that are highly dependent on experimental conditions such as excitation/activation light intensity, pixel size, background noise, frame rate, spot detection algorithm, and spot fitting algorithm. This scheme was validated by verifying that the observed time traces of individual mEos2 molecules under the experimental conditions were well-described by exponential distributions of τ_{on} , τ_{off} , and n_{blink} (Figure 4.11A-C).

Molecules were iteratively activated with lag times sampled from the updated τ_{act} distribution. Once activated, the number of blinks for a given molecule was sampled from the n_{blink} distribution. For each blink event, the on-time was sampled from the τ_{on} distribution and the time until the next blink was sampled from the τ_{off} distribution. The lag time (τ_{act}) until the next molecule activation was calculated from the start of the previously activated molecule such that blinking events from multiple molecules could overlap in time.

For low expected values, sampling from an exponential distribution often resulted in values less than one frame. A value of $n_{blink} < 0.5$ (rounded to $n_{blink} = 0$) means that the molecule was

activated but never 'observed' in the simulation due to fast photobleaching. This was also true for low values of mean on-time (τ_{on}), which resulted in some blinks not being recorded. These properties mimic experimental conditions and highlight the fact that not every activated fluorophore or blinking event will be visualized.

Once the blinking time trace was established for each molecule, its multiple localizations were scattered around the original molecule position according to a two-dimensional normal distribution with a standard deviation, σ , between 7 - 37nm. For the simulation described in Figure 4.2, Figure 4.3, Figure 4.4, and Figure 4.5, $\sigma = 15\text{nm}$, which results in a FWHM spatial resolution of 35nm. The position distributions generated by the simulation were similar to those observed for experimental mEos2 localizations by plotting the histograms of distances between repeat localizations of the same molecule that result from the simulation (Figure 4.15E) and from experimental data (Figure 4.15D). The shape and peak position of both distributions are similar, suggesting that the simulation with $\sigma = 15\text{nm}$ approximates our experimental data.

Superresolution image reconstruction with localization-based PSFs

Superresolution images of both simulated and experimental data were generated in MATLAB[®] with a pixel size of 15 nm. Each localized spot was plotted as a symmetrical 2D Gaussian distribution with total intensity equal to 1 and σ equal to the experimental or simulated localization precision. For simulated data, the localization precision was equivalent to the standard deviation, σ , used to simulate the scatter of localizations around the molecule position . For experimental data, only molecules with localization precisions smaller than 20 nm were

plotted. Superresolution images were pseudocolored using the 'Red Hot' lookup table in ImageJ software (NIH).

Superresolution molecule density measurement

For density measurements, superresolution molecule density images of both simulated and experimental data were generated in MATLAB® with a pixel size of 15 nm. The intensity of each pixel in the density image represents the number of molecules detected within the pixel's boundaries, and hence represents a two-dimensional histogram of molecule counts. For experimental data, only molecules with localization precisions smaller than 20 nm were included.

Boundaries of the Z-ring or cluster regions of each density image were identified as polygons by eye. Relative density within the Z-ring ($f_{midcell}$) was calculated by dividing the summed intensity within the Z-ring region by the total intensity of the density image (total number of localized spots). Similarly, relative density within clusters ($f_{cluster}$) was calculated by dividing the summed intensity within all clusters by the total intensity of the density image. Z-ring density histograms were generated by binning pixels within the Z-ring region by intensity.

Calculation of maximal activation rate

The average time between molecule activations, Δt_{max} , was calculated from the time intervals between localizations within the 225nm x 225nm square of maximum density, which was identified by applying a mean filter to the superresolution density image (see above) using the 'nlfilter' function in MATLAB with a 17pixel x 17pixel sliding window (15 nm pixel size). The maximum density square is centered at the maximum intensity pixel in the filtered image. This calculation is identical for both simulated and experimental data.

Clustering algorithm

Both simulated and experimental time traces were clustered in MATLAB® using two thresholds: any spot that occurred within time, t_{Thresh} , and distance, d_{Thresh} , of a previous spot was grouped into the same cluster as that previous spot (see Figure 4.17 for flowchart). The resulting cluster was assigned a spatial position equal to the centroid position of all the spots included in the cluster.

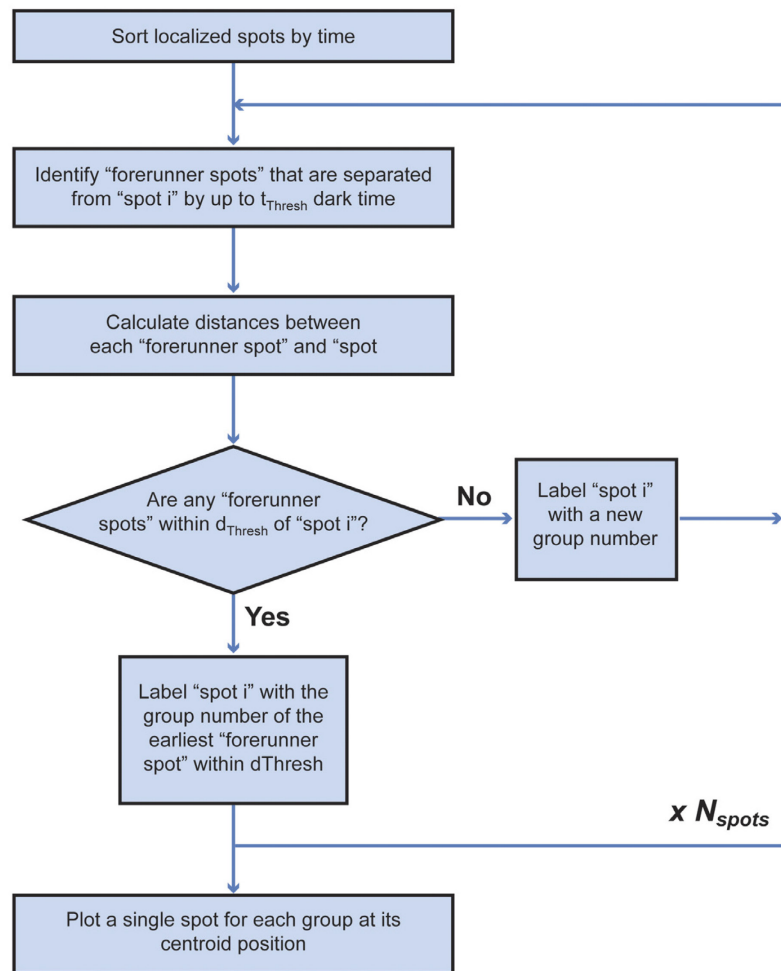


Figure 4.17 Schematic of spot clustering algorithm.

After spot identification and localization, the set of spots is processed iteratively such that any previous spot ("forerunner spot") that occurred within t_{Thresh} and d_{Thresh} of a given spot ("spot i ") are grouped together. Each group is then plotted only once in the final superresolution image at the calculated centroid position.

Jaccard index of cluster accuracy

The Jaccard index (Gower and Legendre 1986; Jackson, Somers et al. 1989) of clustering accuracy was calculated for each clustering result as $TP / (TP + FP + FN)$. TP is the number of pairs of localizations that came from the same molecule, and were grouped into the same cluster; FP is the number of pairs of localizations that did not come from the same molecule, but were grouped into the same cluster; and FN is the number of pairs of localizations that came from the same molecule, but were grouped into different clusters. The Jaccard index varies from 0 to 1, where a value of 1 represents perfect clustering.

Preparation and purification of mEos2

The *mEos2* gene was amplified using primers AATTGTCGACAATGAGTGCGATTAAGCCAGACA and TTAAGCGGCCGCTTATCGTCTGGCATTGTCAG. The PCR product was restricted using *Sa*I and *Not*I restriction enzymes (New England Biolabs), and cloned into the same sites of plasmid pT7HMT (Geisbrecht, Bouyain et al.) . The inserted sequence was confirmed via sequencing and the resulting plasmid was transformed into BL21-Gold(DE3) cells (Stratagene). To purify his-mEos2, cells were cultured overnight at 37°C in LB (Luria Broth) media. The culture was then diluted 1:200 in 200 mL LB media, grown at 37°C to an OD₆₀₀ of 0.8, then induced for 2 hours with 0.5 mM IPTG (Isopropyl β-D-1-thiogalactopyranoside). Cells were collected at 4100 rpm for 20 min in a Sorvall Legend RT bench top centrifuge at 4°C. Cells were lysed using sonication and repeated freeze thaw cycles and subsequently purified on Ni-NTA beads (Invitrogen) at 4°C according to the ProBond™ native protocol. Protein was buffer-exchanged and concentrated from elution buffer to pH 7.4 phosphate buffer saline using a Vivaspin 500 concentrator (GE Healthcare) with a 5,000 MW cutoff. Purified his-mEos2 was checked for purity by running Mini-PROTEAN TGX Gels (BIO-RAD), and concentration was determined in a Nanodrop

spectrophotometer using absorption coefficient of $5,600\text{M}^{-1}\text{cm}^{-1}$ at 280 nm (McKinney, Murphy et al. 2009). His-tagged mEos2 was diluted 1:10,000 from a stock concentration of $13.5\ \mu\text{M}$, then frozen in an ethanol dry-ice bath and stored at -80°C in $2\ \mu\text{L}$ aliquots.

***In vitro* sample preparation**

A 12% NiCl_2 aqueous solution was prepared and filtered to sterilize and remove aggregates. A coverslip was secured via Scotch tape (3M) to a Mini Mouse II (Denville scientific) centrifuge with the 1.5 mL tube attachment. While spinning at 6000 RPM, $50\ \mu\text{L}$ of the NiCl_2 solution was slowly pipetted to the center of the spinning coverslip through a $\sim 1\ \text{cm}$ hole in the plastic cover. The spin coating was visually inspected for evenness. Next, $0.5\ \mu\text{L}$ of purified his-mEos2 sample ($1.35\ \text{nM}$) was pipetted to the center of the NiCl_2 -coated coverslip without spinning. Sample was allowed to dry, then topped with an agarose gel pad to mimic the PALM image acquisition setup described previously (Fu, Huang et al. 2010).

***E. coli* sample preparation and fixation**

E. coli B/rA cells containing plasmid pCA24N-FtsZ-mEos2 (Fu, Huang et al. 2010) were grown in M9 media supplemented with glucose at 25°C to an OD_{600} of 0.2, then induced with $20\ \mu\text{M}$ IPTG for 2hrs. Cells were then collected via centrifugation, resuspended in fresh M9 media, grown at 25°C for 90 minutes, and fixed with 4% formaldehyde at 25°C for 40min. The fixed *E. coli* cells were mixed with 50 nm gold fiducial beads (Microspheres-Nanospheres, Mahopac, NY), then sandwiched between an agarose gel pad and a cleaned coverslip as described previously (Fu, Huang et al. 2010).

PALM Imaging conditions

Images were acquired using an Olympus IX-71 inverted microscope, equipped with a 60x, 1.45 NA TIRFM objective. A 405nm laser (CUBE™, Coherent, Santa Clara, CA) was used to activate mEos2. The green and red fluorescence of mEos2 was excited via epi-illumination with 488nm and 561nm solid state lasers (Sapphire, Coherent, Santa Clara, CA) and emission was collected on an EMCCD camera (iXon DU897E, Andor Technology, Belfast, Northern Ireland) after passing through a dual-band emission filter (510/19 and 620/20, Chroma Technology, Rockingham, VT).

During the imaging sequence, the sample was illuminated continuously with both 405nm and 561nm lasers. The exposure time was 50 ms per frame (20 Hz) with a 100pixel × 100pixel imaging area. The intensity of the 405nm activation laser was increased stepwise as the number of unactivated mEos2 molecules decreased during data acquisition.

Molecule detection in experimental data

Molecules were detected and localized as described previously (Fu, Huang et al. 2010). Briefly, intensity and area thresholds were used to identify potential fluorescence spots, which were fit to a symmetric, two-dimensional Gaussian function using a nonlinear least squares algorithm in MATLAB. Localization precision was calculated from the photon counts according to the theoretical formula (Thompson, Larson et al.). Sample drift was calibrated by applying the frame-to-frame displacement of 50nm gold beads, which were localized in the same manner as single molecules of mEos2.

Appendix 1: Calculation of Spatial Resolution

The spatial resolution of PALM or STORM experiments is determined by several factors. The theoretical upper bound of spatial resolution is related to the localization precision (σ), which primarily depends on the number of photons detected per localized spot (Lehmann, Rocha et al. 2011):

$$\sigma^2 = \frac{s^2 + a^2/12}{N} + \frac{8\pi s^4 b^2}{a^2 N^2} \quad (1)$$

where s is the standard deviation of the Gaussian point spread function, a is the image pixel size, N is the number of photons detected from the molecule, and b is the background noise. The upper bound of spatial resolution is then the FWHM (full width at half maximum) of a Gaussian distribution with localization precision, σ , as the standard deviation.

In practice, the experimental spatial resolution is often defined as the positional variability in repeat localizations of the same molecule, which can deviate from the theoretical localization precision value due to thermal fluctuations and nonidealities in the detection system. For molecules that are localized many times (such as STORM dyes), this positional variability can be measured by first identifying the mean position of each molecule, then superimposing localizations of many molecules such that the mean positions of every molecule are aligned. The FWHM of the resulting Gaussian distribution of positions is the maximum achievable spatial resolution (Coltharp and Xiao 2012), given sufficient sampling (see below). When each molecule is only localized a few times (as with PALM fluorophores), however, the mean position of each molecule is less well-defined and this method is not as reliable.

For PALM fluorophores, measurement of positional variability can be made from the distribution of pair-wise displacement between repeat localizations of the same molecule. This measurement is more applicable for fluorophores that are only localized a few times because the results from many molecules can be combined into a single distribution without alignment. The distribution of distances between two localized spots is given by the following equation (Stirling Churchman, Flyvbjerg et al. 2006):

$$p(r) = \left(\frac{r}{\sigma_1^2 + \sigma_2^2} \right) e^{\left(-\frac{\mu^2 + r^2}{2(\sigma_1^2 + \sigma_2^2)} \right)} I_0 \left(\frac{r\mu}{\sigma_1^2 + \sigma_2^2} \right) \quad (2)$$

where $p(r)$ is probability of observing displacement, r , in two dimensions; σ_1 is the standard deviation in localized positions for spot 1; σ_2 is standard deviation in localized positions for spot 2; μ is the true distance between the two spots; and I_0 is the modified Bessel function of integer order zero. For calculation of spatial resolution, the true distance between repeat localizations of the same molecule is zero ($\mu = 0$) and the standard deviations in localized positions for both spots are identical ($\sigma_1 = \sigma_2 = \sigma$), so Equation 2 simplifies to:

$$p(r) = \left(\frac{r}{2\sigma^2} e^{\frac{-r^2}{4\sigma^2}} \right) \quad (3)$$

where $p(r)$ is probability of observing displacement, r , between repeat localizations. The achieved spatial resolution is then the FWHM calculated from the measured σ (FWHM = 2.35σ). Equation 3 was used to fit the distribution of distances between repeat localizations for both experimental (Figure 4.15D) and simulated (Figure 4.15E) datasets to extract the spatial resolution. For the simulated dataset, the fitted spatial resolution ($\sigma = 15 \pm 1\text{nm}$; FWHM = $35 \pm 2\text{nm}$) was in excellent agreement with the nominal spatial resolution ($\sigma = 15\text{nm}$; FWHM = 35nm).

The measurements of spatial resolution provided above all reflect the precision of identifying a single molecule's location. It is important to note that the spatial resolution needed to resolve a given structural feature is also related to the sampling of the structure by the Nyquist-Shannon criterion, which states that a structure needs to be sampled at greater than twice the desired resolution (Shannon 1949; Biteen and Moerner 2010; Coltharp, Yang et al. 2014). For example, to achieve a precision-dictated FWHM resolution of 35nm, a structure needs to be sampled once every 17.5 nm on average. Thus, a 350 x 350 nm² structure would require 400 molecules to achieve 35nm resolution, and detection of only 100 molecules would yield 70nm resolution.

References

- Aarsman, M. E., A. Piette, et al. (2005). "Maturation of the Escherichia coli divisome occurs in two steps." *Mol Microbiol* **55**(6): 1631-1645.
- Adams, D. W. and J. Errington (2009). "Bacterial cell division: assembly, maintenance and disassembly of the Z ring." *Nat Rev Microbiol* **7**(9): 642-653.
- Addinall, S. G. and J. Lutkenhaus (1996). "FtsZ-spirals and -arcs determine the shape of the invaginating septa in some mutants of Escherichia coli." *Mol Microbiol* **22**(2): 231-237.
- Allard, J. F. and E. N. Cytrynbaum (2009). "Force generation by a dynamic Z-ring in Escherichia coli cell division." *Proc Natl Acad Sci U S A* **106**(1): 145-150.
- Anderson, D. E., F. J. Gueiros-Filho, et al. (2004). "Assembly Dynamics of FtsZ Rings in Bacillus subtilis and Escherichia coli and Effects of FtsZ-Regulating Proteins." *J Bacteriol* **186**(17): 5775-5781.
- Ando, R., H. Mizuno, et al. (2004). "Regulated Fast Nucleocytoplasmic Shuttling Observed by Reversible Protein Highlighting." *Science* **306**(5700): 1370-1373.
- Annibale, P., M. Scarselli, et al. (2012). "Identification of the factors affecting co-localization precision for quantitative multicolor localization microscopy." *Optical Nanoscopy* **1**(1): 9.
- Annibale, P., M. Scarselli, et al. (2010). "Photoactivatable Fluorescent Protein mEos2 Displays Repeated Photoactivation after a Long-Lived Dark State in the Red Photoconverted Form." *Journal of Physical Chemistry Letters* **1**(9): 1506-1510.
- Annibale, P., S. Vanni, et al. (2011). "Identification of clustering artifacts in photoactivated localization microscopy." *Nat Methods* **8**(7): 527-528.
- Annibale, P., S. Vanni, et al. (2011). "Quantitative photo activated localization microscopy: unraveling the effects of photoblinking." *PLoS One* **6**(7): e22678.
- Arends, S. J., K. Williams, et al. (2010). "Discovery and characterization of three new Escherichia coli septal ring proteins that contain a SPOR domain: DamX, DedD, and RlpA." *J Bacteriol* **192**(1): 242-255.
- Aussel, L., F. X. Barre, et al. (2002). "FtsK Is a DNA motor protein that activates chromosome dimer resolution by switching the catalytic state of the XerC and XerD recombinases." *Cell* **108**(2): 195-205.
- Baba, T., T. Ara, et al. (2006). Construction of Escherichia coli K-12 in-frame, single-gene knockout mutants: the Keio collection.
- Baddeley, D., M. B. Cannell, et al. (2010). "Visualization of Localization Microscopy Data." *Microscopy and Microanalysis* **16**(01): 64-72.
- Baddeley, D., M. B. Cannell, et al. (2010). "Visualization of localization microscopy data." *Microsc Microanal* **16**(1): 64-72.
- Bailey, M. W., P. Bisicchia, et al. (2014). "Evidence for Divisome Localization Mechanisms Independent of the Min System and SlmA in *Escherichia coli*." *PLoS Genet* **10**(8): e1004504.
- Bakshi, S., A. Siryaporn, et al. (2012). "Superresolution imaging of ribosomes and RNA polymerase in live Escherichia coli cells." *Molecular Microbiology* **85**(1): 21-38.
- Bar-On, D., S. Wolter, et al. (2012). "Super-resolution imaging reveals the internal architecture of nano-sized syntaxin clusters." *Journal of Biological Chemistry*.
- Bates, M., B. Huang, et al. (2007). "Multicolor super-resolution imaging with photo-switchable fluorescent probes." *Science* **317**(5845): 1749-1753.

- Bates, M., B. Huang, et al. (2007). "Multicolor Super-Resolution Imaging with Photo-Switchable Fluorescent Probes." *Science* **317**(5845): 1749-1753.
- Begg, K. J., A. Takasuga, et al. (1990). "The balance between different peptidoglycan precursors determines whether Escherichia coli cells will elongate or divide." *J Bacteriol* **172**(12): 6697-6703.
- Beheiry, M. E. and M. Dahan (2013). "ViSP: representing single-particle localizations in three dimensions." *Nat Meth* **10**(8): 689-690.
- Betzig, E., G. H. Patterson, et al. (2006). "Imaging intracellular fluorescent proteins at nanometer resolution." *Science* **313**(5793): 1642-1645.
- Bi, E. and J. Lutkenhaus (1990). "Analysis of ftsZ mutations that confer resistance to the cell division inhibitor Sula (SfiA)." *J Bacteriol* **172**(10): 5602-5609.
- Bielopolski, N., A. D. Lam, et al. (2014). "Differential interaction of tomosyn with syntaxin and SNAP25 depends on domains in the WD40 beta-propeller core and determines its inhibitory activity." *J Biol Chem*.
- Bigot, S., O. A. Saleh, et al. (2005). "KOPS: DNA motifs that control E. coli chromosome segregation by orienting the FtsK translocase." *EMBO J* **24**(21): 3770-3780.
- Biteen, J. S., E. D. Goley, et al. (2012). "Three-Dimensional Super-Resolution Imaging of the Midplane Protein FtsZ in Live Caulobacter crescentus Cells Using Astigmatism." *ChemPhysChem* **13**(4): 1007-1012.
- Biteen, J. S., E. D. Goley, et al. (2012). "Three-dimensional super-resolution imaging of the midplane protein FtsZ in live Caulobacter crescentus cells using astigmatism." *Chemphyschem* **13**(4): 1007-1012.
- Biteen, J. S. and W. E. Moerner (2010). "Single-Molecule and Superresolution Imaging in Live Bacteria Cells." *Cold Spring Harbor Perspectives in Biology* **2**(3).
- Biteen, J. S., M. A. Thompson, et al. (2008). "Super-resolution imaging in live Caulobacter crescentus cells using photoswitchable EYFP." *Nat Meth* **5**(11): 947-949.
- Bolte, S. and F. P. Cordelieres (2006). "A guided tour into subcellular colocalization analysis in light microscopy." *J Microsc* **224**(Pt 3): 213-232.
- Bottomley, A. L., A. F. Kabli, et al. (2014). "Staphylococcus aureus DivIB is a peptidoglycan-binding protein that is required for a morphological checkpoint in cell division." *Molecular Microbiology* **94**(5): 1041-1064.
- Bramhill, D. and C. M. Thompson (1994). "GTP-dependent polymerization of Escherichia coli FtsZ protein to form tubules." *Proc. Natl Acad. Sci. USA* **91**: 5813-5817.
- Burnette, D. T., P. Sengupta, et al. (2011). "Bleaching/blinking assisted localization microscopy for superresolution imaging using standard fluorescent molecules." *Proceedings of the National Academy of Sciences* **108**(52): 21081-21086.
- Buss, J., C. Coltharp, et al. (2013). "In vivo organization of the FtsZ-ring by ZapA and ZapB revealed by quantitative super-resolution microscopy." *Mol Microbiol*.
- Buss, J., C. Coltharp, et al. (2013). "In vivo organization of the FtsZ-ring by ZapA and ZapB revealed by quantitative super-resolution microscopy." *Mol Microbiol* **89**(6): 1099-1120.
- Buss, J., C. Coltharp, et al. (2015). "A multi-layered protein network stabilizes the Escherichia coli FtsZ-ring and modulates constriction dynamics." *PLoS Genetics* (accepted).
- Buss, J., C. Coltharp, et al. (2013). "Super-resolution Imaging of the Bacterial Division Machinery." *J Vis Exp*(71): e50048.
- Buss, J., C. Coltharp, et al. (2013). "Super-resolution imaging of the bacterial division machinery." *J Vis Exp*(71).

- Campos, M., Ivan V. Surovtsev, et al. "A Constant Size Extension Drives Bacterial Cell Size Homeostasis." Cell **159**(6): 1433-1446.
- Carmon, G., I. Fishov, et al. (2012). "Oriented imaging of 3D subcellular structures in bacterial cells using optical tweezers." Opt Lett **37**(3): 440-442.
- Chattopadhyaya, S., F. B. Abu Bakar, et al. (2008). "In Vivo Imaging of a Bacterial Cell Division Protein Using a Protease-Assisted Small-Molecule Labeling Approach." ChemBioChem **9**(5): 677-680.
- Chen, J. C. and J. Beckwith (2001). "FtsQ, FtsL and FtsI require FtsK, but not FtsN, for co-localization with FtsZ during Escherichia coli cell division." Molecular Microbiology **42**(2): 395-413.
- Chen, Y., K. Bjornson, et al. (2005). "A rapid fluorescence assay for FtsZ assembly indicates cooperative assembly with a dimer nucleus." Biophys J **88**(1): 505-514.
- Chen, Y. and H. P. Erickson (2011). "Conformational changes of FtsZ reported by tryptophan mutants." Biochemistry **50**(21): 4675-4684.
- Chen, Y., S. L. Milam, et al. (2012). "SulA inhibits assembly of FtsZ by a simple sequestration mechanism." Biochemistry **51**(14): 3100-3109.
- Chien, F.-C., C. W. Kuo, et al. (2011). "Exploring the Formation of Focal Adhesions on Patterned Surfaces Using Super-Resolution Imaging." Small **7**(20): 2906-2913.
- Churchman, L. S., H. Flyvbjerg, et al. (2006). "A non-Gaussian distribution quantifies distances measured with fluorescence localization techniques." Biophys J **90**(2): 668-671.
- Coltharp, C., J. Buss, et al. (2015). "Nanoscale architecture and dynamics of the FtsZ-ring during constriction in *E. coli*." manuscript in submission.
- Coltharp, C., R. P. Kessler, et al. (2012). "Accurate construction of photoactivated localization microscopy (PALM) images for quantitative measurements." PLoS One **7**(12): e51725.
- Coltharp, C. and J. Xiao (2012). "Superresolution microscopy for microbiology." Cellular Microbiology **14**(12): 1808-1818.
- Coltharp, C., X. Yang, et al. (2014). "Quantitative analysis of single-molecule superresolution images." Current Opinion in Structural Biology **28**(0): 112-121.
- Colville, K., N. Tompkins, et al. (2009). "Effects of Poly(l-lysine) Substrates on Attached Escherichia coli Bacteria." Langmuir **26**(4): 2639-2644.
- Dai, K. and J. Lutkenhaus (1992). "The proper ratio of FtsZ to FtsA is required for cell division to occur in Escherichia coli." J Bacteriol **174**(19): 6145-6151.
- Dai, K., Y. Xu, et al. (1993). "Cloning and characterization of ftsN, an essential cell division gene in Escherichia coli isolated as a multicopy suppressor of ftsA12(Ts)." J Bacteriol **175**(12): 3790-3797.
- Dajkovic, A., G. Lan, et al. (2008). "MinC Spatially Controls Bacterial Cytokinesis by Antagonizing the Scaffolding Function of FtsZ." Current Biology **18**(4): 235-244.
- Dajkovic, A., A. Mukherjee, et al. (2008). "Investigation of regulation of FtsZ assembly by SulA and development of a model for FtsZ polymerization." J Bacteriol **190**(7): 2513-2526.
- Dajkovic, A., S. Pichoff, et al. (2010). "Cross-linking FtsZ polymers into coherent Z rings." Mol Microbiol **78**(3): 651-668.
- Datsenko, K. A. and B. L. Wanner (2000). "One-step inactivation of chromosomal genes in Escherichia coli K-12 using PCR products." Proceedings of the National Academy of Sciences **97**(12): 6640-6645.
- David, C. C., P. Dedecker, et al. (2012). "Spectroscopic characterization of Venus at the single molecule level." Photochemical & Photobiological Sciences **11**(2).

- de Boer, P., R. Crossley, et al. (1992). "The essential bacterial cell-division protein FtsZ is a GTPase." *Nature* **359**(6392): 254-256.
- de Pedro, M. A., J. C. Quintela, et al. (1997). "Murein segregation in *Escherichia coli*." *J Bacteriol* **179**(9): 2823-2834.
- Deghorain, M., C. Pagès, et al. (2011). "A Defined Terminal Region of the *E. coli* Chromosome Shows Late Segregation and High FtsK Activity." *PLoS One* **6**(7): e22164.
- Dempsey, G. T., J. C. Vaughan, et al. (2011). "Evaluation of fluorophores for optimal performance in localization-based super-resolution imaging." *Nat Meth* **8**(12): 1027-1036.
- Dietz, M. S., F. Fricke, et al. (2014). "Receptor-ligand interactions: binding affinities studied by single-molecule and super-resolution microscopy on intact cells." *Chemphyschem* **15**(4): 671-676.
- Durisic, N., L. Laparra-Cuervo, et al. (2014). "Single-molecule evaluation of fluorescent protein photoactivation efficiency using an in vivo nanotemplate." *Nat Meth* **11**(2): 156-162.
- Egan, A. J. and W. Vollmer (2013). "The physiology of bacterial cell division." *Ann N Y Acad Sci* **1277**: 8-28.
- Egan, A. J. F. and W. Vollmer (2013). "The physiology of bacterial cell division." *Annals of the New York Academy of Sciences* **1277**(1): 8-28.
- Endesfelder, U., S. Malkusch, et al. (2011). "Chemically Induced Photoswitching of Fluorescent Probes—A General Concept for Super-Resolution Microscopy." *Molecules* **16**(4): 3106-3118.
- Endesfelder, U., S. Malkusch, et al. (2014). "A simple method to estimate the average localization precision of a single-molecule localization microscopy experiment." *Histochemistry and Cell Biology* **141**(6): 629-638.
- Erickson, H. P. (1997). "FtsZ, a tubulin homologue in prokaryote cell division." *Trends Cell Biol* **7**(9): 362-367.
- Erickson, H. P. (2009). "Modeling the physics of FtsZ assembly and force generation." *Proc Natl Acad Sci U S A* **106**(23): 9238-9243.
- Erickson, H. P., D. E. Anderson, et al. (2010). "FtsZ in Bacterial Cytokinesis: Cytoskeleton and Force Generator All in One." *Microbiology and Molecular Biology Reviews* **74**(4): 504-528.
- Erickson, H. P. and D. Stoffler (1996). "Protofilaments and rings, two conformations of the tubulin family conserved from bacterial FtsZ to alpha/beta and gamma tubulin." *J Cell Biol* **135**(1): 5-8.
- Espeli, O., R. Borne, et al. (2012). "A MatP-divisome interaction coordinates chromosome segregation with cell division in *E. coli*." *EMBO J* **31**(14): 3198-3211.
- Fernandez-Suarez, M. and A. Y. Ting (2008). "Fluorescent probes for super-resolution imaging in living cells." *Nat Rev Mol Cell Biol* **9**(12): 929-943.
- Fischer, A. H., K. A. Jacobson, et al. (2008). "Fixation and Permeabilization of Cells and Tissues." *Cold Spring Harbor Protocols* **2008**(5): pdb.top36.
- Fleming, T. C., J. Y. Shin, et al. (2010). "Dynamic SpoIIIE assembly mediates septal membrane fission during *Bacillus subtilis* sporulation." *Genes & Development* **24**(11): 1160-1172.
- Fletcher, P. A., D. R. Scriven, et al. (2010). "Multi-image colocalization and its statistical significance." *Biophys J* **99**(6): 1996-2005.
- Folling, J., M. Bossi, et al. (2008). "Fluorescence nanoscopy by ground-state depletion and single-molecule return." *Nat Meth* **5**(11): 943-945.

- Friedman, N., S. Vardi, et al. (2005). "Precise Temporal Modulation in the Response of the SOS DNA Repair Network in Individual Bacteria." PLoS Biol **3**(7): e238.
- Frohn, J. T., H. F. Knapp, et al. (2000). "True optical resolution beyond the Rayleigh limit achieved by standing wave illumination." Proceedings of the National Academy of Sciences **97**(13): 7232-7236.
- Fu, G., T. Huang, et al. (2010). "In vivo structure of the E. coli FtsZ-ring revealed by photoactivated localization microscopy (PALM)." PLoS One **5**(9): e12682.
- Fu, G., T. Huang, et al. (2010). "In Vivo Structure of the E. coli FtsZ-ring Revealed by Photoactivated Localization Microscopy (PALM)." PLoS One **5**(9): e12680.
- Fu, G., T. Huang, et al. (2010). "<italic>In Vivo</italic> Structure of the <italic>E. coli</italic> FtsZ-ring Revealed by Photoactivated Localization Microscopy (PALM)." PLoS One **5**(9): e12680.
- Galli, E. and K. Gerdes (2010). "Spatial resolution of two bacterial cell division proteins: ZapA recruits ZapB to the inner face of the Z-ring." Molecular Microbiology **76**(6): 1514-1526.
- Galli, E. and K. Gerdes (2012). "FtsZ-ZapA-ZapB interactome of Escherichia coli." J Bacteriol **194**(2): 292-302.
- Garcia-Parajo, M. F., M. Koopman, et al. (2001). "The nature of fluorescence emission in the red fluorescent protein DsRed, revealed by single-molecule detection." Proceedings of the National Academy of Sciences **98**(25): 14392-14397.
- Geisbrecht, B. V., S. Bouyain, et al. (2006). "An optimized system for expression and purification of secreted bacterial proteins." Protein Expression and Purification **46**(1): 23-32.
- Geissler, B., D. Elraheb, et al. (2003). "A gain-of-function mutation in ftsA bypasses the requirement for the essential cell division gene zipA in Escherichia coli." Proc Natl Acad Sci U S A **100**(7): 4197-4202.
- Geissler, B., D. Shiomi, et al. (2007). "The ftsA* gain-of-function allele of Escherichia coli and its effects on the stability and dynamics of the Z ring." Microbiology **153**(Pt 3): 814-825.
- Gerding, M. A., B. Liu, et al. (2009). "Self-enhanced accumulation of FtsN at Division Sites and Roles for Other Proteins with a SPOR domain (DamX, DedD, and RlpA) in Escherichia coli cell constriction." J Bacteriol **191**(24): 7383-7401.
- Ghosh, B. and A. Sain (2008). "Origin of contractile force during cell division of bacteria." Phys Rev Lett **101**(17): 178101.
- Ghosh, B. and A. Sain (2011). "Force generation in bacteria without nucleotide-dependent bending of cytoskeletal filaments." Physical Review E **83**(5): 051924.
- Goehring, N. W. and J. Beckwith (2005). "Diverse Paths to Midcell: Assembly of the Bacterial Cell Division Machinery." Current Biology **15**(13): R514-R526.
- Gonzalez, J. M., M. Velez, et al. (2005). "Cooperative behavior of Escherichia coli cell-division protein FtsZ assembly involves the preferential cyclization of long single-stranded fibrils." Proc Natl Acad Sci U S A **102**(6): 1895-1900.
- Gower, J. C. and P. Legendre (1986). "Metric and Euclidean properties of dissimilarity coefficients." Journal of Classification **3**(1): 5-48.
- Grecco, H. E. and P. J. Verveer (2011). "FRET in cell biology: still shining in the age of super-resolution?" Chemphyschem **12**(3): 484-490.
- Greenfield, D., A. L. McEvoy, et al. (2009). "Self-Organization of the <italic>Escherichia coli</italic> Chemotaxis Network Imaged with Super-Resolution Light Microscopy." PLoS Biol **7**(6): e1000137.

- Greenfield, D., A. L. McEvoy, et al. (2009). "Self-organization of the Escherichia coli chemotaxis network imaged with super-resolution light microscopy." PLoS Biol **7**(6): e1000137.
- Grotjohann, T., I. Testa, et al. (2011). "Diffraction-unlimited all-optical imaging and writing with a photochromic GFP." Nature **478**(7368): 204-208.
- Guberman, J. M., A. Fay, et al. (2008). "PSICIC: noise and asymmetry in bacterial division revealed by computational image analysis at sub-pixel resolution." PLoS Comput Biol **4**(11): e1000233.
- Gueiros-Filho, F. J. and R. Losick (2002). "A widely conserved bacterial cell division protein that promotes assembly of the tubulin-like protein FtsZ." Genes Dev **16**(19): 2544-2556.
- Gunzenhauser, J., N. Olivier, et al. (2012). "Quantitative super-resolution imaging reveals protein stoichiometry and nanoscale morphology of assembling HIV-Gag virions." Nano Lett **12**(9): 4705-4710.
- Gustafsson, M. G. L. (2000). "Surpassing the lateral resolution limit by a factor of two using structured illumination microscopy." Journal of Microscopy **198**(2): 82-87.
- Gustafsson, M. G. L. (2005). "Nonlinear structured-illumination microscopy: Wide-field fluorescence imaging with theoretically unlimited resolution." Proceedings of the National Academy of Sciences of the United States of America **102**(37): 13081-13086.
- Haase, P. (1995). "Spatial pattern analysis in ecology based on Ripley's K-function: Introduction and methods of edge correction." Journal of Vegetation Science **6**(4): 575-582.
- Habuchi, S., R. Ando, et al. (2005). "Reversible single-molecule photoswitching in the GFP-like fluorescent protein Dronpa." Proceedings of the National Academy of Sciences of the United States of America **102**(27): 9511-9516.
- Hale, C. A. and P. A. de Boer (1997). "Direct binding of FtsZ to ZipA, an essential component of the septal ring structure that mediates cell division in E. coli." Cell **88**(2): 175-185.
- Hale, C. A., A. C. Rhee, et al. (2000). "ZipA-induced bundling of FtsZ polymers mediated by an interaction between C-terminal domains." J Bacteriol **182**(18): 5153-5166.
- Haney, S. A. (2001). "Genetic analysis of the Escherichia coli FtsZ.ZipA interaction in the yeast two-hybrid system. Characterization of FtsZ residues essential for the interactions with ZipA and with FtsA." J. Biol. Chem. **276**: 11980-11987.
- Heilemann, M., S. van de Linde, et al. (2009). "Super-Resolution Imaging with Small Organic Fluorophores." Angewandte Chemie International Edition **48**(37): 6903-6908.
- Heilemann, M., S. van de Linde, et al. (2008). "Subdiffraction-Resolution Fluorescence Imaging with Conventional Fluorescent Probes." Angewandte Chemie International Edition **47**(33): 6172-6176.
- Hein, B., K. I. Willig, et al. (2008). "Stimulated emission depletion (STED) nanoscopy of a fluorescent protein-labeled organelle inside a living cell." Proceedings of the National Academy of Sciences **105**(38): 14271-14276.
- Heintzmann, R. and C. G. Cremer (1999). Laterally modulated excitation microscopy: improvement of resolution by using a diffraction grating, Stockholm, Sweden, SPIE.
- Hess, S. T., T. J. Gould, et al. (2007). "Dynamic clustered distribution of hemagglutinin resolved at 40 nm in living cell membranes discriminates between raft theories." Proc Natl Acad Sci U S A **104**(44): 17370-17375.
- Hill, N. S., P. J. Buske, et al. (2013). "A Moonlighting Enzyme Links Escherichia coli Cell Size with Central Metabolism." PLoS Genet **9**(7): e1003663.
- Hoffman, B. D., C. Grashoff, et al. (2011). "Dynamic molecular processes mediate cellular mechanotransduction." Nature **475**(7356): 316-323.

- Holden, S. J., T. Pengo, et al. (2014). "High throughput 3D super-resolution microscopy reveals *Caulobacter crescentus* in vivo Z-ring organization." Proceedings of the National Academy of Sciences **111**(12): 4566-4571.
- Holden, S. J., S. Uphoff, et al. (2011). "DAOSTORM: an algorithm for high-density super-resolution microscopy." Nat Meth **8**(4): 279-280.
- Horger, I., F. Campelo, et al. (2010). "Constricting force of filamentary protein rings evaluated from experimental results." Phys Rev E Stat Nonlin Soft Matter Phys **81**(3 Pt 1): 031922.
- Horger, I., E. Velasco, et al. (2008). "Langevin computer simulations of bacterial protein filaments and the force-generating mechanism during cell division." Phys Rev E Stat Nonlin Soft Matter Phys **77**(1 Pt 1): 011902.
- Hsu, C.-J. and T. Baumgart (2011). "Spatial Association of Signaling Proteins and F-Actin Effects on Cluster Assembly Analyzed via Photoactivation Localization Microscopy in T Cells." PLoS One **6**(8): e23586.
- Hu, Z. and J. Lutkenhaus (2000). "Analysis of MinC reveals two independent domains involved in interaction with MinD and FtsZ." J Bacteriol **182**(14): 3965-3971.
- Huang, B., W. Wang, et al. (2008). "Three-Dimensional Super-Resolution Imaging by Stochastic Optical Reconstruction Microscopy." Science **319**(5864): 810-813.
- Huecas, S., O. Llorca, et al. (2008). "Energetics and geometry of FtsZ polymers: nucleated self-assembly of single protofilaments." Biophys J **94**(5): 1796-1806.
- Huls, P. G., N. O. Vischer, et al. (1999). "Delayed nucleoid segregation in *Escherichia coli*." Mol Microbiol **33**(5): 959-970.
- Jackson, D. A., K. M. Somers, et al. (1989). "Similarity Coefficients: Measures of Co-Occurrence and Association or Simply Measures of Occurrence?" The American Naturalist **133**(3): 436-453.
- Jonas, K. (2014). "To divide or not to divide: control of the bacterial cell cycle by environmental cues." Curr Opin Microbiol **18**(0): 54-60.
- Jones, S. A., S.-H. Shim, et al. (2011). "Fast, three-dimensional super-resolution imaging of live cells." Nat Meth **8**(6): 499-505.
- Katsu, T., T. Tsuchiya, et al. (1984). "Dissipation of membrane potential of *Escherichia coli* cells induced by macromolecular polylysine." Biochemical and Biophysical Research Communications **122**(1): 401-406.
- Kiskowski, M. A., J. F. Hancock, et al. (2009). "On the use of Ripley's K-function and its derivatives to analyze domain size." Biophys J **97**(4): 1095-1103.
- Kitagawa, M., T. Ara, et al. (2005). "Complete set of ORF clones of *Escherichia coli* ASKA library (a complete set of *E. coli* K-12 ORF archive): unique resources for biological research." DNA Res **12**(5): 291-299.
- Klein, T., S. Proppert, et al. (2014). "Eight years of single-molecule localization microscopy." Histochemistry and Cell Biology **141**(6): 561-575.
- Klein, T., S. Proppert, et al. (2014). "Eight years of single-molecule localization microscopy." Histochem Cell Biol.
- Kner, P., B. B. Chhun, et al. (2009). "Super-resolution video microscopy of live cells by structured illumination." Nat Meth **6**(5): 339-342.
- Kopek, B. G., G. Shtengel, et al. (2012). "Correlative 3D superresolution fluorescence and electron microscopy reveal the relationship of mitochondrial nucleoids to membranes." Proceedings of the National Academy of Sciences **109**(16): 6136-6141.

- Lagache, T., G. Lang, et al. (2013). "Analysis of the Spatial Organization of Molecules with Robust Statistics." *PLoS One* **8**(12): e80914.
- Lan, G., B. R. Daniels, et al. (2009). "Condensation of FtsZ filaments can drive bacterial cell division." *Proc Natl Acad Sci U S A* **106**(1): 121-126.
- Lan, G., C. W. Wolgemuth, et al. (2007). "Z-ring force and cell shape during division in rod-like bacteria." *Proc Natl Acad Sci U S A* **104**(41): 16110-16115.
- Lando, D., U. Endesfelder, et al. (2012). "Quantitative single-molecule microscopy reveals that CENP-ACnp1 deposition occurs during G2 in fission yeast." *Open Biology* **2**(7).
- Lara, B. and J. A. Ayala (2002). "Topological characterization of the essential Escherichia coli cell division protein FtsW." *FEMS Microbiol Lett* **216**(1): 23-32.
- Lee, S. H., J. Y. Shin, et al. (2012). "Counting single photoactivatable fluorescent molecules by photoactivated localization microscopy (PALM)." *Proc Natl Acad Sci U S A* **109**(43): 17436-17441.
- Lee, T. K., C. Tropini, et al. (2014). "A dynamically assembled cell wall synthesis machinery buffers cell growth." *Proc Natl Acad Sci U S A* **111**(12): 4554-4559.
- Lehmann, M., S. Rocha, et al. (2011). "Quantitative Multicolor Super-Resolution Microscopy Reveals Tetherin HIV-1 Interaction." *PLoS Pathog* **7**(12): e1002456.
- Lehmann, M., S. Rocha, et al. (2011). "Quantitative multicolor super-resolution microscopy reveals tetherin HIV-1 interaction." *PLoS Pathog* **7**(12): e1002456.
- Leisch, N., J. Verheul, et al. "Growth in width and FtsZ ring longitudinal positioning in a gammaproteobacterial symbiont." *Current Biology* **22**(19): R831-R832.
- Leisch, N., J. Verheul, et al. (2012). "Growth in width and FtsZ ring longitudinal positioning in a gammaproteobacterial symbiont." *Curr Biol* **22**(19): R831-832.
- Lelek, M., F. Di Nunzio, et al. (2012). "Superresolution imaging of HIV in infected cells with FIAsh-PALM." *Proceedings of the National Academy of Sciences*.
- Lew, M. D., S. F. Lee, et al. (2011). "Three-dimensional superresolution colocalization of intracellular protein superstructures and the cell surface in live *Caulobacter crescentus*." *Proc Natl Acad Sci U S A* **108**(46): E1102-1110.
- Li, Y., J. Hsin, et al. (2013). "FtsZ protofilaments use a hinge-opening mechanism for constrictive force generation." *Science* **341**(6144): 392-395.
- Li, Z., M. J. Trimble, et al. (2007). "The structure of FtsZ filaments in vivo suggests a force-generating role in cell division." *EMBO J* **26**(22): 4694-4708.
- Lieberman, J. A., N. A. Frost, et al. (2012). "Outer Membrane Targeting, Ultrastructure, and Single Molecule Localization of the Enteropathogenic Escherichia coli Type IV Pilus Secretin BfpB." *Journal of Bacteriology* **194**(7): 1646-1658.
- Lillemeier, B. F., M. A. Mortelmaier, et al. (2010). "TCR and Lat are expressed on separate protein islands on T cell membranes and concatenate during activation." *Nat Immunol* **11**(1): 90-96.
- Liu, G., G. C. Draper, et al. (1998). "FtsK is a bifunctional protein involved in cell division and chromosome localization in Escherichia coli." *Mol Microbiol* **29**(3): 893-903.
- Liu, Z., D. Xing, et al. (2014). "Super-resolution imaging and tracking of protein-protein interactions in sub-diffraction cellular space." *Nat Commun* **5**.
- Low, H. H., M. C. Moncrieffe, et al. (2004). "The crystal structure of ZapA and its modulation of FtsZ polymerisation." *J Mol Biol* **341**(3): 839-852.
- Lu, C., M. Reedy, et al. (2000). "Straight and curved conformations of FtsZ are regulated by GTP hydrolysis." *J Bacteriol* **182**(1): 164-170.

- Lu, C., J. Stricker, et al. (2001). "Site-specific mutations of FtsZ - effects on GTPase and in vitro assembly." *BMC Microbiology* **1**(1): 7.
- Lukosz, W., Marchand, M. (1963). "Optische Abbildung unter Überschreitung der beugungsbedingten Auflösungsgrenze." *Opt. Acta* **10**: 241-255.
- Lutkenhaus, J. (2009). "FtsN--trigger for septation." *J Bacteriol* **191**(24): 7381-7382.
- Ma, X., D. W. Ehrhardt, et al. (1996). "Colocalization of cell division proteins FtsZ and FtsA to cytoskeletal structures in living Escherichia coli cells by using green fluorescent protein." *Proc Natl Acad Sci U S A* **93**(23): 12998-13003.
- MacGillavry, H. D., Y. Song, et al. (2013). "Nanoscale scaffolding domains within the postsynaptic density concentrate synaptic AMPA receptors." *Neuron* **78**(4): 615-622.
- Malkusch, S., U. Endesfelder, et al. (2012). "Coordinate-based colocalization analysis of single-molecule localization microscopy data." *Histochem Cell Biol* **137**(1): 1-10.
- Massey, F. J., Jr. (1951). "The Kolmogorov-Smirnov Test for Goodness of Fit." *Journal of the American Statistical Association* **46**(253): 68-78.
- Mateos-Gil, P., A. Paez, et al. (2012). "Depolymerization dynamics of individual filaments of bacterial cytoskeletal protein FtsZ." *Proc Natl Acad Sci U S A* **109**(21): 8133-8138.
- McAnaney, T. B., W. Zeng, et al. (2005). "Protonation, Photobleaching, and Photoactivation of Yellow Fluorescent Protein (YFP 10C): A Unifying Mechanism†." *Biochemistry* **44**(14): 5510-5524.
- McKinney, S. A., C. S. Murphy, et al. (2009). "A bright and photostable photoconvertible fluorescent protein." *Nat Meth* **6**(2): 131-133.
- Meier, E. L. and E. D. Goley (2014). "Form and function of the bacterial cytokinetic ring." *Curr Opin Cell Biol* **26**(0): 19-27.
- Mercer, K. L. and D. S. Weiss (2002). "The Escherichia coli cell division protein FtsW is required to recruit its cognate transpeptidase, FtsI (PBP3), to the division site." *J Bacteriol* **184**(4): 904-912.
- Mercer, K. L. N. and D. S. Weiss (2002). "The Escherichia coli Cell Division Protein FtsW Is Required To Recruit Its Cognate Transpeptidase, FtsI (PBP3), to the Division Site." *J Bacteriol* **184**(4): 904-912.
- Mercier, R., M.-A. Petit, et al. (2008). "The MatP/matS Site-Specific System Organizes the Terminus Region of the E. coli Chromosome into a Macrodome." *Cell* **135**(3): 475-485.
- Milam, S. L., M. Osawa, et al. (2012). "Negative-stain electron microscopy of inside-out FtsZ rings reconstituted on artificial membrane tubules show ribbons of protofilaments." *Biophys J* **103**(1): 59-68.
- Milles, S., S. Tyagi, et al. (2012). "Click Strategies for Single-Molecule Protein Fluorescence." *Journal of the American Chemical Society* **134**(11): 5187-5195.
- Mingorance, J., M. Tadros, et al. (2005). "Visualization of single Escherichia coli FtsZ filament dynamics with atomic force microscopy." *J Biol Chem* **280**(21): 20909-20914.
- Mohammadi, T., G. E. Ploeger, et al. (2009). "The GTPase activity of Escherichia coli FtsZ determines the magnitude of the FtsZ polymer bundling by ZapA in vitro." *Biochemistry* **48**(46): 11056-11066.
- Mohammadi, T., V. van Dam, et al. (2011). "Identification of FtsW as a transporter of lipid-linked cell wall precursors across the membrane." *EMBO J* **30**(8): 1425-1432.
- Monahan, L. G., A. Robinson, et al. (2009). "Lateral FtsZ association and the assembly of the cytokinetic Z ring in bacteria." *Mol Microbiol* **74**(4): 1004-1017.

- Mosyak, L., Y. Zhang, et al. (2000). "The bacterial cell-division protein ZipA and its interaction with an FtsZ fragment revealed by X-ray crystallography." *EMBO J* **19**(13): 3179-3191.
- Mukherjee, A., C. Saez, et al. (2001). "Assembly of an FtsZ mutant deficient in GTPase activity has implications for FtsZ assembly and the role of the Z ring in cell division." *J Bacteriol* **183**(24): 7190-7197.
- Nan, X., E. A. Collisson, et al. (2013). "Single-molecule superresolution imaging allows quantitative analysis of RAF multimer formation and signaling." *Proc Natl Acad Sci U S A* **110**(46): 18519-18524.
- Nguyen-Disteche, M., C. Fraipont, et al. (1998). "The structure and function of Escherichia coli penicillin-binding protein 3." *Cell Mol Life Sci* **54**(4): 309-316.
- Nickerson, A., T. Huang, et al. (2014). "Photoactivated Localization Microscopy with Bimolecular Fluorescence Complementation (BiFC-PALM) for Nanoscale Imaging of Protein-Protein Interactions in Cells." *PLoS ONE* **9**(6): e100589.
- Notelaers, K., S. Rocha, et al. (2014). "Membrane distribution of the glycine receptor alpha3 studied by optical super-resolution microscopy." *Histochem Cell Biol*.
- Ori, A., N. Banterle, et al. (2013). "Cell type-specific nuclear pores: a case in point for context-dependent stoichiometry of molecular machines." *Mol Syst Biol* **9**: 648.
- Osawa, M., D. E. Anderson, et al. (2008). "Reconstitution of Contractile FtsZ Rings in Liposomes." *Science* **320**(5877): 792-794.
- Osawa, M., D. E. Anderson, et al. (2009). "Curved FtsZ protofilaments generate bending forces on liposome membranes." *EMBO J* **28**(22): 3476-3484.
- Osawa, M. and H. P. Erickson (2006). "FtsZ from divergent foreign bacteria can function for cell division in Escherichia coli." *J Bacteriol* **188**(20): 7132-7140.
- Osawa, M. and H. P. Erickson (2011). "Inside-out Z rings--constriction with and without GTP hydrolysis." *Mol Microbiol* **81**(2): 571-579.
- Osawa, M. and H. P. Erickson (2013). "Liposome division by a simple bacterial division machinery." *Proc Natl Acad Sci U S A* **110**(27): 11000-11004.
- Paez, A., P. Mateos-Gil, et al. (2009). "Simple modeling of FtsZ polymers on flat and curved surfaces: correlation with experimental in vitro observations." *PMC Biophys* **2**(1): 8.
- Palacios, P., M. Vicente, et al. (1996). "Dependency of Escherichia coli cell-division size, and independency of nucleoid segregation on the mode and level of ftsZ expression." *Mol Microbiol* **20**(5): 1093-1098.
- Pastoret, S., C. Fraipont, et al. (2004). "Functional analysis of the cell division protein FtsW of Escherichia coli." *J Bacteriol* **186**(24): 8370-8379.
- Patterson, G. H. (2011). "Highlights of the optical highlighter fluorescent proteins." *Journal of Microscopy* **243**(1): 1-7.
- Pearson, K. (1900). "On the Criterion that a Given System of Deviations from the Probable in the Case of Correlated System of Variables is such that it can be Reasonably Supposed to have Arisen from Random Sampling." *Philosophical Magazine* **50**: 157-175.
- Penttinen, A. and D. Stoyan (2000). "Recent applications of point process methods in forestry statistics." *Statistical Science* **15**(1): 61-78.
- Peters, N. T., T. Dinh, et al. (2011). "A Fail-Safe Mechanism in the Septal Ring Assembly Pathway Generated by the Sequential Recruitment of Cell Separation Amidases and Their Activators." *J Bacteriol* **193**(18): 4973-4983.
- Pichoff, S. and J. Lutkenhaus (2002). "Unique and overlapping roles for ZipA and FtsA in septal ring assembly in Escherichia coli." *EMBO J* **21**(4): 685-693.

- Pichoff, S. and J. Lutkenhaus (2005). "Tethering the Z ring to the membrane through a conserved membrane targeting sequence in FtsA." Mol Microbiol **55**(6): 1722-1734.
- Pichoff, S., B. Shen, et al. (2012). "FtsA mutants impaired for self-interaction bypass ZipA suggesting a model in which FtsA's self-interaction competes with its ability to recruit downstream division proteins." Mol Microbiol **83**(1): 151-167.
- Plass, T., S. Milles, et al. (2011). "Genetically Encoded Copper-Free Click Chemistry." Angewandte Chemie International Edition **50**(17): 3878-3881.
- Plass, T., S. Milles, et al. (2012). "Amino Acids for Diels–Alder Reactions in Living Cells." Angewandte Chemie International Edition **51**(17): 4166-4170.
- Pogliano, J., K. Pogliano, et al. (1997). "Inactivation of FtsI inhibits constriction of the FtsZ cytokinetic ring and delays the assembly of FtsZ rings at potential division sites." Proc Natl Acad Sci U S A **94**(2): 559-564.
- Popp, D., M. Iwasa, et al. (2010). "Suprastructures and dynamic properties of Mycobacterium tuberculosis FtsZ." J Biol Chem **285**(15): 11281-11289.
- Potluri, L.-P., M. A. de Pedro, et al. (2012). "Escherichia coli low-molecular-weight penicillin-binding proteins help orient septal FtsZ, and their absence leads to asymmetric cell division and branching." Molecular Microbiology **84**(2): 203-224.
- Ptacin, J. L., S. F. Lee, et al. (2010). "A spindle-like apparatus guides bacterial chromosome segregation." Nat Cell Biol **12**(8): 791-798.
- Puchner, E. M., J. M. Walter, et al. (2013). "Counting molecules in single organelles with superresolution microscopy allows tracking of the endosome maturation trajectory." Proc Natl Acad Sci U S A **110**(40): 16015-16020.
- Raskin, D. M. and P. A. de Boer (1999). "MinDE-dependent pole-to-pole oscillation of division inhibitor MinC in Escherichia coli." J. Bacteriol. **181**: 6419-6424.
- RayChaudhuri, D. (1999). "ZipA is a MAP-Tau homolog and is essential for structural integrity of the cytokinetic FtsZ ring during bacterial cell division." EMBO J **18**(9): 2372-2383.
- RayChaudhuri, D. and J. T. Park (1992). "Escherichia coli cell-division gene ftsZ encodes a novel GTP-binding protein." Nature **359**(6392): 251-254.
- Rayleigh, L. (1896). "On the theory of optical images, with special reference to the microscope." Philosophical Magazine **42**: 167-195.
- Renz, M., B. R. Daniels, et al. (2012). "Plasticity of the asialoglycoprotein receptor deciphered by ensemble FRET imaging and single-molecule counting PALM imaging." Proceedings of the National Academy of Sciences **109**(44): E2989–E2997.
- Reshes, G., S. Vanounou, et al. (2008). "Cell shape dynamics in Escherichia coli." Biophys J **94**(1): 251-264.
- Reshes, G., S. Vanounou, et al. (2008). "Timing the start of division in E. coli: a single-cell study." Phys Biol **5**(4): 046001.
- Ribeiro, S. A., P. Vagnarelli, et al. (2010). "A super-resolution map of the vertebrate kinetochore." Proc Natl Acad Sci U S A **107**(23): 10484-10489.
- Ripley, B. D. (1989). Statistical Inference for Spatial Processes. New York, NY, USA, Cambridge University Press
- Rojas, E., J. A. Theriot, et al. (2014). "Response of Escherichia coli growth rate to osmotic shock." Proceedings of the National Academy of Sciences **111**(21): 7807-7812.
- Romberg, L., M. Simon, et al. (2001). "Polymerization of Ftsz, a bacterial homolog of tubulin. is assembly cooperative?" J Biol Chem **276**(15): 11743-11753.

- Rossy, J., E. Cohen, et al. (2014). "Method for co-cluster analysis in multichannel single-molecule localisation data." Histochem Cell Biol.
- Rowlett, V. W. and W. Margolin (2014). "3D-SIM super-resolution of FtsZ and its membrane tethers in Escherichia coli cells." Biophys J **107**(8): L17-20.
- Rowlett, Veronica W. and W. Margolin (2014). "3D-SIM Super-resolution of FtsZ and Its Membrane Tethers in Escherichia coli Cells." Biophys J **107**(8): L17-L20.
- Rueda, S., M. Vicente, et al. (2003). "Concentration and assembly of the division ring proteins FtsZ, FtsA, and ZipA during the Escherichia coli cell cycle." J Bacteriol **185**(11): 3344-3351.
- Rust, M. J., M. Bates, et al. (2006). "Sub-diffraction-limit imaging by stochastic optical reconstruction microscopy (STORM)." Nat Methods **3**(10): 793-795.
- Sauvage, E., A. Derouaux, et al. (2014). "Crystal structure of penicillin-binding protein 3 (PBP3) from Escherichia coli." PLoS One **9**(5): e98042.
- Sauvage, E., F. Kerff, et al. (2008). "The penicillin-binding proteins: structure and role in peptidoglycan biosynthesis." FEMS Microbiol Rev **32**(2): 234-258.
- Scarselli, M., P. Annibale, et al. (2012). "Cell type-specific beta2-adrenergic receptor clusters identified using photoactivated localization microscopy are not lipid raft related, but depend on actin cytoskeleton integrity." J Biol Chem **287**(20): 16768-16780.
- Schmied, J. J., M. Raab, et al. (2014). "DNA origami-based standards for quantitative fluorescence microscopy." Nat. Protocols **9**(6): 1367-1391.
- Schneider, C. A., W. S. Rasband, et al. (2012). "NIH Image to ImageJ: 25 years of image analysis." Nat Meth **9**(7): 671-675.
- Sengupta, P., T. Jovanovic-Talman, et al. (2013). "Quantifying spatial organization in point-localization superresolution images using pair correlation analysis." Nat Protoc **8**(2): 345-354.
- Sengupta, P., T. Jovanovic-Talman, et al. (2011). "Probing protein heterogeneity in the plasma membrane using PALM and pair correlation analysis." Nat Methods **8**(11): 969-975.
- Sengupta, P. and J. Lippincott-Schwartz (2012). "Quantitative analysis of photoactivated localization microscopy (PALM) datasets using pair-correlation analysis." Bioessays **34**(5): 396-405.
- Sham, L. T., E. K. Butler, et al. (2014). "Bacterial cell wall. MurJ is the flippase of lipid-linked precursors for peptidoglycan biogenesis." Science **345**(6193): 220-222.
- Shannon, C. E. (1949). "Communication in the presence of noise." Proc. Institute of Radio Engineers **37**(1): 10-21.
- Sharonov, A. and R. M. Hochstrasser (2006). "Wide-field subdiffraction imaging by accumulated binding of diffusing probes." Proceedings of the National Academy of Sciences **103**(50): 18911-18916.
- Shen, B. and J. Lutkenhaus (2010). "Examination of the interaction between FtsZ and MinCN in E. coli suggests how MinC disrupts Z rings." Mol Microbiol **75**(5): 1285-1298.
- Sherman, E., V. Barr, et al. (2011). "Functional Nanoscale Organization of Signaling Molecules Downstream of the T Cell Antigen Receptor." Immunity **35**(5): 705-720.
- Sherman, E., V. Barr, et al. (2011). "Functional nanoscale organization of signaling molecules downstream of the T cell antigen receptor." Immunity **35**(5): 705-720.
- Shin, J. Y., W. Vollmer, et al. (2013). "Glutamate 83 and arginine 85 of helix H3 bend are key residues for FtsZ polymerization, GTPase activity and cellular viability of Escherichia coli: lateral mutations affect FtsZ polymerization and E. coli viability." BMC Microbiology **13**(1): 26.

- Shiomi, D. and W. Margolin (2007). "The C-terminal domain of MinC inhibits assembly of the Z ring in Escherichia coli." J Bacteriol **189**(1): 236-243.
- Shroff, H., C. G. Galbraith, et al. (2008). "Live-cell photoactivated localization microscopy of nanoscale adhesion dynamics." Nat Meth **5**(5): 417-423.
- Shroff, H., C. G. Galbraith, et al. (2007). "Dual-color superresolution imaging of genetically expressed probes within individual adhesion complexes." Proceedings of the National Academy of Sciences **104**(51): 20308-20313.
- Shtengel, G., J. A. Galbraith, et al. (2009). "Interferometric fluorescent super-resolution microscopy resolves 3D cellular ultrastructure." Proceedings of the National Academy of Sciences.
- Small, E., R. Marrington, et al. (2007). "FtsZ polymer-bundling by the Escherichia coli ZapA orthologue, YgfE, involves a conformational change in bound GTP." J Mol Biol **369**(1): 210-221.
- Stirling Churchman, L., H. Flyvbjerg, et al. (2006). "A Non-Gaussian Distribution Quantifies Distances Measured with Fluorescence Localization Techniques." Biophysical Journal **90**(2): 668-671.
- Stouf, M., J. C. Meile, et al. (2013). "FtsK actively segregates sister chromosomes in Escherichia coli." Proc Natl Acad Sci U S A **110**(27): 11157-11162.
- Strahl, H. and L. W. Hamoen (2010). "Membrane potential is important for bacterial cell division." Proceedings of the National Academy of Sciences **107**(27): 12281-12286.
- Strauss, M. P., A. T. F. Liew, et al. (2012). "3D-SIM Super Resolution Microscopy Reveals a Bead-Like Arrangement for FtsZ and the Division Machinery: Implications for Triggering Cytokinesis." PLoS Biol **10**(9): e1001389.
- Stricker, J., P. Maddox, et al. (2002). "Rapid assembly dynamics of the Escherichia coli FtsZ-ring demonstrated by fluorescence recovery after photobleaching." Proceedings of the National Academy of Sciences **99**(5): 3171-3175.
- Stromqvist, J., K. Skoog, et al. (2010). "Estimating Z-ring radius and contraction in dividing Escherichia coli." Mol Microbiol **76**(1): 151-158.
- Sun, S. X. and H. Jiang (2011). "Physics of bacterial morphogenesis." Microbiol Mol Biol Rev **75**(4): 543-565.
- Sung, M. T., Y. T. Lai, et al. (2009). "Crystal structure of the membrane-bound bifunctional transglycosylase PBP1b from Escherichia coli." Proc Natl Acad Sci U S A **106**(22): 8824-8829.
- Surovtsev, I. V., J. J. Morgan, et al. (2008). "Kinetic Modeling of the Assembly, Dynamic Steady State, and Contraction of the FtsZ Ring in Prokaryotic Cytokinesis." PLoS Comput Biol **4**(7): e1000102.
- Suzuki, H., Y. Nishimura, et al. (1978). "On the process of cellular division in Escherichia coli: a series of mutants of E. coli altered in the penicillin-binding proteins." Proc Natl Acad Sci U S A **75**(2): 664-668.
- Szwedziak, P., Q. Wang, et al. (2014). Architecture of the ring formed by the tubulin homologue FtsZ in bacterial cell division.
- Szwedziak, P., Q. Wang, et al. (2012). "FtsA forms actin-like protofilaments." EMBO J **31**(10): 2249-2260.
- Tarancon Diez, L., C. Borsch, et al. (2014). "Coordinate-based co-localization-mediated analysis of arrestin clustering upon stimulation of the C-C chemokine receptor 5 with RANTES/CCL5 analogues." Histochem Cell Biol.

- Taschner, P. E., P. G. Huls, et al. (1988). "Division behavior and shape changes in isogenic ftsZ, ftsQ, ftsA, pbpB, and ftsE cell division mutants of Escherichia coli during temperature shift experiments." *J Bacteriol* **170**(4): 1533-1540.
- Thevenaz, P., U. E. Ruttimann, et al. (1998). "A pyramid approach to subpixel registration based on intensity." *Image Processing, IEEE Transactions on* **7**(1): 27-41.
- Thompson, R. E., D. R. Larson, et al. (2002). "Precise Nanometer Localization Analysis for Individual Fluorescent Probes." *Biophysical Journal* **82**(5): 2775-2783.
- Tsukanov, R., G. Reshes, et al. (2011). "Timing of Z-ring localization in Escherichia coli." *Phys Biol* **8**(6): 066003.
- Ulbrich, M. H. and E. Y. Isacoff (2007). "Subunit counting in membrane-bound proteins." *Nat Meth* **4**(4): 319-321.
- Ursinus, A., F. van den Ent, et al. (2004). "Murein (peptidoglycan) binding property of the essential cell division protein FtsN from Escherichia coli." *J Bacteriol* **186**(20): 6728-6737.
- Vale, R. D. (2000). "AAA proteins. Lords of the ring." *J Cell Biol* **150**(1): F13-19.
- van de Linde, S., S. Wolter, et al. (2010). "The effect of photoswitching kinetics and labeling densities on super-resolution fluorescence imaging." *Journal of Biotechnology* **149**(4): 260-266.
- Varma, A., M. A. de Pedro, et al. (2007). "FtsZ Directs a Second Mode of Peptidoglycan Synthesis in Escherichia coli." *J Bacteriol* **189**(15): 5692-5704.
- Veatch, S. L., B. B. Machta, et al. (2012). "Correlation functions quantify super-resolution images and estimate apparent clustering due to over-counting." *PLoS One* **7**(2): e31457.
- Vicente, M. and J. Löwe (2003). Ring, helix, sphere and cylinder: the basic geometry of prokaryotic cell division.
- Wang, S., J. R. Moffitt, et al. (2014). "Characterization and development of photoactivatable fluorescent proteins for single-molecule-based superresolution imaging." *Proceedings of the National Academy of Sciences.*
- Wang, W., G. W. Li, et al. (2011). "Chromosome organization by a nucleoid-associated protein in live bacteria." *Science* **333**(6048): 1445-1449.
- Wang, Y., T. Quan, et al. (2012). "PALMER: a method capable of parallel localization of multiple emitters for high-density localization microscopy." *Opt Express* **20**(14): 16039-16049.
- Weart, R. B., A. H. Lee, et al. (2007). "A metabolic sensor governing cell size in bacteria." *Cell* **130**(2): 335-347.
- Weart, R. B. and P. A. Levin (2003). "Growth rate-dependent regulation of medial FtsZ ring formation." *J Bacteriol* **185**(9): 2826-2834.
- Weiss, D. S. (2015). "Last but not least: new insights into how FtsN triggers constriction during Escherichia coli cell division." *Mol Microbiol* **95**(6): 903-909.
- Westphal, V., S. O. Rizzoli, et al. (2008). "Video-Rate Far-Field Optical Nanoscopy Dissects Synaptic Vesicle Movement." *Science* **320**(5873): 246-249.
- Wheeler, R., S. Mesnage, et al. (2011). "Super-resolution microscopy reveals cell wall dynamics and peptidoglycan architecture in ovococcal bacteria." *Molecular Microbiology* **82**(5): 1096-1109.
- Wientjes, F. B. and N. Nanninga (1989). "Rate and topography of peptidoglycan synthesis during cell division in Escherichia coli: concept of a leading edge." *J Bacteriol* **171**(6): 3412-3419.
- Wolter, S., U. Endesfelder, et al. (2011). "Measuring localization performance of super-resolution algorithms on very active samples." *Opt. Express* **19**(8): 7020-7033.

- Yeow, E. K. L., S. M. Melnikov, et al. (2006). "Characterizing the Fluorescence Intermittency and Photobleaching Kinetics of Dye Molecules Immobilized on a Glass Surface." The Journal of Physical Chemistry A **110**(5): 1726-1734.
- Zhang, M., H. Chang, et al. (2012). "Rational design of true monomeric and bright photoactivatable fluorescent proteins." Nat Meth **advance online publication**.
- Zhao, J., S. Bruck, et al. (2013). "CD2AP links cortactin and capping protein at the cell periphery to facilitate formation of lamellipodia." Mol Cell Biol **33**(1): 38-47.
- Zhao, Z. W., R. Roy, et al. (2014). "Spatial organization of RNA polymerase II inside a mammalian cell nucleus revealed by reflected light-sheet superresolution microscopy." Proc Natl Acad Sci U S A **111**(2): 681-686.
- Zhu, L., W. Zhang, et al. (2012). "Faster STORM using compressed sensing." Nat Meth **9**(7): 721-723.

Curriculum Vitae

Carla Coltharp

May 21, 2015

Place of birth: Corpus Christi, TX

Academic Background

2015 Ph.D. Program in Molecular Biophysics, Johns Hopkins University School of Medicine

2006 B.S. Chemistry, Massachusetts Institute of Technology

Research Experience

The Johns Hopkins University School of Medicine, Baltimore, MD 2010 - present
Graduate Researcher, Laboratory of Professor Jie Xiao

Characterization of cytoskeleton involved in bacterial cell division using super-resolution microscopy

- Developed and published image acquisition and analysis methods to quantify *in vivo* biophysical properties of macromolecular structures using super-resolution microscopy.
- Re-defined the role of the bacterial cytoskeletal protein, FtsZ, in cell division by revealing the nanoscale structure and activity of the contracting cell division ring in *E. coli*.

Sensor Technologies LLC, Shrewsbury, MA 2006 -2009
Chemistry Research Associate

Minimally-Invasive Glucose Sensor Development:

- Optimized production and formulation of fluorescently-labeled proteins for skin-implantable glucose sensor.
- Created computational models to predict sensor performance limits, error budgets, and optimal component formulations.

QuantumXpert™ Fluorescence Correlation Spectroscopy (FCS) Instrument Development:

- Independently designed and authored end-user software for FCS data acquisition and analysis.
- Developed molecular interaction assays to showcase system functionality to investors and clients.

Massachusetts Institute of Technology, Cambridge, MA 2005 - 2006
Undergraduate Researcher, Laboratory of Professor Sarah O'Connor

Mutational analysis of strictosidine synthase, a plant enzyme that produces chemotherapeutic agents:

- Developed HPLC analysis routines that identified several amino acids important to enzyme function.
- Produced mutant enzymes with broadened substrate specificity, allowing for turnover of unnatural substrates to produce novel natural products.

Awards & Honors

- 2014 **ASCB/KGI Managing Science in Industry Course:** fully-funded, two-week MBA-style course regarding science commercialization; selected as one of 40 students out of 600 applicants
- 2011 **NSF Graduate Research Fellowship, Honorable Mention**
- 2010 **Turock Young Scientist Award:** annually recognizes two promising graduate students in the Johns Hopkins Institute for Basic Biomedical Sciences
- 2009 **George E. Owen Fellowship:** three-year supplemental fellowship provided to attract outstanding graduate students to Johns Hopkins University

Teaching & Service

- 2013 **Instructor,** Single Cell Analysis Course, Cold Spring Harbor Laboratory
- 2012 **Organizer,** JHU Institute for Biophysical Research Annual Retreat
- 2011-12 **Volunteer Instructor,** JHMI Fun with Science Summer Camp (for Baltimore students)
- 2011-12 **Volunteer Instructor,** JHMI Science Day (for Baltimore students)
- 2008 **Instructor,** Analytical & Quantitative Light Microscopy Course, Marine Biological Laboratory

Publications

Buss J, Coltharp C, Shtengel G, Yang X, Hess H, Xiao J. (2015) A multi-layered protein network stabilizes the *Escherichia coli* FtsZ-ring and modulates constriction dynamics. *PLOS Genetics*.

Coltharp C, Yang X, Xiao J. (2014) Quantitative analysis of single-molecule superresolution images. *Current Opinion in Structural Biology*.

Buss J, Coltharp C, Huang T, Pohlmeier C, Wang SC, Hatem C, Xiao J. (2013) *In vivo* organization of the FtsZ-ring by ZapA and ZapB revealed by quantitative super-resolution microscopy. *Molecular Microbiology*.

Buss J, Coltharp C, Xiao J. (2013) Super-resolution imaging of the bacterial cell division machinery. *Journal of Visualized Experiments*.

Coltharp C, Kessler RP, Xiao J. (2012) Accurate construction of photoactivated localization microscopy (PALM) images for quantitative measurements. *PLOS One*.

Coltharp C, Xiao J. (2012) Superresolution microscopy for microbiology. *Cellular Microbiology*.

Herbst K, Coltharp C, Amzel L, Zhang, J. (2011) Direct Activation of Epac by Sulfonylurea is Isoform Specific. *Chemistry & Biology*.

Fu G, Huang T, Buss J, **Coltharp C**, Hensel Z, Xiao J. (2010) *In vivo* structure of the *E. coli* FtsZ-ring revealed by photoactivated localization microscopy (PALM). *PLOS One*.

Chen S, Galan MC, **Coltharp C**, O'Connor SE. (2006) Redesign of a central enzyme in alkaloid biosynthesis. *Chemistry & Biology*.

submitted

Coltharp C, Buss J, Plumer T, Xiao J. The rate of *E. coli* cytokinesis is not limited by FtsZ ring contraction, but by cell wall growth and chromosome segregation.

Oral Presentations

Nanoscale architecture and remodeling of the contracting E. coli Z-ring during cell division. Biophysical Society Meeting, February 2015, Baltimore, Maryland

Nanoscale architecture and remodeling of the contracting E. coli Z-ring during cell division. JHMI Topics in Macromolecular Structure and Function Seminar Series, February 2015, Baltimore, Maryland

Super-resolution insights into bacterial cell division. Institute for Biophysical Research Retreat, September 2014, Baltimore, Maryland

Quantitative analysis of super-resolution microscopy data. Single Cell Analysis Course Instruction, June 2013, Cold Spring Harbor, New York

In vivo structure and dynamics of E. coli FtsZ structures during cytokinesis. JHMI Topics in Macromolecular Structure and Function Seminar Series, April 2012, Baltimore, Maryland

Super-resolution Fluorescence Microscopy. JHMI Center for Cell Dynamics Seminar Series, October 2011, Baltimore, MD

In vivo structure and dynamics of E. coli FtsZ structures during cytokinesis. JHMI Center for Cell Dynamics Seminar Series, October 2011, Baltimore, MD

Poster Presentations

Nanoscale architecture and remodeling of the contracting E. coli Z-ring during cell division. Biophysical Society Meeting, February 2015, Baltimore, Maryland

Superresolution investigation of the E. coli cell division ring during constriction. Zing Bacterial Cell Biology Conference, December 2013, Playa del Carmen, Mexico

Superresolution investigation of the dynamics of FtsZ structures during E. coli cell division. Biophysical Society Meeting, February 2013, Philadelphia, Pennsylvania

Superresolution investigation of in vivo FtsZ structures during E. coli cell division. Bacteria, Archaea and Phages, August 2012, Cold Spring Harbor, New York

Superresolution investigation of in vivo structure and dynamics of E. coli FtsZ structures during cytokinesis. Mats Gustafsson Memorial Symposium on High Resolution Imaging, May 2012, Ashburn, Virginia

Superresolution investigation of in vivo structure and dynamics of E. coli FtsZ structures during cytokinesis. Biophysical Society Meeting, February 2012, San Diego, California

Imaging the in vivo structure and dynamics of the E. coli cell division apparatus with superresolution . New Advances in Optical Imaging of Live Cells and Organisms, May 2011, Suzhou, China

In vivo structure of the E. coli FtsZ-ring revealed by Photoactivated Localization Microscopy (PALM). Biophysical Society Meeting, March 2011, Baltimore, Maryland